uOttawa

L'Université canadienne
Canada's university

t

FACULTÉ DES ÉTUDES SUPÉRIEURES ET POSTOCTORALES

uOttawa

L'Université canadienne
Canada's university

FACULTY OF GRADUATE AND POSDOCTORAL STUDIES

Gitanjali Kolhatkar
AUTEUR DE LA THÈSE / AUTHOR OF THESIS

M.Sc. (Physics)
GRADE / DEGREE

Department of Physics
FACULTÉ, ÉCOLE, DÉPARTEMENT / FACULTY, SCHOOL, DEPARTMENT

Characterisation of High-Efficiency Multi-Junction Solar Cells and Tunnel Junctions
TITRE DE LA THÈSE / TITLE OF THESIS

Karin Hinzer
DIRECTEUR (DIRECTRICE) DE LA THÈSE / THESIS SUPERVISOR

CO-DIRECTEUR (CO-DIRECTRICE) DE LA THÈSE / THESIS CO-SUPERVISOR

Emery Fortin

Christopher Py

Thomas Gregoire

Gary W. Slater
Le Doyen de la Faculté des études supérieures et postdoctorales / Dean of the Faculty of Graduate and Postdoctoral Studies

Characterisation of high-efficiency multi-junction solar cells and tunnel junctions

by
Gitanjali Kolhatkar

Thesis submitted to the
Faculty of Graduate and Postdoctoral Studies
In partial fulfillment of the requirements
For the MSc degree in Physics

Department of Physics
Faculty of Sciences
University of Ottawa

Your file Votre référence
ISBN: 978-0-494-79712-9
Our file Notre référence
ISBN: 978-0-494-79712-9

Abstract

Tunnel junctions for use in solar cells and monolithic multi-junction solar cells are studied experimentally. The current density-voltage characteristic of an AlGaAs/AlGaAs tunnel junction having a mesa resistance of 0.11 $m\Omega \cdot cm^2$ is determined using time-averaged measurements. A tunneling peak higher than the operating point of a solar cell is recorded by this method, with a value of ~950 A/cm^2. Due to the unstable nature of the negative differential resistance region of the current density-voltage curve, measurements of the tunneling peak and valley current densities are obscured. A time-dependent analysis is performed on this sample, from which a tunneling peak of a value larger than 1100 A/cm^2 is determined. An AlGaAs/InGaP tunnel junction having a tunneling peak of 80 A/cm^2 is presented. Multi-junction solar cells fabricated using indium tin-oxide as transparent top electrodes are measured. These cells have a maximal efficiency of 25.1% at 3 suns illumination and 26.1% at 20 suns, ~40% lower efficiency than the standard multi-junction solar cell.

Statement of Originality

Except stated otherwise, the results presented in this thesis were obtained by the author during the period of her M. Sc. research project under the supervision of Dr. Karin Hinzer. They are to the best of her knowledge original.

This project was developed through the SUNRISE project (Semiconductor Using Nanostructures for Record Increases in Solar-cell Efficiency). The goal of this project is to investigate solar cell using simulation and characterisation to integrate them into concentrator to increase their efficiency to value higher than 40%.

The simulations used in Figures 2-18, 3-6, 3-15, 3-16, 3-20, 3-21 and 3-27 were performed by Alex Walker, PhD student. The simulation model used to generate Figure 3-28 was developed by Florent Chagnoleau. Figures 2-7 and 2-8 were provided by Dr. Christopher E. Valdivia, PDF, University of Ottawa. Figures 4-4, 4-5 and 4-6 were provided by Artur Turala, PDF, Université de Sherbrooke. The mesa structure resistance calculation method developed in section 3.3-2.2 is original.

- The above work has led to the following papers:

1. G.Kolhatkar, J.F. Wheeldon, C.E. Valdivia, S. Fafard, A. Turala, A. Jaouad, R.Ares, V.Aimez, K. Hinzer, "Time-dependent analysis of AlGaAs/AlGaAs tunnel junctions for high efficiency multi-junction solar cells," *Photonics North 2010*, Niagara Falls, Canada, 2010.
2. A.Walker, J.F. Wheeldon, C.E. Valdivia, G. Kolhatkar, K. Hinzer. "Simulation, modeling and comparison of III-V tunnel junction designs for high efficiency

metamorphic multi-junction solar cells," *Photonics North 2010*, Niagara Falls, Canada, 2010.

3. J. F. Wheeldon, C. E. Valdivia, A. Walker, G. Kolhatkar, A. Jaouad, A. Turala, B. Riel, D. Masson, S. Fafard, R. Ares, V. Aimez, T. J. Hall, K. Hinzer, "Performance Comparison of AlGaAs, GaAs and InGaP Tunnel Junctions for Concentrated Multi-Junction Solar Cells," *Prog. in Photovoltaic Res. and Appl.*, 2010.

4. J. F. Wheeldon, C. E. Valdivia, A. Walker, G. Kolhatkar, T. J. Hall, K. Hinzer, D. Masson, B. Riel, S. Fafard, A. Jaouad, A. Turala, R. Ares and V. Aimez, "GaAs, AlGaAs and InGaP tunnel junctions for multi-junction solar cells under concentration: Resistance study," *International Conference on Concentrating Photovoltaic Systems (CPV-6),* Freiburg, Germany, 2010.

5. J. F. Wheeldon, C. E. Valdivia, A. Walker, G. Kolhatkar, T. J. Hall, K. Hinzer, D. Masson, S. Fafard, A. Jaouad, A. Turala, R. Arès, V. Aimez, "AlGaAs tunnel junction for high efficiency multi-junction solar cells: Simulation and measurements of temperature-dependent operation," *34th IEEE Photovoltaic Specialist Conference 2009,* Philadelphia, PA, USA, pp. 135, 2009.

- Portions of the results in this thesis were presented at the following conferences:

1. G.Kolhatkar, J.F. Wheeldon, C.E. Valdivia, S. Fafard, A. Turala, A. Jaouad, R.Ares, V.Aimez, K. Hinzer, "Time-dependent analysis of AlGaAs/AlGaAs tunnel junctions for high efficiency multi-junction solar cells," oral presentation at *Photonics North 2010*, Niagara Falls, Canada, 2010.

2. Turala, A. Jaouad, P. Demolon, G. Kolhatkar, C.E. Valdivia, D. Masson, S. Fafard, K. Hinzer, R. Arès, V. Aimez. "Transparent indium tin oxide front-side electrode for high efficiency multi-junction III-V/Ge solar cells," oral presentation at *Photonics North 2010*, Niagara Falls, Canada, 2010.

3. J. F. Wheeldon, C. E. Valdivia, A. Walker, G. Kolhatkar, T. J. Hall, K. Hinzer, D. Masson, B. Riel, S. Fafard, A. Jaouad, A. Turala, R. Arès, V. Aimez, "GaAs, AlGaAs and InGaP tunnel junctions for multi-junction solar cells under concentration: Resistance study," *International Conference on Concentrating Photovoltaic Systems (CPV-6),* Freiburg, Germany, 2010.

4. J. F. Wheeldon, C. E. Valdivia, A. Walker, G. Kolhatkar, T. J. Hall, K. Hinzer, D. Masson, S. Fafard, A. Jaouad, A. Turala, R. Arès, V. Aimez, "AlGaAs tunnel junction for high efficiency multi-junction solar cells: Simulation and measurements of temperature-dependent operation," *34th IEEE Photovoltaic Specialist Conference 2009,* Philadelphia, PA, USA, pp. 135, 2009.

Acknowledgements

I would like to thank my supervisor, Dr. Karin Hinzer for her enthusiasm and her guidance all along this project. I am grateful to the SUNLab members Dr. Chris Valdivia and Dr. Jeff Wheeldon for their supervision, Alex Walker and Mark Yandt for their support. I would like to acknowledge Florent Chagnoleau for his assistance in analysing the equivalent circuit of the TJ.

I would like to thank Dr. Richard Ares, Dr. Vincent Aimez, Dr. Artur Turala and Dr. Abdelatif Jaouad from the Université de Sherbrooke for fabricating the samples, as well as Dr. Simon Fafard, Dr. Bruno Riel, Dr. Denis Masson and Eric Desfonds from Cyrium Technologies Inc. for providing the materials used to fabricate the samples.

I would like to acknowledge the Natural Sciences and Engineering Research council (NSERC), Canadian Foundation for Innovation (CFI), Canada Research Chair and Ministry of Research and Innovation (MRI) for financial support.

I am grateful to Dr. Emery Fortin for introducing me to experimental research and supporting me in the course of my studies.

I would like to thank family for their encouragement. I would like to thank my boyfriend for his unfailing support.

Table of Contents

List of Figures

Number *Page*

List of Tables

Number *Page*

List of Abbreviations

AM: Air mass

ARC: Antireflection coating

DNI: Direct normal incidence

DUT: Device under test

fcc: Face-centered cubic

FF: Fill factor

ITO: Indium tin oxide

MIS: Metal insulator semiconductor

MJ: Multi-junction

MOCVD: Metalorganic chemical vapor deposition

ND: Neutral density

NDR: Negative differential resistance

RF: Radio frequency

RTD: Resistance temperature detector

SEM: Scanning electron microscopy

TCO: Transparent conductive oxide

TEC: Thermo-electric cooler

TJ: Tunnel junction

TLM: Transmission line measurements

List of Symbols

a: Lattice constant (Å)
C: Capacitance (F)
D : diffusion coefficient (cm^2·sec)
d : spacing between two adjacent TLM pads (μm)
$\hat{\mathbf{E}}$: Electric field (volt/cm)
E_C: Energies at the edge of the conduction band (eV)
E_g: Energy gap (eV)
E_V: Energies at the edges of the valence band (eV)
E_F: Fermi energy (eV)
$F(E)$: Fermi-Dirac distribution function.
FF: Fill factor (%)
$\hbar$: Planck's constant (joules·sec)
I: Current (A)
I_{SC}: Short circuit current (A)
J: Current density (A/cm^2)
J_{excess}: Excess current-density (A/cm^2)
J_P: Peak current density (A/cm^2)
J_{SC}: Short circuit current-density (A/cm^2)
J_V: Valley current density (A/cm^2)
k_B: Boltzmann constant
L: Inductance (H)
m^*: Effective mass (kg)
n: Electron concentration (cm^{-3})
N_C: Effective density of state in the conduction band (cm^{-3})
N_V: Effective density of state in the valence band (cm^{-3})
p: Holes concentration (cm^{-3})
P_{MP}: Maximum power (W)
P_S: Incident light power density (W/cm^2)
r_1: inner radius of a Corbino (μm)
r_2: outer radius of a Corbino (μm)
R: Resistance (Ω)
R_{CH}: Characteristic resistance (Ω)
R_N: Resistance of the n-layer of a TLM pad (Ω)
R_{NTJ}: Resistance of the n-layer of a TJ (Ω)

R_{NC}: Resistance of the *n*-contact of a TLM pad (Ω)
R_{NCTJ}: Resistance of the *n*-contact of a TJ (Ω)
R_{NS}: Sheet resistance of the *n*-layer (Ω/□)
R_P: Resistance of the *p*-layer of a TLM pad (Ω)
R_{PTJ}: Resistance of the *p*-layer of a TJ (Ω)
R_{PC}: Resistance of the *p*-contact of a TLM pad (Ω)
R_{PCTJ}: Resistance of the *p*-contact of a TLM pad (Ω)
R_{PS}: Sheet resistance of the *p*-layer (Ω/□)
R_S: Series resistance (Ω)
R_{SH}: Shunt resistance (Ω)
R_T: Total resistance (Ω)
R_{TOT}: Total mesa resistance of a tunnel junction device (Ω)
R_{TJ}: Resistance of a tunnel junction (Ω)
R_C: Contact resistance (Ω)
T: Temperature (K)
T: thickness (μm)
s: spacing between the inner and the outer metal contact of a Corbino (μm)
V: Voltage (V)
V_{OC}: Open circuit voltage (V)
V_P: Peak voltage (V)
V_V: Valley voltage (V)
$V(r)$: Periodic potential (V)
W: width of a TLM pads (μm)
W_C: area of the inner metal contact of a Corbino (cm^2)
Z: Length of a TLM pads (μm)
η: Efficiency of a solar cell (%)
θ: the incident angle (°)
μ_n : electron mobility ($cm^2/V \cdot sec$)
μ_p : hole mobility ($cm^2/V \cdot sec$)
ρ: resistivity (Ω·cm)

Chapter 1 - Introduction

Nowadays, the world is facing an energy crisis. Oil consumption keeps increasing and has now reached four times its discovery rate. In addition to targeting energy consumption reduction, inexpensive, renewable and efficient alternative energy sources have to be found. Solar energy could play an important role in addressing this challenge. The most efficient and portable method to exploit this solar energy is through the use of solar cells. Solar cells absorb the Sun's photons, generating an electron-hole pair in the process. The cell's *p-n* junction separates the pair and the electrical circuit is closed by introducing a load, leading to electricity generation. Solar cells fabricated with silicon are already available, but their efficiency is limited and only goes up to 21% in present widely available products. They absorb only a fraction of the overall solar spectrum, which limits their performance. Multi-junction (MJ) solar cells provide an alternative to silicon solar cells. They are built with sub-cells of varying bandgap energies fabricated using monolithically stacked *p-n* junctions, enabling them to absorb a wider range of the solar spectrum.

One of the major challenges in MJ solar cell design is to conduct current between each *p-n* junction. This can be accomplished by introducing tunnel junctions (TJ), which interconnect the three *p-n* junctions. A TJ is a highly doped *n-p* junction that connects the *n*-terminal of one sub-cell to the *p*-terminal of the adjacent sub-cell. These TJ are still not well understood and require testing to determine the most appropriate design to achieve the highest overall efficiency in the MJ solar cell. This project consists of experimentally measuring current-voltage characteristics of tunnel junctions under different conditions, including the effects of temperature on their operation and their time-dependent behavior. In addition to obtaining the tunneling peak value, the results of this work help calibrating numerical models developed within our research group. Triple junction GaInP/InGaAs/Ge solar cells which incorporate these tunnel junctions are also tested under low concentration

artificial sunlight using an Oriel solar simulator capable of achieving intensities of up to 150 times the intensity of the sun.

The photovoltaic effect was first discovered in 1839 by Edmund Becquerel [1] but the first photovoltaic devices were only built forty years later using selenium. It was observed that when illuminating selenium with light, current could be produced spontaneously without using a power supply. This discovery led to the fabrication of the first solar cell in 1894 by Charles Fritts, which consisted of a layer of selenium deposited between gold and a layer of another metal [2-4].

In the 1950s, the first solar cells potentially capable of producing a useful quantity of power were developed. These solar cells, also called first generation solar cells were fabricated using silicon wafers. They consisted of a single silicon *p-n* junction. Chapin, Fuller and Pearson fabricated the first silicon solar cell in 1954, which attained an efficiency of 6% [5]. Between the 1950s and the 1970s, work was done on silicon solar cells, leading to an increase in their efficiency. Due to their cost, they were only used for space applications.

The 1970's energy crisis led to increased interest in alternative sources. Solar cells developed using different materials called thin film solar cells appeared. These thin film solar cells are named second generation solar cells. Tandem cells, solar cells using two *p-n* junctions, were also studied. The first MJ solar cell, reported in 1983 by the Carolina State University was a tandem cell and had an efficiency of ~16%. Also during the 1980s, organic materials were investigated, leading to the first organic solar cells [6-7], which had efficiencies of 1%. In 1999, the first triple-junction solar cell was fabricated. It attained efficiencies higher than all the solar cells previously developed, with a value of ~30%. Figure 1-1, illustrates the different types of solar cells, developed using different materials: silicon solar cells (efficiency of up to 21%), organic solar cells (efficiency on the order of 7%) [3, 8, 9], thin film solar cells (efficiency up to 19%) [10] and high-efficiency MJ solar cells (reached up to 41.1% efficiency).

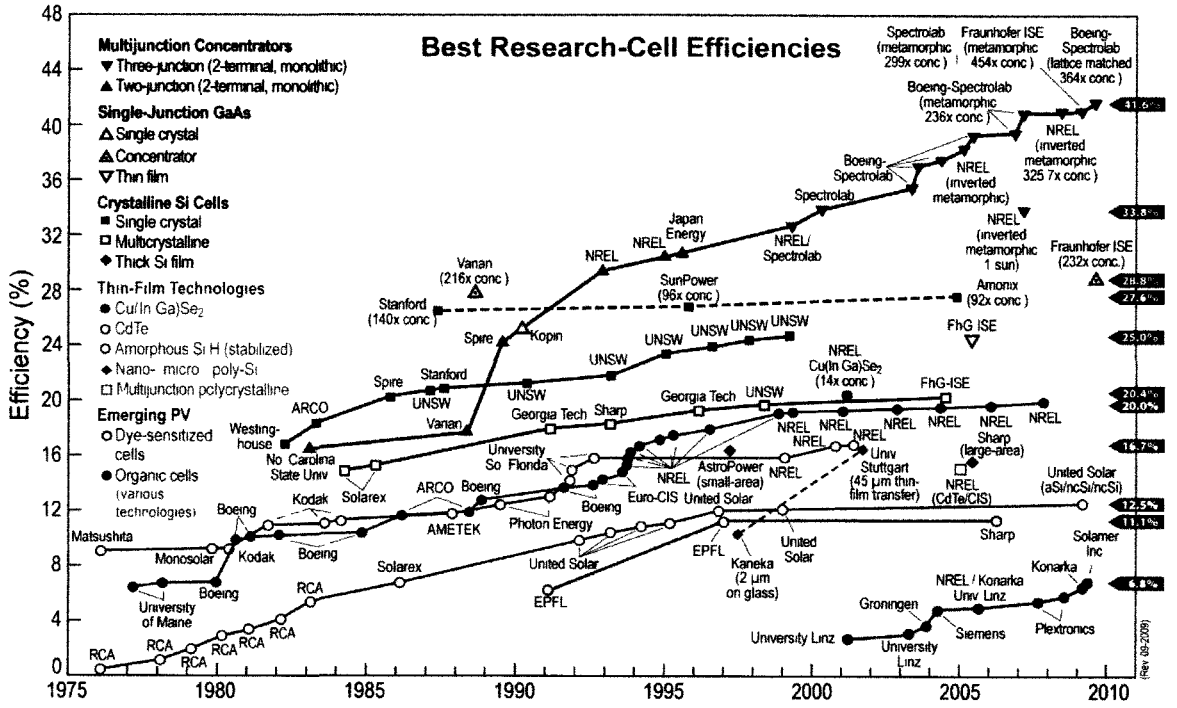

Figure 1-1: Best research-cell efficiencies since 1975 as compiled by the National Renewable Energy Laboratory [11].

Today, thin film cells are the cheapest to fabricate, with an efficiency of ~15% in products. MJ solar cells must be combined with concentrating systems to minimise the size of the cell for a given power in the system and therefore become cost competitive with thin film technology.

The main goal of this research is to provide further understanding of MJ high efficiency solar cells for high concentration by experimentally studying TJ fabricated with different materials (ex. AlGaAs/AlGaAs). By studying the impact of the different materials on their current density-voltage (*J-V*) characteristics, the most suitable TJ to incorporate in high efficiency solar cells can be determined. AlGaAs/AlGaAs TJ are studied in this project. This material was chosen because it allows more flexibility in the optimisation of the device. Adding Al can be used to change the energy band alignment and optimise the current going through the solar cell while still remaining lattice-matched materials. Depending on the location and the system integration, solar cells on Earth are subjected to a variation of temperature, from -40 to 65°C. To ensure they are still able to conduct the current density

with this variation in operating conditions, the effects of temperature on the *J-V* curves of these TJ are studied. A challenge is to characterise TJ over their full operating range. When time-averaged measurements are performed, part of the information of the *J-V* curve is lost. Performing a time-dependent analysis of their *J-V* curve provides us with a better understanding of the TJ behavior, especially the maximum current density at which the full MJ solar cell can operate using this type of TJ. Furthermore, it allows us to accurately calibrate the simulations over their full operating range. Full triple junction GaInP/InGaAs/Ge solar cells which incorporate these TJ are also studied. On these solar cells, a transparent electrode fabricated using an indium tin oxide (ITO) layer is deposited in the hope of decreasing the fabrication steps and therefore reducing the cost of the solar cells.

The first tunnel diode was discovered by Esaki in 1958 [12], who was later awarded the Nobel prize in physics for discovering the electron tunneling effect which explained the behaviour of the tunnel diode. He observed for the first time a negative differential resistance region on the current-voltage behavior of a germanium *p-n* junction. In the following years, work was done on understanding the physics of TJ [13]. Different materials were investigated and a Ge/GaAs heterojunction was developed in 1962 [14]. In 1984, the first AlGaAs/GaAs TJ was reported by Hickmott *et al.* [15]. While this project focuses on AlGaAs/AlGaAs TJ and AlGaAs/InGaP TJ, devices fabricated using GaAs/GaAs were studied experimentally and numerically in the past [16-18]. Previous research has presented the effects of variation of doping concentration on the resistance of three TJ types [19]. TJ are an important area of research. One of their applications is to conduct the current between the sub-cells of MJ solar cells. Many groups around the world are studying solar cells. An important one is the Fraunhofer Institute for Solar Energy Systems, in Germany, that has developed solar cell models, and reported in 2009 an efficiency of 41.1% for a MJ solar cell [20]. III-V semiconductor TJ can also be used in other applications such as long-wavelength vertical-cavity surface-emitting lasers (LW-VCSEL) [21].

Chapter 2 of this work presents the background theory necessary to the understanding of solar cell operation. Starting from an overview of the basic properties of III-V

semiconductors, *p-n* junctions are depicted, in particular their behavior under applied bias. Then the structure and the operation of a MJ solar cell are described. A section of this chapter is dedicated to the theory of TJ, which are critical to conduct current through a MJ solar cell. Finally, the band energy diagram of a MJ solar cell is explained.

In Chapter 3, TJ are studied experimentally. Two AlGaAs/AlGaAs TJ samples with different internal resistances are measured using the time-averaged method. These resistances are calculated using two methods, the TLM method and the Corbino method to determine the most accurate technique. The *J-V* characteristics of the TJ are studied as a function of temperature. A *J-V* curve consists of three different regions, one of which, called the negative differential resistance (NDR) region, is unstable. Due to the unstable nature of the NDR region, important information is obscured on the time-averaged measurements. A time-dependent analysis of this NDR region is provided. Finally, a TJ fabricated with a different material is presented, InGaP/AlGaAs. Both materials are compared to determine the most suitable to integrate in a MJ solar cell design.

Chapter 4 moves on to the measurements of full MJ solar cells. In this chapter, solar cells fabricated using ITO, a transparent conductive oxide (TCO), are measured and their performance is compared with a reference standard top metal grid solar cell. Three different designs are studied and compared to determine the most efficient. A detailed description of the experimental setup is provided. A section is dedicated to the calibration of the solar simulator, to determine accurately the intensity of the light shone on the solar cells.

The last chapter ends with general conclusions and proposed future work. Two appendixes are included. Appendix A discusses the derivation of the correction factor used to calculate the internal resistances of a TJ using Corbinos. Appendix B presents the uncertainties relative to the measurements and includes an example of the calculations of the uncertainty on the internal resistances values.

These are the samples measured in this work. Table 1 was made for reference. Further details will be provided in the following chapters.

Table 1: Table of the samples studied in this work.

Sample name	Sample type	Specifications
TJ1-A	AlGaAs/AlGaAs tunnel junctions	- Au/Ti contacts - High mesa resistance - Nonlinear *p*-contact resistance
TJ1-B	AlGaAs/AlGaAs tunnel junctions	- Zn/Au *p*-type contacts and Ti/Au *n*-type contacts - Low mesa resistance - Linear *p*-contact resistance
TJ2	AlGaAs/InGaP tunnel junctions	- High mesa resistance (~9 Ω)
ITO-A1	ITO solar cell-Design A	- No top metallic electrode - No passivation
ITO-A2	ITO solar cell-Design A	- No top metallic electrode - Top sub-cell chemically passivated
ITO-B1	ITO solar cell-Design B	- Two fingers deposited under the ITO layer
ITO-C1	ITO solar cell-Design C	- 100% of top metallic electrode fingers deposited under the ITO layer
ITO-C2	ITO solar cell-Design C	- 90% of top metallic electrode fingers deposited under the ITO layer
ITO-C3	ITO solar cell-Design C	- 40% of top metallic electrode fingers deposited under the ITO layer

Chapter 2 – Background

This chapter presents the background knowledge on solar cell design and operation. First, the fundamental properties of III-V semiconductors are described. This is followed by theory of *p-n* junctions as applied to semiconductor devices. The next part presents an overview of solar cell operation processes, in particular the impact of external parameters such as the temperature and the intensity of the light on their *J-V* characteristics. Finally, a section is dedicated to the understanding of tunnel junction theory, specifically their behavior under applied voltage biases. Their *J-V* characteristics are studied, and the influence of temperature and the resistance of their structure is explained. Two standard methods used to determine this resistance, the transmission line measurement method and the Corbino method, are presented in this work. In the last part, the band structure of a multi-junction solar cell is explained.

2.1 III-V Semiconductor Materials

2.1-1 Crystal structure of III-V semiconductors

A crystal consists of a series of periodically spaced atoms. The most commonly used crystalline semiconductor is Si, a group IV material, where each atom is covalently bonded to four nearest neighbours. III-V semiconductors are compound semiconductors, made from a combination of group III atoms, i.e Al, Ga and In and group V atoms, i.e. As and P of the periodic table. The number III or V refers to the number of valence electron per atom available for biding. III-V compounds like GaAs (galium arsenide) have the zincblende crystal structure illustrated in Figure 2-1, which consists of two interpenetrating face-

Figure 2-1: Zincblende structure of GaAs; from Ref. [23] p. 38.

centered cubic (fcc) displaced from each other by (¼, ¼, ¼)*a*, where *a* is the lattice constant [22]. In GaAs, one fcc is composed of Ga while the other is consists entirely of As. The properties of III-V semiconductors can be explained by studying their bond structure and band structure.

2.1-2 Bond structure

Two atoms in the lattice are bonded together by a covalent bond consisting of two electrons. Each atom is connected in this way to four other atoms, or nearest neighbours, and surrounded by eight electrons. At low temperature, these electrons cannot move and the semiconductor acts like an insulator. When the temperature is increased, the electrons gain some kinetic energy from lattice vibrations. Due to this energy, some can break free from the bond, becoming free electrons, and can conduct current. When an electron is freed from a bond, a hole is created in its place. The neighbouring electrons can move to fill this hole, which will move through the lattice as if it had a positive charge. Therefore, current transport comes from the electrons and the holes. Electrons and holes are called charge carriers [24].

2.1-3 Band structure

The band structure describes this behavior of the electron in the form of an energy diagram presenting different energy levels. The electrons in the covalent bonds are in the valence band, while the free electrons are excited into the conduction band. At 0 K, the conduction band is completely empty, and all the electrons are in the valence band. The valence band and the conduction band are separated by an energy gap E_g, corresponding to the minimum energy needed for an electron to move from the valence band to the conduction band [25]. The electrons can be moved from the valence band to the conduction band by thermal excitation, but also by absorbing the energy of a photon, i.e. photon excitation. If a semiconductor is exposed to a source of energy greater than the bandgap, a photon can be absorbed by a valence electron and excite an electron into the conduction band, creating an electron-hole pair. Because of the periodicity of the lattice, the free electrons act like nearly-free particles in the crystal lattice submitted to a periodic potential. Therefore, they obey Bloch's theorem, which states that the wavefunction of a particle in a periodic potential can be written as the product of a plane wave times a periodic function having the same periodicity.

The band structure is the relationship between the energy and the wave vector $\mathbf{k}$ which is linked to the momentum $\mathbf{p}$ by the relation $\mathbf{p} = \hbar\mathbf{k}$. The band structure is obtained by solving Schrödinger's equation for the one-electron model with a periodic potential $V(\mathbf{r})$ given by [26]

$$\left[\left(-\frac{\hbar^2}{2m^*}\nabla^2 + V(\mathbf{r})\right)\right]\phi_{\mathbf{k}}(\mathbf{r}) = E_{\mathbf{k}}\phi_{\mathbf{k}}(\mathbf{r}), \tag{2.1.1}$$

where $\hbar$ is Planck's constant and m^* is the effective mass of the electrons given by [26]

$$m^* = \frac{\hbar^2}{\left(\frac{\partial^2 E}{\partial k^2}\right)}. \tag{2.1.2}$$

The solution of this equation is the Bloch wavefunction $\phi_{\mathbf{k}}(\mathbf{r})$. It is the product of a plane-wave $e^{i\mathbf{k}\cdot\mathbf{r}}$ and a wavefunction $U_{\mathbf{k}}(\mathbf{r})$ with the periodicity of the lattice, and is given by [27]

$$\phi_{\mathbf{k}}(\mathbf{r}) = e^{i\mathbf{k}\cdot\mathbf{r}} U_{\mathbf{k}}(\mathbf{r}). \tag{2.1.3}$$

Figure 2-2 shows the band structure of Si and GaAs. **k** is varied from 0 to π/a along the x y and z axis. The lattice being a periodic structure with period a, and knowing $E(\mathbf{k})=E(-\mathbf{k})$ the wavevector repeats itself with a period $2\pi/a$. Near the bottom of the conduction band and the top of the valence band, the energy can be expressed as [26]

$$E(\mathbf{k}) = \frac{\hbar^2 \mathbf{k}^2}{2m^*}, \tag{2.1.4}$$

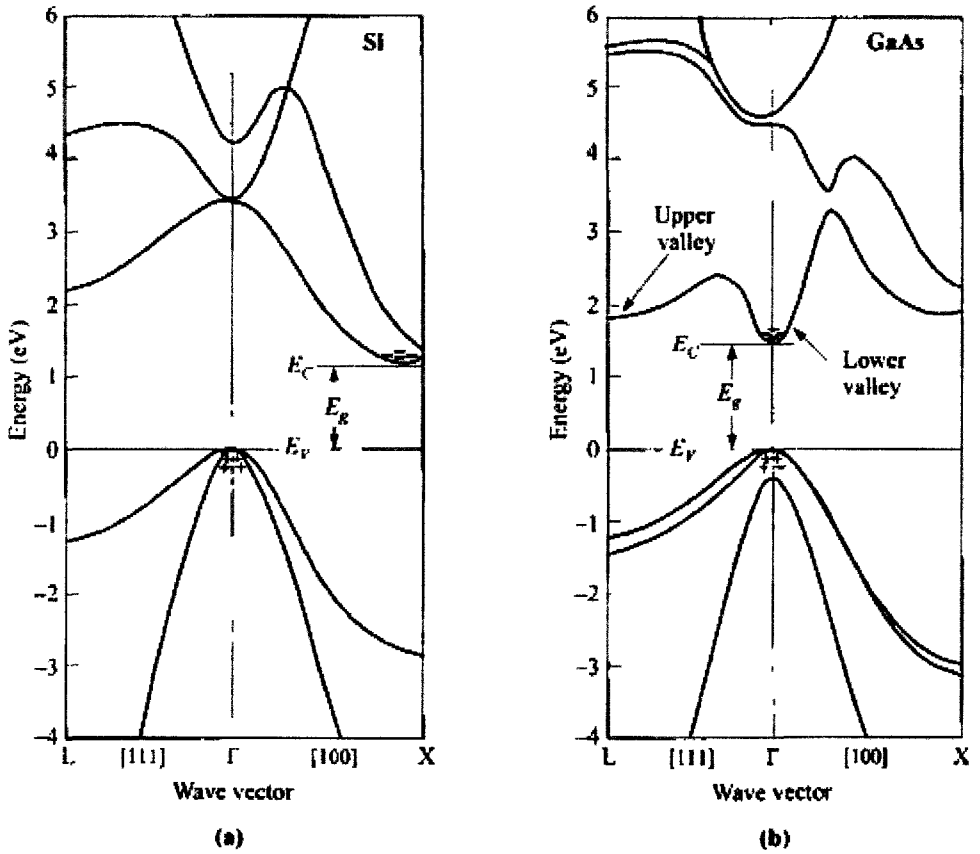

Figure 2-2: Energy-band structure of (a) Si and (b) GaAs where the maximum of the higher valence band and the minimum of the lower conduction band occur at the Γ point; from Ref. [26] p. 14.

GaAs is a direct bandgap semiconductor while Si has an indirect bandgap. Direct bandgap occurs when the maximum of the valence band is aligned with the minimum of the covalence band. In this case, an electron needs to absorb a photon to jump to the excited state. Otherwise, the semiconductor is called indirect bandgap semiconductor. In the case, more than one particle is needed for an electron to go from the valence band to the conduction band. Thus, there is a higher transition probability in the case of a direct bandgap semiconductor.

The bandgap is highly dependent on the composition of the III-V semiconductor and on the lattice constant, as shown in Figure 2-3. This dependence is important in the choice of the materials used in solar cells, as it will be explained later on. The energy gap varies with temperature. As the temperature increases, the bandgap becomes narrower, and the relationship between the energy gap and the temperature is given by

$$E_g(T) = E_g(0) - \frac{\alpha T^2}{T + \beta}, \tag{2.1.5}$$

where α and β are constants depending on the material and $E_g(0)$ is the energy gap at 0 K [28].

2.1-4 Doping

Conductivity inside a semiconductor can be improved by increasing several parameters such as temperature and carrier concentration, or decreasing the bandgap. When the energy gap is narrower, it takes less energy for an electron to jump into the excited state, and electrons can be moved into the conduction band more easily. Impurities, or dopants, can be added to a semiconductor to change the carrier concentration. There are two types of dopants. The *n*-type doping consists in adding atoms with more valence electrons. In an *n*-doped material, electrons are majority carriers and holes are minority carriers. The other type

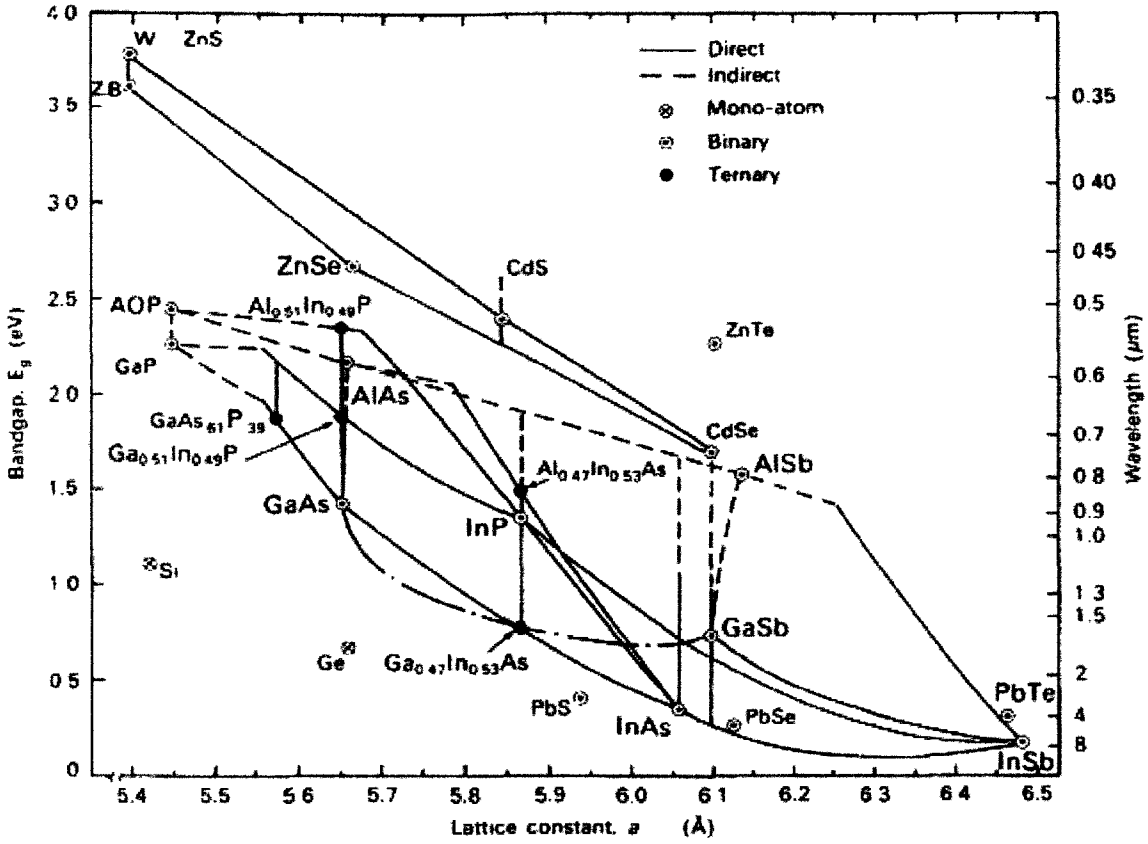

Figure 2-3: Bandgap of common compound structures as a function of their composition or lattice constant; from Ref. [29].

of dopant is the *p*-type doping which uses atoms with fewer valence electrons. Inversely, in *p*-doped materials, holes are majority carriers and electrons are minority carriers. Impurities that add an electron to the conduction band are called donors, while impurities adding holes to the valence band are called acceptors. These impurities give rise to additional levels within the energy gap, called quasi-Fermi levels, making it easier for an electron to jump to the conduction band.

Carrier concentration depends on the density of states and the probability an electron will occupy a state. The electron distribution over the energy states obeys the Fermi-Dirac distribution function [26]

$$F(E) = \frac{1}{1+\exp\left[\frac{(E-E_F)}{kT}\right]}, \tag{2.1.6}$$

where k is the Boltzmann constant and E_F is the Fermi energy. In the case of intrinsic semiconductor E_F is located in the center of the bandgap. However, when a semiconductor is doped, the Fermi level is shifted to preserve charge neutrality, as shown in Figure 2-4. If the semiconductor is p-doped, E_F is lowered, whereas it is n-doped, E_F is increased.

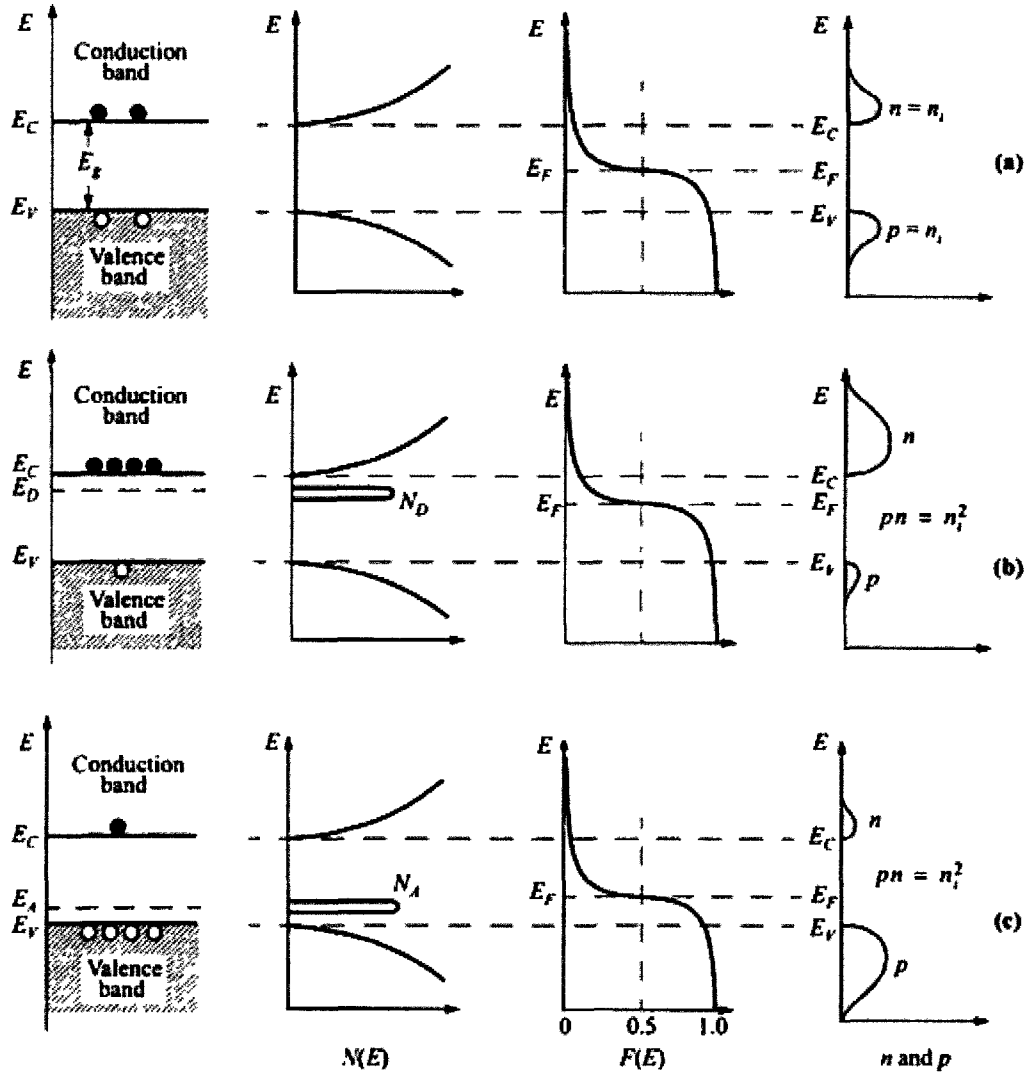

Figure 2-4: Schematic band diagram, density of states, Fermi-Dirac distribution and carrier concentration for (a) intrinsic (b) n-type (c) p-type semiconductors at thermal equilibrium; from Ref. [26] p. 24. E_A and E_D are the quasi-Fermi levels of holes and electrons.

The density of states describes the number of available states at each energy level. In the conduction band, it is given by

$$D_{\mathrm{C}}(E)=\frac{1}{2\pi^2}\left(\frac{2m_{\mathrm{C}}^*}{\hbar^2}\right)^{3/2}\left(E-E_C\right)^{3/2}, \tag{2.1.7}$$

and in the valence band

$$D_{\mathrm{V}}(E)=\frac{1}{2\pi^2}\left(\frac{2m_{\mathrm{V}}^*}{\hbar^2}\right)^{3/2}\left(E_{\mathrm{V}}-E\right)^{3/2} \tag{2.1.8}$$

where m^*_{C} and m^*_{V} are the effective masses of electrons and holes and E_{C} and E_{V} are the energies at the edges of the conduction band and the valence band respectively [26].

The number of electrons in the conduction band is defined as the product of the number of states available in the conduction band and the Fermi-Dirac distribution $F(E)$ given by Eq. (2.1.6) integrated over the conduction band [26]

$$n(E)=\int_{E_{\mathrm{C}}}^{\infty} D_C(E)F(E)\mathrm{d}E. \tag{2.1.9}$$

Integrating gives the electron concentration [26]

$$n=N_{\mathrm{C}}\exp\left(-\frac{E_{\mathrm{C}}-E_{\mathrm{F}}}{kT}\right), \tag{2.1.10}$$

where N_{C} is the effective density of state in the conduction band given by [26]

$$N_C=2\left(\frac{m_C^*kT}{2\pi\hbar^2}\right)^{3/2}. \tag{2.1.11}$$

Similarly for a *p*-type semiconductor, the number of holes in the valence band is defined as [26]

$$p(E) = \int_{\infty}^{E_V} D_V(E)[1 - F(E)]\mathrm{d}E, \tag{2.1.12}$$

and the holes concentration in the valence band can be expressed as [26]

$$p = N_V \exp\left(-\frac{E_F - E_V}{kT}\right), \tag{2.1.13}$$

where the valence band effective density of states N_V is given by [26]

$$N_V = 2\left(\frac{m_V^* kT}{2\pi\hbar^2}\right)^{3/2}. \tag{2.1.14}$$

2.1-5 Carrier recombination and generation

Electrons and holes can be created by different processes. To increase the number of carriers, also referred to as carrier generation, additional energy is required. This energy can come from phonons (vibrations within the lattice), from the absorption of a photon by light excitation, from the kinetic energy of other carriers, or from an increase of temperature also referred to as thermal excitation. Carriers can also recombine. In this case, the number of carrier is decreased, releasing energy. Recombination is due to the relaxation of an excited electron from the conduction band to a lower energy state.

2.1-6 *p-n* junctions

A *p-n* junction is created by joining a *p*-type semiconductor material and an *n*-type semiconductor material, as illustrated in Figure 2-5(a). Because of the difference in carrier concentration between both sides of the junction, holes from the *p*-side diffuse into the *n*-side, and similarly electrons from the *n*-side diffuse into the *p*-side, creating ionized acceptors and ionized donors on the *p*-side and the *n*-side respectively. A negative space charge is formed on the *p*-side of the junction, while a positive space charge is formed on the

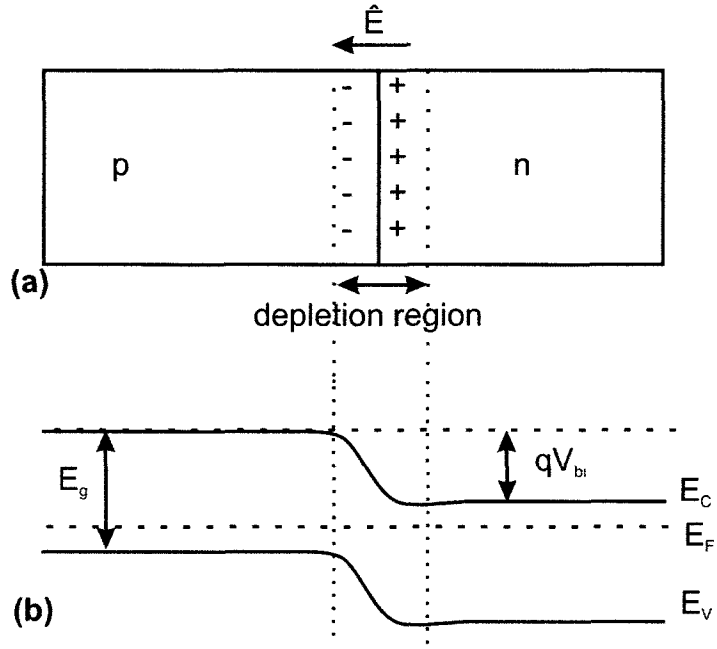

Figure 2-5: (a) Schematic of a *p-n* junction and (b) energy band diagram of a *p-n* junction as a function of position.

p-side of the junction. At the interface between the *p*-side and the *n*-side, a region with no charged particles, called the depletion region, is created [30]. An electric field $\hat{\mathbf{E}}$, called the built-in electric field is formed in the process in the direction opposite to the diffusion current of both carriers, limiting the diffusions of holes and electrons to reach equilibrium [31-32]. Since the energy of the carriers is closely linked to the electric field inside the material, the energy diagram will change, as shown in Figure 2-5 (b). The electric field induces a shift inside the valence and the conduction band. Knowing

$$\hat{\mathbf{E}} = -\frac{dV}{dx}, \tag{2.1.15}$$

the electric field gives rise to a potential gradient in the direction opposite to the electric field. This potential is called the built-in potential and noted V_{bi}. $\hat{\mathbf{E}}$ exists only within the depletion region and therefore, the potential is constant outside. Furthermore, the energy is given by $E=qV$, where q is the charge of a particle and V is the potential. Thus, the energy band diagram is higher on the *p*-side than on the *n*-side. Furthermore, at equilibrium the

Fermi energy level has to be constant throughout the material for the carrier concentration to be uniform [33].

While the diffusion current density (J_{diff}) is created by the concentration gradient, a current referred to as drift current density (J_{drift}) is created by the drift of carriers in the electric field. Four current density components are uncovered in this system, the drift current density of the electrons and the diffusion current density from the holes going from the *n*-side to the *p*-side, and inversely, the drift current density of the holes and the diffusion current density of the electrons going from the *p*-side to the *n*-side. Since electron current is always opposite to the direction of the electron flow, both diffusion current density component are directed from the *p*-side to the *n*-side and both drift current density component are directed toward the *n*-side. At equilibrium, the drift current density in $\hat{\mathbf{E}}$ is opposite to the diffusion current density. Thus, J_{drift} and J_{diff} of the electrons and holes are in balance and no current flows:

$$J_{drift} = -J_{diffusion}. \tag{2.1.16}$$

The diffusion and drift current densities of each carrier cancel out and the total current density is zero:

$$J_{eq} = 0 = q\mu_n nE + qD\nabla n = \mu_n n\frac{dE_F}{dx}, \tag{2.1.17}$$

where μ_n is the electron mobility and D is the diffusion coefficient.

When no voltage is applied, a large energy barrier prevents the electrons from going from the *n*-side to the *p*-side. When a voltage is applied, the separation of the energy band is affected, as well as the width of the depletion region. If a positive voltage bias is applied from the *p*-side to the *n*-side, or forward bias, the band diagram shifts, decreasing the energy difference between the *p*-side and the *n*-side. The potential barrier is lower by the applied voltage V_F. Electrons and holes can now overcome the barrier, inducing a current flow. As the voltage is increased, the barrier is lowered and more electrons can diffuse. The diffusion

current density can be large. When a voltage V_R is applied from the *n*-side to the *p*-side, or reverse bias, the potential barrier is increased by V_R. The potential barrier becomes so high that no electron can gain enough energy to overcome the barrier and diffuse from the *n*-side to the *p*-side. Hence, there is no current flow [33].

The electric field is also affected by an applied voltage bias. In forward bias, the applied electric field opposes $\hat{\mathbf{E}}$, hence the electric field at the junction is decreased. Inversely, in reverse bias, the applied field is in the same direction as $\hat{\mathbf{E}}$, which increases the electric field at the junction. A change in the electric field induces a change in the depletion region width. If $\hat{\mathbf{E}}$ is lower, there are fewer ionized donors and acceptor on each side and the width decreases, and inversely if $\hat{\mathbf{E}}$ is higher, the width increases [33].

2.1-7 Schottky barrier

Doped semiconductors can be joined to metals. When a metal is deposited on a semiconductor, a difference in the work function, or minimum potential required to free an electron, of both sides creates a barrier at the interface, called Schottky barrier [26]. When the metal and the semiconductors are in contact, E_F in the semiconductor is lowered by an amount equal to the difference between both work functions and the Fermi levels of both sides line up. Metal-semiconductor contacts behave like *p-n* junctions: an electric field is created at the interface, inducing a potential gradient in the depletion region. Metal-semiconductor contacts are often used, called Schottky contacts.

The case of the *n*-type semiconductor is illustrated on the left side of Figure 2-6. At thermal equilibrium, shown in Figure 2-6(a), the Fermi level is constant on both sides and no current flows. In forward bias, presented in Figure 2-6(b), the Fermi level increases inside the semiconductor, increasing the electron population in the conduction band. Electrons gain enough energy to go through the barrier and current flows. Five different processes are used to create current. Electrons can overcome the barrier by thermal excitation; others can tunnel through the barrier. Current can also be created by carrier recombination as well as diffusion

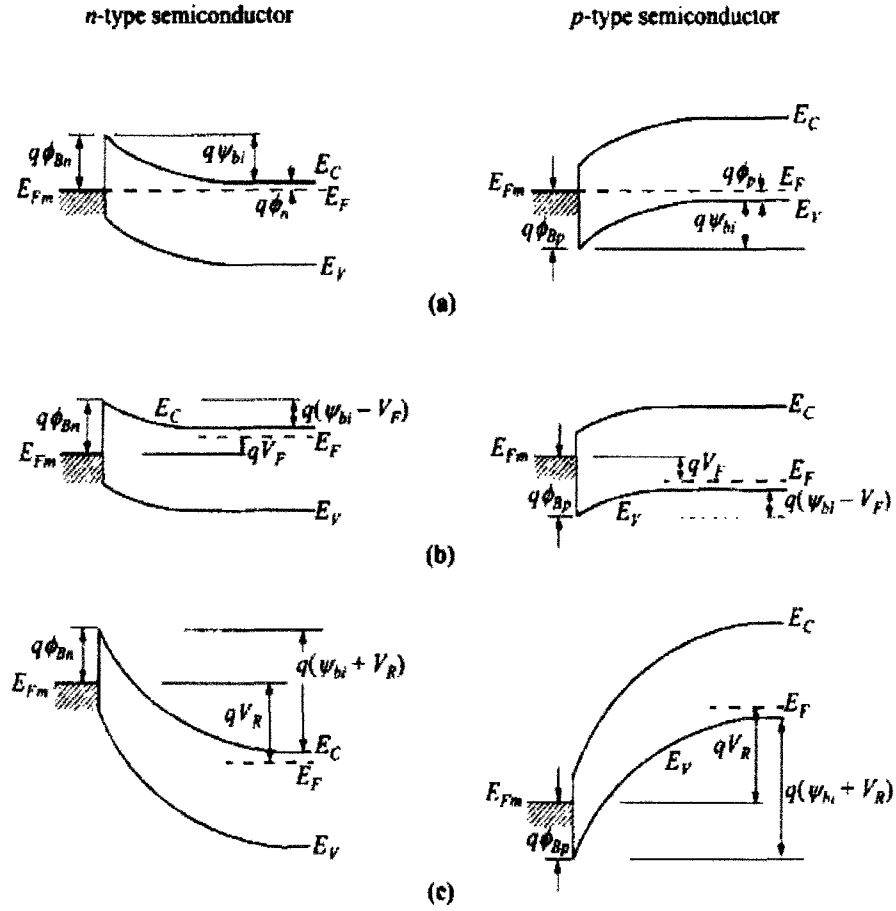

Figure 2-6: Schottky barrier energy band diagrams of metal on *p*-type (right) and *n*-type (left) semiconductors (a) at thermal equilibrium, (b) in forward bias and (c) reverse bias; from Ref. [26] p. 136.

of electrons and holes. Figure 2-6(c) shows the energy band diagram of a Schottky barrier in reverse bias. In this case, the barrier is increased and no current can flow. For a *p*-type semiconductor, the phenomenon is the same but for holes: the potential gradient is in the opposite direction, as depicted on the right side of Figure 2-6.

The Schottky barrier is independent of doping, thus a temperature variation will not affect its height. Furthermore, at higher temperature, the Fermi level increases, resulting in a higher population of electrons in the conduction band, thus more electrons tunnel through and higher current flows for a certain voltage and the resistance decreases [26].

2.2 Multi-junction Solar Cell Theory

2.2-1 Solar Spectrum

The intensity of sunlight, or irradiance is expressed in suns, 1 sun corresponding to 1 kW/m^2. This intensity varies with the distance from the sun. It is also influenced by the atmosphere between the sun and the device, which absorbs and reflects certain wavelengths of the light. Therefore, as the atmosphere is different terrestrially than extra-terrestrially, the spectrum of light in space is different from the one on Earth. The absorption is quantified by the air mass (AM) defined as [30]

$$AirMass = \frac{1}{\cos\theta}, \tag{2.2.1}$$

where θ is the incident angle. The air mass zero (AM0) is the radiation spectrum in space. It is not affected by the atmosphere and has a maximum intensity of 1.3 terrestrial suns [34]. It is similar to the black body radiation at 5800K. Two standard spectra are used to define the spectrum on Earth, AM1.5G having an intensity of 1 sun and AM1.5D which has an intensity of 0.9 suns [35]. AM1.5D represents the light on a straight path from the sun to the device only, or direct normal incidence (DNI), while AM1.5G also includes the light scattered by the atmosphere, or diffused light. The different spectra are illustrated in Figure 2-7.

2.2-2 Structure and Operation

Semiconductor devices such as solar cells are used to generate current. Charge separation is required in order to produce current. This can be achieved using a *p-n* junction. A standard solar cell consists of a single *p-n* junction. Under no illuminations, it behaves like

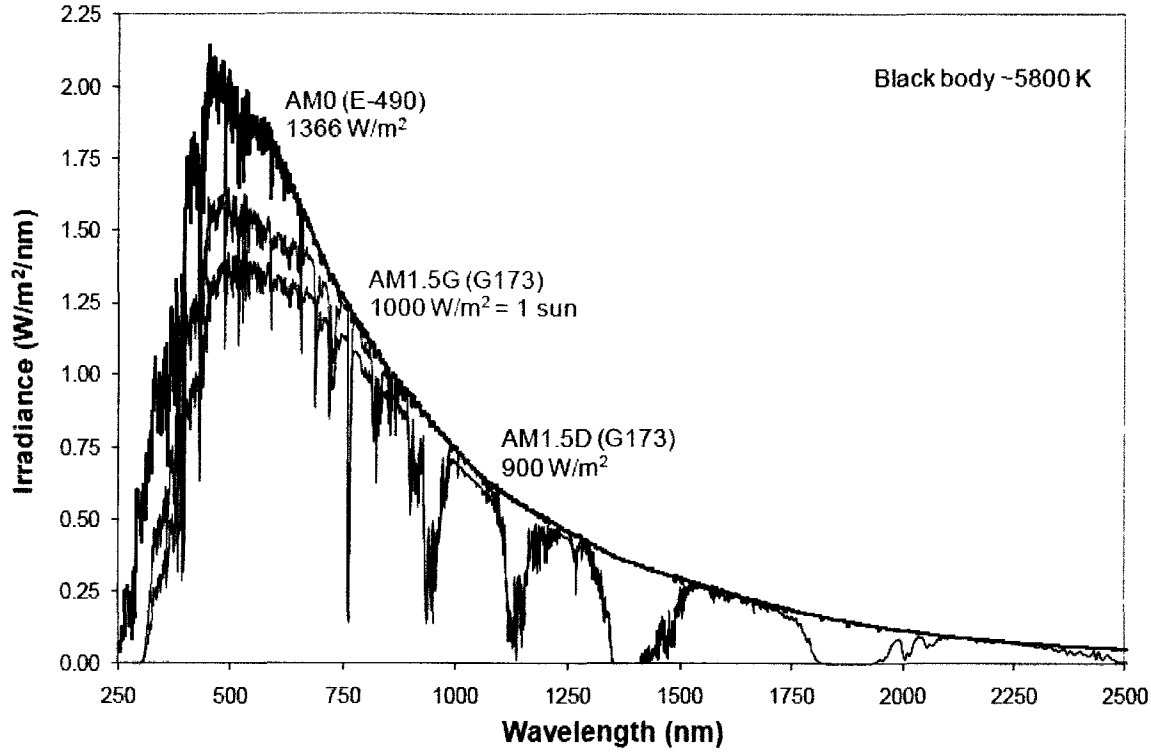

Figure 2-7 : Solar irradiance spectra under extraterrestrial (AM0) and terrestrial (AM1.5D and AM1.5G) illumination. [Courtesy of Christopher E. Valdivia]

a regular semiconductor diode. When it is illuminated by the sun, it absorbs the photons composing sunlight and converts them into electrical energy, creating both a current and a voltage [2].

A multi-junction solar cell consists of three III-V semiconductor *p-n* junctions of varying bandgap energies monolithically stacked as depicted in Figure 2-8(a). As illustrated in Figure 2-8(b), this enables it to absorb a broader range of the solar spectrum and achieve high conversion efficiencies, up to 40.7% [36] 40.8% [37] and 41.1% [20] using the AM1.5D spectrum under high concentration. The material with the larger bandgap is located at the top, and the one with the smaller bandgap is located at the bottom. The materials need to be chosen carefully for the overall solar cell to get the highest possible efficiency. The bandgap of the material is an important parameter to consider: with a small bandgap, more electrons can reach the excited state, but it results in lower photovoltage. Furthermore, photons of high energy will waste most of that energy as heat instead of conversion into

electrical energy. On the other hand, if the bandgap energy is too high, photons with higher energies are needed to excite the electrons into the conduction band, which reduces the output current of the device. The bandgap dimensions must be a balance between the two [2]. Additionally, the materials are chosen to be lattice matched as shown in Figure 2-3. Mismatch in the lattice induces defects or dislocations at the interface where recombination can occur, resulting in the loss of minority carriers. Such effects will decrease the efficiency of the overall solar cell [20]. The triple-junction solar cells studied in this work are fabricated using, from top to bottom, gallium indium phosphate (GaInP), indium arsenide (InAs) quantum dots in a matrix of indium gallium arsenide (InGaAs), and germanium (Ge), as shown in Figure 2-8(a). These sub-cells are connected in series by TJ connecting the *p*-terminal of one sub-cell to the *n*-terminal of the adjacent sub-cell. The theory of TJ will be elaborated in the next section. Moreover, the top layer is covered with an antireflection coating (ARC), a thin-film dielectric of refractive index higher than the one of the air and lower than the semiconductor. The ARC is designed to increase the amount of light transmitted to the cell, and minimise the reflected light [2].

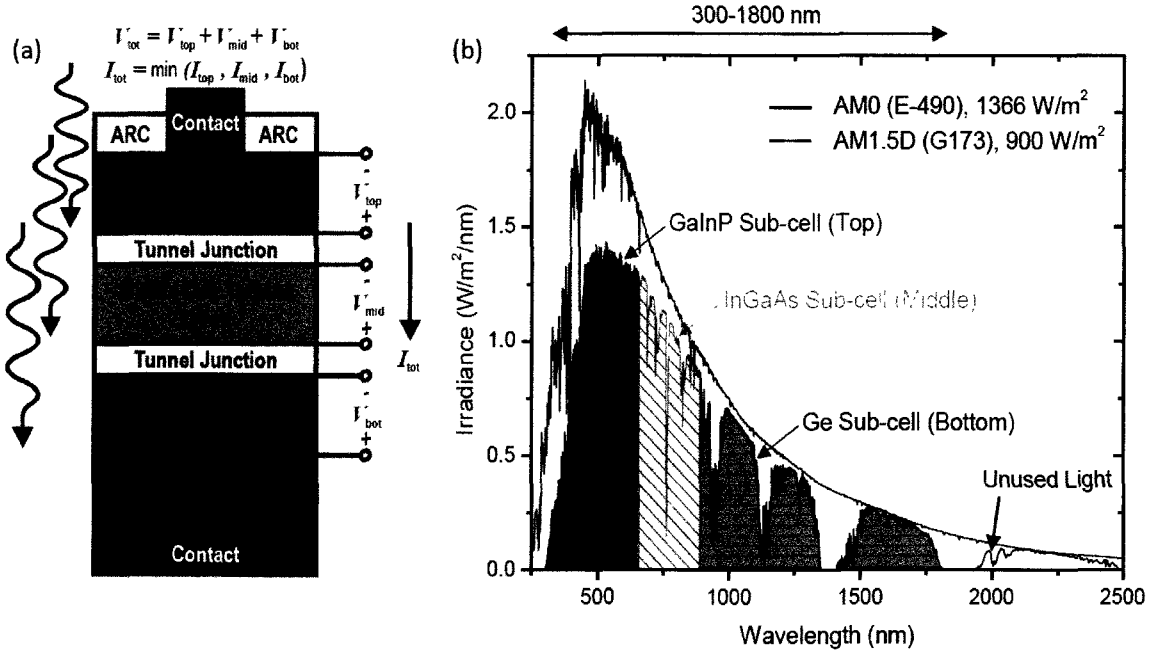

Figure 2-8: (a) Structure of a III-V triple-junction solar cell and (b) each sub-cell absorption spectrum overlaid with the AM1.5D solar spectrum. [Courtesy of Christopher E. Valdivia]

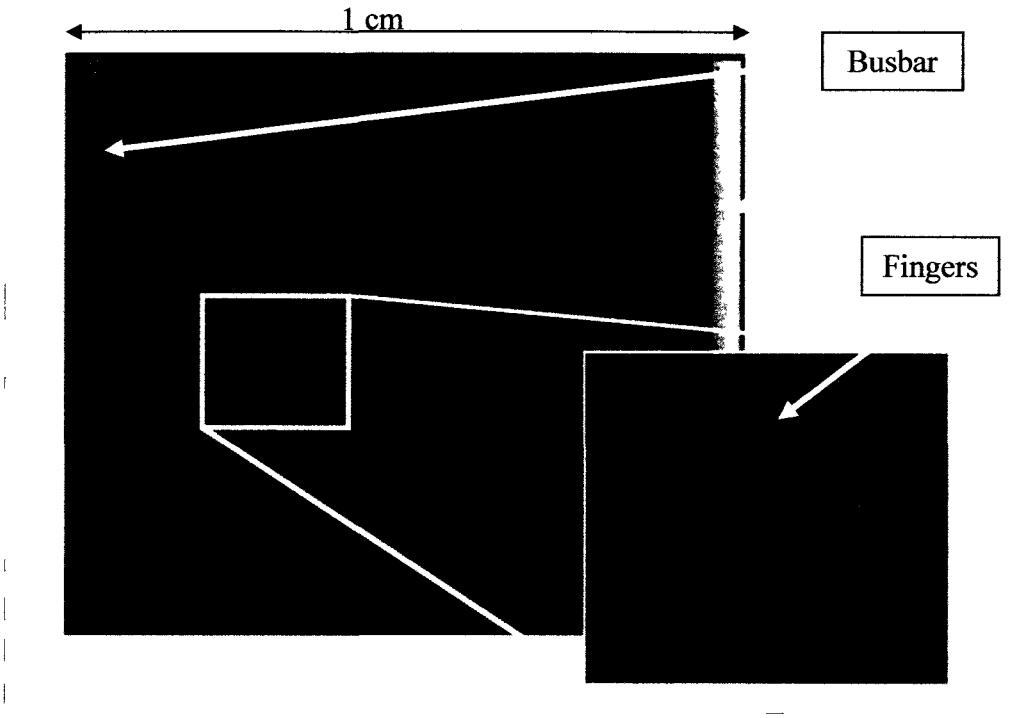

Figure 2-9: Picture of a multi-junction solar cell, with an in-set on the finger and the busbars constituting the pattern of metal contact. The brightness of the inset was increased to show the fingers.

Two electrical contacts are needed to apply a voltage on a solar cell, located on the top and on the bottom of a device. The bottom contact is formed by a metallic layer deposited on the back of the solar cell while the top contact is formed by a metallic electrode grid imprinted on the top of the solar cell. This metallic grid consists of a pattern of fingers covering the solar cell and two busbars of each side to enable a good conduction while allowing the cell to absorb as much sunlight as possible, as illustrated in Figure 2-9.

2.2-3 *J-V* characteristics

To determine the efficiency of a solar cell, current density-voltage (*J-V*) characteristics are measured by sweeping over a determined range of voltage and measuring the output current. Several important parameters can be obtained from these measurements.

The first parameter is the open circuit voltage noted V_{OC}. It is the maximum voltage of the solar cell, and occurs when the current density is zero, and the resistance is infinite. V_{OC} is given by [2]

$$V_{OC} = \frac{kT}{q} \ln\left(\frac{J_{SC}}{J_0} + 1\right). \tag{2.2.2}$$

where J_0 is a constant.

The next value is the short circuit current density noted J_{SC}. It is the current density measured when the voltage is zero and corresponds to the current density generated by the illumination only. These values are indicated in Figure 2-10. The net current density in a solar cell is given by [2]

$$J(V) = J_{SC} - J_O(e^{qV/kT} - 1), \tag{2.2.3}$$

A solar cell also generates power. The power density is given by [2]

$$P = JV. \tag{2.2.4}$$

The fill factor (*FF*) is a measure of the squareness of the *J-V* curve, corresponding to the largest rectangle that fits under the *J-V* curve. Its value is always less than one, and is given by [2]

$$FF = \frac{P_{MP}}{V_{OC} J_{SC}}, \tag{2.2.5}$$

where P_{MP} is the maximum power of the cell. The *FF* is used to measure the efficiency of the cell. The power efficiency of a solar cell, referred to as efficiency, is given by [2]

$$\eta = \frac{J_{SC} V_{OC} FF}{P_S}, \tag{2.2.6}$$

where P_S is the incident light power density. It is defined as the ratio of the maximum total power density of the solar cell to the total irradiance. It depends on the spectrum and

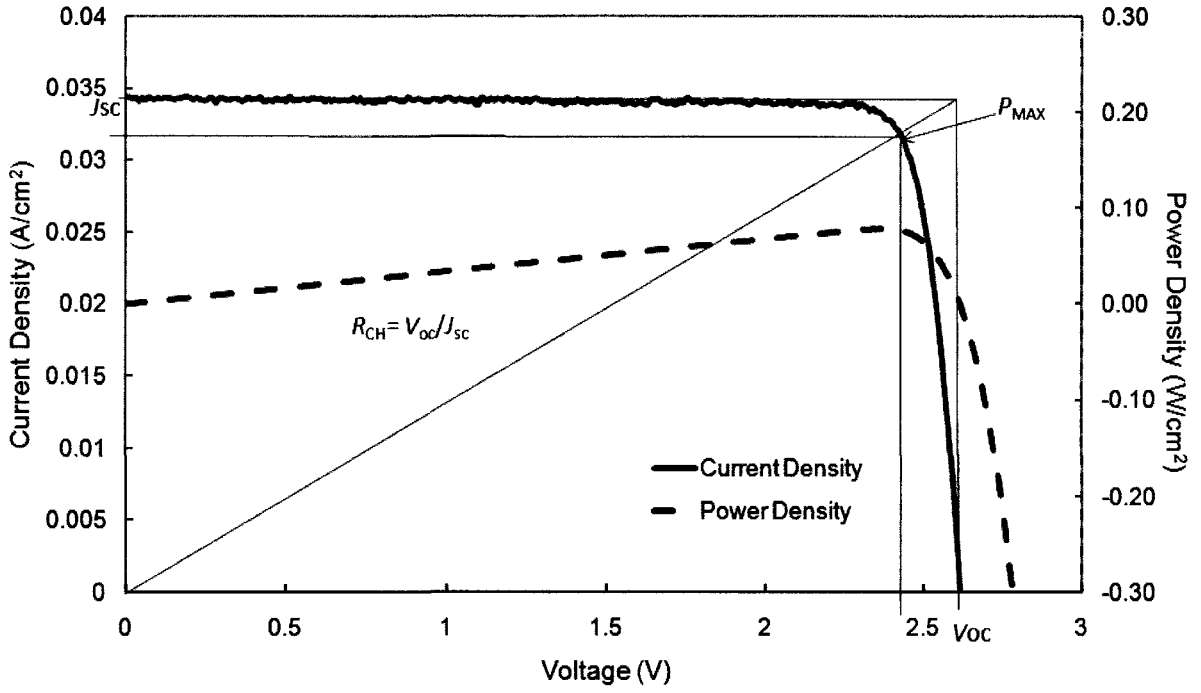

Figure 2-10: *J-V* (full line) and *P-V* (dashed line) characteristics of a solar cell. The power density is displayed by the right *y*-axis while the current density is displayed by the left *y*-axis.

intensity of the incident sunlight, as well as the temperature [38]. Typical *J-V* and *P-V* curves are illustrated in Figure 2-10.

The efficiency of a solar cell is decreased by several parameters, the most important one being resistive losses. There are different types of resistances, the characteristic resistance and the parasitic resistance, each of them influencing the *J-V* curve in a different way, as depicted schematically in Figure 2-11. The characteristic resistance of a solar cell is its resistance at the maximum power point. It is given by

$$R_{CH} = \frac{V_{OC}}{J_{SC}}. \tag{2.2.7}$$

The parasitic resistance is due to the fabrication of a device. It arises from series resistance and parallel resistance. The series resistance (R_S) is the resistance due to the

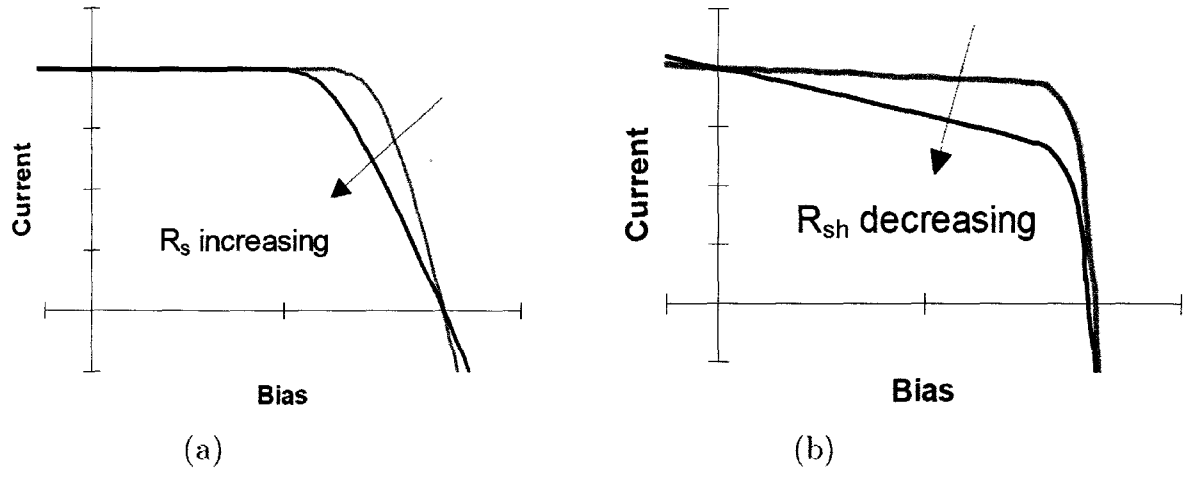

Figure 2-11 : Effects of parasitic resistance on the *I-V* curve when (a) increasing series resistance and (b) reducing shunt resistance; from Ref. [2] p. 14.

material of the cell. It can reduce the J_{SC} as well as the *FF*, but it mainly affects the slope of the *J-V* curve near V_{OC}, as shown in Figure 2-11(a).

The parallel resistance, also called shunt resistance (R_{SH}) comes from leakage current around the sides of the device. It is mainly due to fabrication defects in the cell. R_{SH} reduces the slope near the V_{OC}, but has no effect on the J_{SC} of the cell. Therefore, it affects the slope of the *J-V* curve near J_{SC}, as illustrated in Figure 2-11(b). Its effects are observable at low voltage and low illumination.

The *J-V* curve is sensitive to external parameters, such as the temperature and the intensity of the light. In previous studies [39], it has been observed that temperature has a significant effect on solar cell efficiency. Increasing the temperature of a semiconductor reduces the bandgap, enabling electrons with lower energy to go through. The dark current increases as there are more vibrations (i.e. phonons) present in the device. An increase in temperature decreases the V_{OC} and increases slightly J_{SC} as shown in Figure 2-12. These results are in agreement with Eq. (2.2.2) and (2.2.3). The irradiance of the light incident on the solar cell, or concentration, influences all the parameters, including the J_{SC}, the V_{OC}, the

efficiency, the *FF* and P_{MAX}. When the intensity of the light is increased, the J_{SC} increases as well, following the relation [2]

$$J(V,X) = XJ_{SC} - J_O(e^{qV/mkT} - 1), \tag{2.2.8}$$

where X is the concentration in suns and m is a diode ideality factor, or measure of how closely the diode follows the ideal diode equation. Furthermore, the V_{OC} slightly increases as shown in Figure 2-13 according to the equation [2]

$$V_{OC}(X) = \frac{mkT}{q}\ln\left(\frac{XJ_{SC}}{J_0}+1\right) \approx V_{OC}(1) + \frac{mkT}{q}\ln(X). \tag{2.2.9}$$

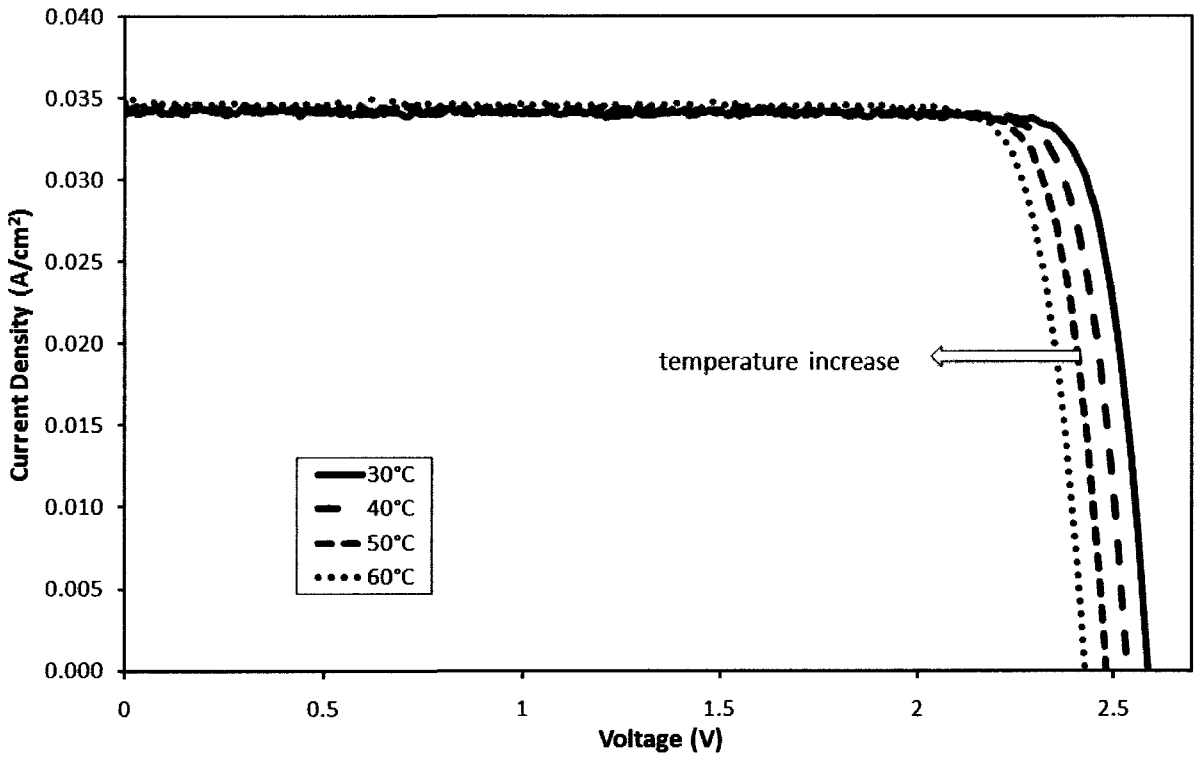

Figure 2-12: *J-V* curve of a solar cell at different temperatures varying from 30 to 60°C. Data taken using an ORIEL model 92191 solar simulator at 3 suns.

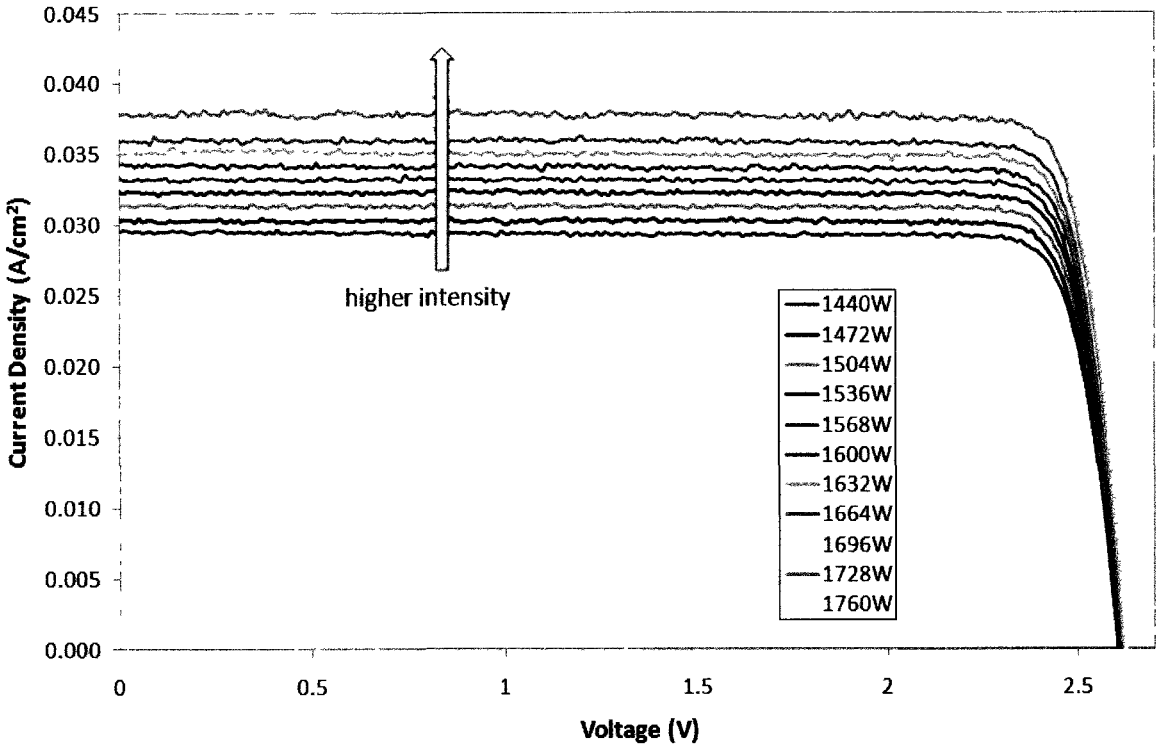

Figure 2-13: *J-V* curve of a solar cell at different lamp powers between 1440 and 1760 W. Data taken using an ORIEL model 92191 solar simulator at 25°C.

2.3 Tunnel Junction Theory

2.3-1 Structure and Operation

One of the biggest challenges in the design of MJ solar cell is the conduction of the current between the sub-cells. To address it, tunnel junctions connecting the *n* terminal of one sub-cell to the *p* terminal of an adjacent one are introduced, as shown in Figure 2-14(a). The TJ is a critical layer to conduct the current in a MJ solar cell. As illustrated in Figure 2-14(b), it consists of a heavily doped *p-n* junction with doping concentration typically $>10^{19}cm^{-3}$. As a result of this high doping density, the Fermi level is located within the allowed bands, within the conduction and the valence band of the *p*-side and the *n*-side respectively. Furthermore, the impurity states broaden into bands, and the intrinsic bandgap is reduced. This bandgap reduction is also known as band-edge tailing [26]. Moreover, because of the high doping, the width of the depletion region is narrowed, allowing carriers to tunnel through the barrier.

To provide high conversion efficiency to the overall solar cell, a TJ must fulfill some specific requirements. First, it must have a low resistance for the carriers to travel from one

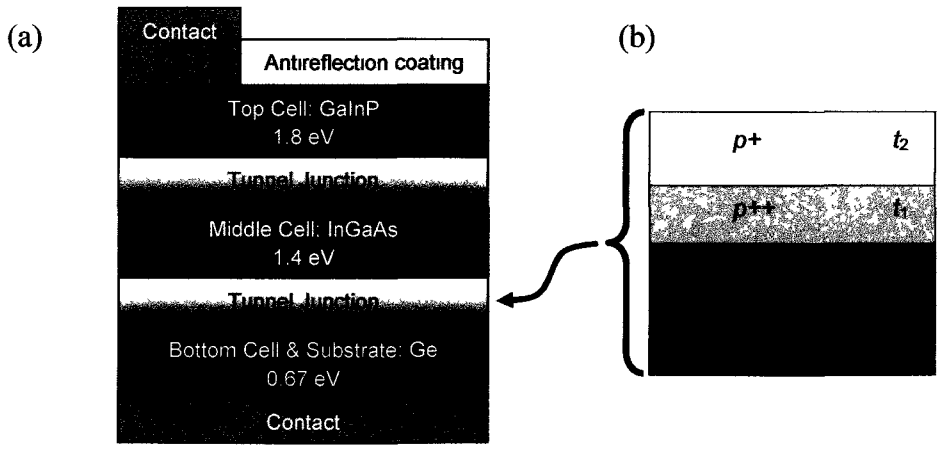

Figure 2-14: (a) Triple-junction solar cell made of InGaP/InGaAs/Ge (the energy values indicate the material bandgaps) and (b) expanded view of an AlGaAs/AlGaAs single tunnel junction (t_1 and t_2 represent the thicknesses of each layer).

sub-cell to the adjacent one, resulting in a minimal voltage drop. Second, a TJ must be transparent to the wavelengths absorbed in the surrounding sub-cells. This way, the TJ will not absorb a portion of the incident light, which would reduce the efficiency of the solar cell. This can be ensured by choosing a TJ with the largest possible bandgap. Third, it must conduct current densities higher than the operation point of a solar cell (~7 A/cm^2 at 500 suns), which can be verified by studying the *J-V* characteristic [40, 41]. The next section will describe the basic theory and the *J-V* characteristic of a TJ.

2.3-2 Tunneling mechanism

2.3-2.1 Basic theory

Tunnel junctions are diodes in which the electrons have to overcome a high energy barrier by quantum tunneling [13]. Tunneling is a quantum mechanical process in which an electron confronting a potential barrier of higher energy has a finite probability of going from the conduction band to the valence band through this barrier if the barrier is thin enough. The tunneling probability is described by the Wentzel-Kramers-Brillouin (WKB) approximation [26, 42]

$$T_t \approx \exp\left[-2\int_0^{x_2}|k(x)|\mathrm{d}x\right], \tag{2.3.1}$$

where x=0 and x_2 are classical boundaries delimiting the depletion region, as shown in Figure 2-15, and $|k(x)|$ is the absolute value of the wave vector of the carrier inside the barrier, given by

$$k(x)=\sqrt{\frac{2m^*}{\hbar^2}(PE-E_C)}, \tag{2.3.2}$$

where PE is the potential energy and m^* and E_C are previously defined variables. The potential energy of the incoming electron is equal to the bottom of the energy gap, which is

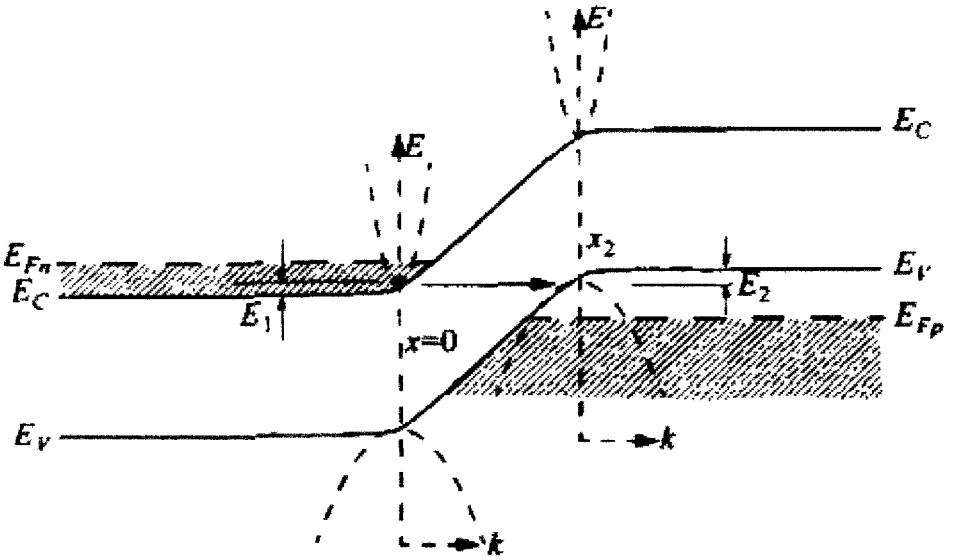

Figure 2-15: Direct tunneling process of the tunnel junction, where the *E-k* relationship on the classical turning points (x=0 and x_2) is presented; from Ref. [26] p. 422.

used as a reference to be zero, therefore the value inside the square root is negative and k is imaginary. The edge of the conduction band can be expressed in terms of the electric field $\hat{\mathbf{E}}$ and the position x, giving

$$k(x)=\sqrt{\frac{2m^*}{\hbar^2}\left(-q\hat{\mathbf{E}}x\right)}, \tag{2.3.3}$$

and replacing Eq. (2.3.2) in (2.3.1) gives

$$T_t \approx \exp\left[-2\int_0^{x_2}\sqrt{\frac{2m^*}{\hbar^2}\left(q\hat{\mathbf{E}}x\right)}\mathrm{d}x\right]. \tag{2.3.4}$$

Thus, the tunneling probability exponentially depends on the electric field and on the width of the barrier. This is why the TJ must have a thin barrier which is achieved by a high doping.

However, at thermal equilibrium the Fermi level is constant through the material, and no tunneling occurs. This can be understood using the equation of the tunneling current I_t given by [26]

$$I_t = I_{C\to V} - I_{V\to C} = C_1 \int_{E_{Cn}}^{E_{Vp}} \left[F_C(E) - F_V(E) \right] T_t N_C(E) N_V(E) \mathrm{d}E, \qquad (2.3.5)$$

where $I_{C\to V}$ is the current going from the conduction band to the valence band and $I_{V\to C}$ is the current going from the valence band to the conduction band, $F_C(E)$ and $F_V(E)$ are the Fermi energies in the conduction band and the valence band. I_t is integrated from the bottom edge of the conduction band of the *n*-side (E_{Cn}) to the top edge of the valence band of the *p*-side (E_{Vp}) [26]. Therefore, if the Fermi level is the same on both sides of the barrier, the total current is zero.

The tunneling process can be further understood by studying the energy band diagram. At thermal equilibrium, shown in Figure 2-16(a), when no bias is applied, the Fermi level is constant across the junction, and located within the conduction band on the *n*-side and the valence band on the *p*-side. There are no filled states above the Fermi level and no empty states below the Fermi level on either side of the junction. Therefore, no current can flow unless a voltage bias is applied. When a voltage bias is applied in the forward direction, from the *p*-side to the *n*-side, the band structure changes and the filled states on the *n*-side align with the empty states on the *p*-side, as illustrated in Figure 2-16(b). A band of energy is created, for which there are filled states on the *n*-side and available states on the *p*-side. Under these conditions, electrons can tunnel through the bandgap. However, for this phenomenon to occur, three conditions must be fulfilled. The filled and empty states must be at the same energy, the potential barrier height and width should be low and narrow enough to have a finite tunneling probability, and momentum is conserved [26]. The current increases until it reaches a maximum, called the tunneling peak (J_P). At the tunneling peak, the bands have reached their maximum alignment. As the voltage is increased, the bands start misaligning, causing the band of common energies to decrease, and thus a reduction of the current flow is observed, until the top edge of the *n*-type conduction band is aligned with the bottom edge of the *p*-type valence band. At this point, the current flow reaches its minimum, called the valley current density (J_V). This situation is illustrated in Figure 2-16(c). At the valley current density, the electrons can still tunnel through via interface states in the bandgap. At larger biases, the electrons gain enough energy from thermal

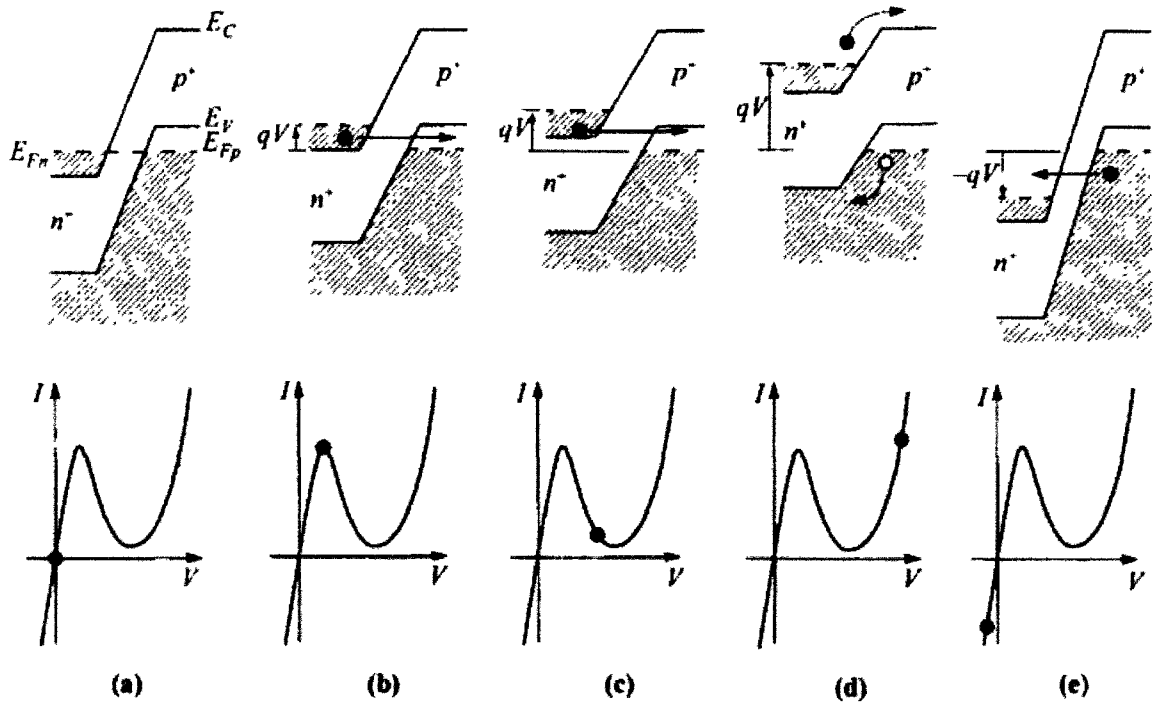

Figure 2-16: Simplified band structure diagrams of a tunnel junction: (a) at zero bias, (b) forward bias at peak tunneling current, (c) valley current, (d) thermal diffusion current and (e) in reverse bias; from Ref. [26] p. 420.

excitation to overcome the barrier, as depicted in Figure 2-16(d). This region is dominated by thermal current, where the current increases exponentially with the voltage following the typical diode behavior. Figure 2-16(e) shows the band diagram in reverse bias. In this case, the bands are shifted, creating empty states on one side of the junction. The electrons can now tunnel from the valence band to the conduction band [13].

Thus, the *J-V* characteristic can be separated in three main current regions, presented in Figure 2-17(b). The first component is the initial slope region, where the current increases to the tunneling peak. The current density and the voltage at the peak are called the peak current density J_P, and the peak voltage V_P. After the peak, the current decreases to the valley, and reaches the valley current J_V and the valley voltage V_V. The region between the peak and the valley, illustrated in Figure 2-17(a), is the NDR region. When the system is biased inside the NDR region, the measurement circuit becomes unstable, leading to inaccuracy in measuring the peak and valley currents. For $V > V_V$, the current is governed by the excess and thermal currents, where each current component varies exponentially with the voltage. The thermal

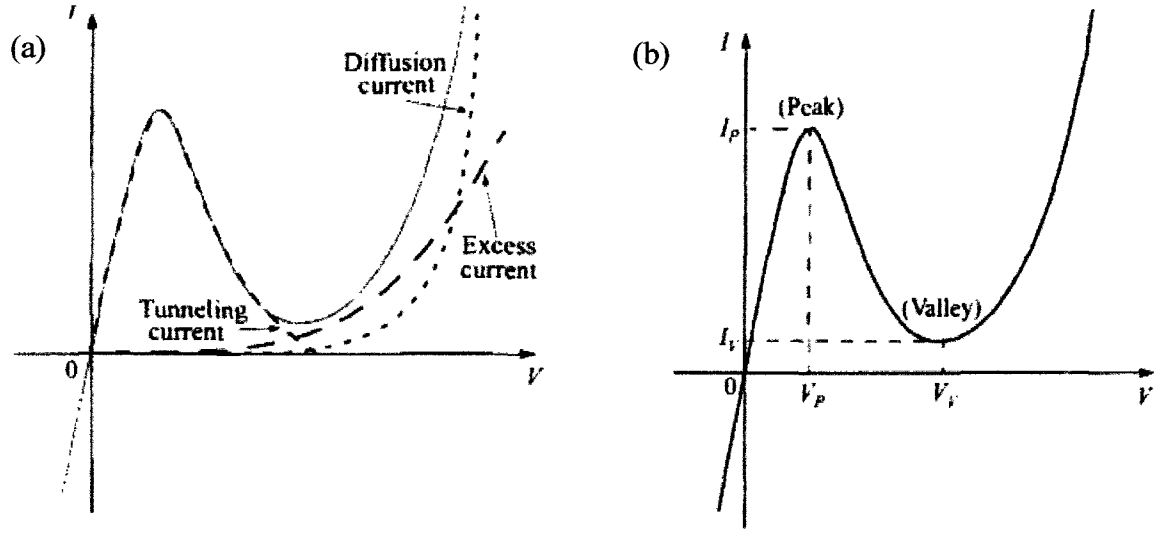

Figure 2-17: Ideal current-voltage characteristic of a tunnel junction displaying (a) the three main current components: the tunneling current, excess current and thermal diffusion current, and (b) the same *I-V* curve but instead, showing the peak tunneling current and valley current; from Ref. [26] p. 419.

current is the current of a *p-n* junction diode in forward bias, while the excess current is due to tunneling through interface states located within the bandgap [26].

The tunneling peak current must be higher than the overall operating current of the solar cell. Otherwise, the MJ solar cell would experience a large voltage drop across the TJ as the operating point moves into the excess region of the *J-V* curve. The peak tunneling obeys the following equation [30]

$$J_P \propto \exp\left(-E_g^{3/2}/\sqrt{N_{\text{eff}}}\right), \tag{2.3.6}$$

where E_g is the energy gap, N_{eff} is the effective doping concentration and is given by

$$N_{\text{eff}} = N_{\text{p++}} N_{\text{n++}} / \left(N_{\text{p++}} + N_{\text{n++}}\right), \tag{2.3.7}$$

where $N_{\text{p++}}$ and $N_{\text{n++}}$ are the doping concentrations of the *p*++ and *n*++ regions respectively [43]. According to Eq. (2.3.6), for the same effective doping concentration, a TJ made of a semiconductor with a high bandgap will have a much lower peak tunneling current density than a device fabricated in a semiconductor with a lower bandgap. Therefore, a TJ composed of AlGaAs (E_g ~ 1.8 eV) will have a peak tunneling current density approximately 50%

lower than a TJ composed of GaAs ($E_g \sim 1.4$ eV), assuming all other parameters are equal [41].

Only the initial slope region is relevant for MJ solar cells as it is used to determine the voltage drop during solar cell operation. The typical current density of a MJ solar cell is approximately 7 A/cm^2 at 500 suns. A TJ must be able to carry the same or a higher amount of current density. Without a good quality band-to-band tunneling current region, the carriers within a sub-cell will not be able to pass the high resistance thermal current region to the adjacent sub-cell. Hence, the low resistance connection between the sub-cells is formed when the band to band tunneling current region allows the carriers to bypass the thermal current region [41].

2.3-2.2 Sentaurus simulation model

A semiconductor device simulation software tool named Synopsys Sentaurus [44] was used to create a TJ model and simulate its *J-V* characteristics by solving Poisson's equation and the electron and hole current continuity equations throughout a non-local mesh defined in the ultra thin device. The TJ theory is very similar to that described above.

The expression for the tunneling probability of a carrier of energy ε from position x_0 to x_2 can be described using the WKB approximation [44]:

$$\begin{aligned} \Gamma_{CC}(x_2,x_0,\varepsilon) &= \tau_{CC}(x_0,\varepsilon)\exp\left(-2\int_{x_0}^{x_2}\kappa_C(r,\varepsilon)dr\right)\tau_{CC}(x_2,\varepsilon) \\ \Gamma_{VV}(x_2,x_0,\varepsilon) &= \tau_{VV}(x_0,\varepsilon)\exp\left(-2\int_{x_0}^{x_2}\kappa_V(r,\varepsilon)dr\right)\tau_{VV}(x_2,\varepsilon) \end{aligned}, \qquad (2.3.8)$$

where Γ_{CC} and Γ_{VV} are the probability of tunneling from the conduction band to the conduction band and from the valence band to the valence band, r is the distance and τ_{CC} and

τ_{VV} are the interface transmissions coefficients (set to one by default). This equation is equivalent to Eq.(2.3.1). κ_C and κ_V are the wave numbers at position r given by[44]

$$\begin{aligned}\kappa_C(r,\varepsilon) &= \sqrt{2m_C(r)\left|E_C(r)-\varepsilon\right|}\Theta\left[E_C(r)-\varepsilon\right]/\hbar \\ \kappa_V(r,\varepsilon) &= \sqrt{2m_V(r)\left|\varepsilon-E_V(r)\right|}\Theta\left[\varepsilon-E_V(r)\right]/\hbar\end{aligned}, \tag{2.3.9}$$

where m_C and m_V are the conduction and valence band tunneling masses respectively, E_C and E_V are the conduction and the valence bands energies and Θ is the unit step function (0 for negative arguments, 1 for positive arguments).

Both wave vectors can be integrated into a single expression, giving [44]

$$\kappa = \frac{\kappa_C\kappa_V}{\sqrt{\kappa_C^2+\kappa_V^2}}, \tag{2.3.10}$$

The simulated energy band diagram of a TJ is shown in Figure 2-18, where the potential barrier is highlighted, corresponding to the depletion region.

The conduction band to valence band tunneling current density (J_{CV}) can be calculated by integrating the net recombination rate over the tunneling length of the junction and over all particle energies [44]

$$J_{CV}(x_0) = -q\int_{x_0}^{\infty}\int_{-\infty}^{\infty}\left[R_{CV}(r,x_0,\varepsilon)-G_{CV}(r,x_0,\varepsilon)\right]d\varepsilon dr, \tag{2.3.11}$$

where $R_{CV}(x_2,x_0,\varepsilon)$ and $G_{CV}(x_2,x_0,\varepsilon)$ are the recombination and the generation rates at positions x_2 and energy ε due to tunneling at x_0 given by[44]

$$\begin{aligned}R_{CV}(x_2,x_0,\varepsilon)-G_{CV}(x_2,x_0,\varepsilon) = \frac{A_{CV}}{2qk}\vartheta\left[\varepsilon-E_V(x_2),\frac{dE_V(x_2)}{dx_2}\right]\vartheta\left[\varepsilon-E_C(x_0),\frac{dE_C(x_0)}{dx_0}\right] \\ \Gamma_{CV}(x_2,x_0,\varepsilon)\times\left[T_P(x_2)+T_n(x_0)\right] \\ \left[\left(1+\exp\left[\frac{\varepsilon-E_{F,p}(x_2)}{kT_P(x_2)}\right]\right)^{-1}-\left(1+\exp\left[\frac{\varepsilon-E_{F,n}(x_0)}{kT_n(x_0)}\right]\right)^{-1}\right]\end{aligned} \tag{2.3.12}$$

where Γ_{CV} is the band-to-band tunneling probability, E_{Fn} and E_{Fp} are the quasi-Fermi energies of electrons and holes respectively, T_p and T_n are the temperature of electrons and hole, which are assumed to be the equal to the lattice temperature T=300K, A_{CV} is the effective Richardson constant [44]

$$A_{CV} = \sqrt{g_C g_V} A_0 \tag{2.3.13}$$

where g_C and g_V are fit parameters for the conduction and the valence bands respectively and A_0 is the Richardson constant for free electrons. $\vartheta(x,y)$ is a function corresponding to

$$\vartheta(x,y) = \delta(x)|y|\Theta(y), \tag{2.3.14}$$

where δ is the delta function and Θ is once again the unit step function as defined earlier. This function dictates the requirement for constant energy transition between the conduction to valence band tunneling, such that the energy difference between the carrier and the valence band energy at point x_2 is the same as the energy difference between the carrier and the conduction band energy at point x_0. Furthermore, the unit step function dictates that derivative of the conduction and valence band energies at x_2 and x_0 must be positive.

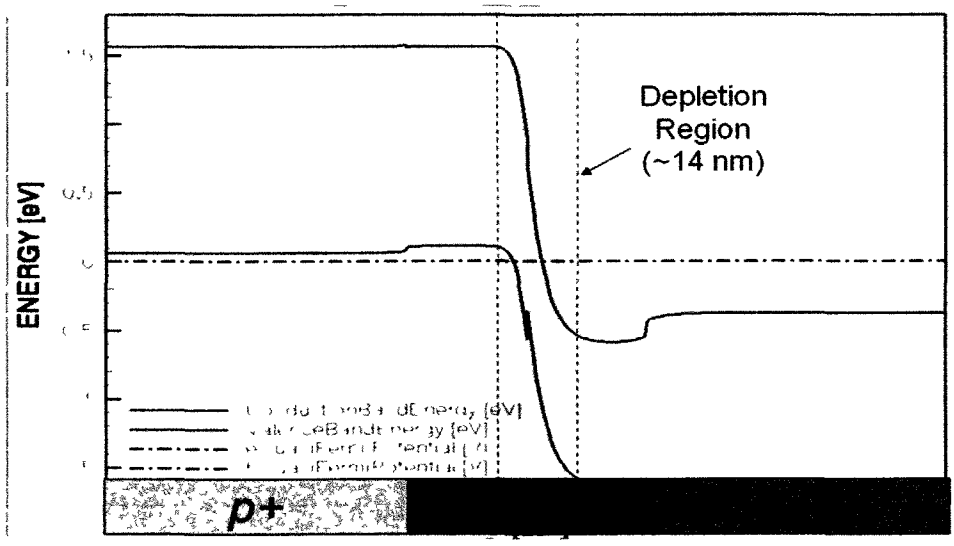

Figure 2-18: Energy band diagram of an AlGaAs/AlGaAs TJ at 0 V bias. The plot comes from results simulated using Synopsys Sentaurus [45].

2.3-3 Effects of resistance and temperature on the *J-V* characteristics.

The internal resistance of a device has a direct impact on the shape of the *J-V* curve. These effects can be observed by a change in the initial slope region. The total resistance of a TJ is given by the inverse of the slope near the origin, thus if the total resistance is high, the value of the slope will be high. Moreover, the resistance has an effect on the NDR region of the *J-V* curve. If the resistance is higher, the NDR region is narrower, and inversely if the resistance is lower, the NDR region is wider [16]. This resistance is composed of the TJ device plus the resistance inherent to the mesa structure. A mesa structure consists of a top contact and a bottom contact deposited on a TJ to allow characterisation, which will be described in more detail later. The mesa structure resistance includes resistances in the cap layers and lateral perimeter resistance, or sheet resistance, and metal-semiconductor contacts, or contact resistances. While the contact resistance corresponds to the current loss inside the metal contacts, the sheet resistance is the internal resistance of a thin layer of material. This quantity is measured in ohms per square (Ω/□). This means the sheet resistance is the same for two squares of any dimension of the same material [46]. These internal resistances can be determined using two methods detailed in the next section, the transmission line measurements (TLM) method and the Corbinos measurements.

As mentioned in section 2.2-3, temperature has a significant effect on solar cell efficiency. The effect of temperature on a TJ can be analysed. When the temperature increases, the number of electrons in the valence band increases, according to the Fermi-Dirac distribution given by Eq.(2.1.6). Therefore, more current travels and the resistance is decreased. When the temperature increases, there is also more scattering of the electrons, which causes the resistance to increase. The result of both effects causes the resistance to decrease when the temperature increases [45]. According to the literature [47-48] the *J-V* curve of tunnel junction should vary in the thermal current region, but the initial slope should stay almost the same while the tunneling peak current density is expected to increase with temperature.

2.3-4 Transmission line measurements

2.3-4.1 Transmission line measurements method

The TLM method is used to determine the sheet resistance and the contact resistance of a material [49]. TLM pads, illustrated in Figure 2-19 consist in a series of metal pads deposited on a semiconductor layer and separated from one another by a distance *d*. When a voltage is applied between two pads and a current-voltage (*I-V*) curve is measured, the current loss is due to the internal resistance of the device. Ideally, the *I-V* curve follows a linear behavior, and the total resistance can be extracted from the slope using Ohm's law

$$V = RI\,. \tag{2.3.15}$$

These measurements are done for a series of pads separated by different distances. The variation of the total resistance with the spacing is then plotted. Figure 2-20 shows an example of a graph of total resistance as a function of spacing *d*. The plot obtained shows a linear relation between the total resistance and the spacing between the pads, which is given by [50]

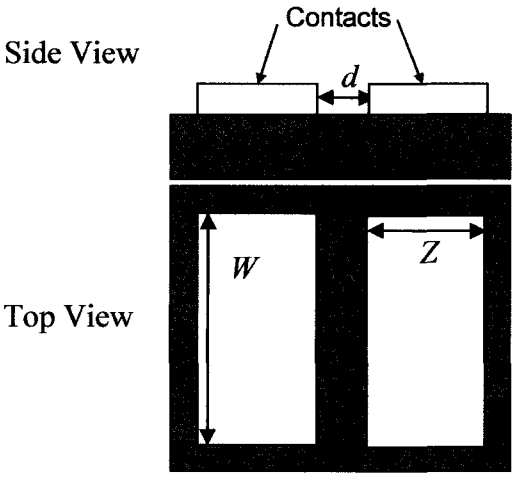

Figure 2-19: Schematic of TLM pads of dimension *W*×*Z* on which the metal contacts are deposited on the semiconductor layer and separated by a distance *d*.

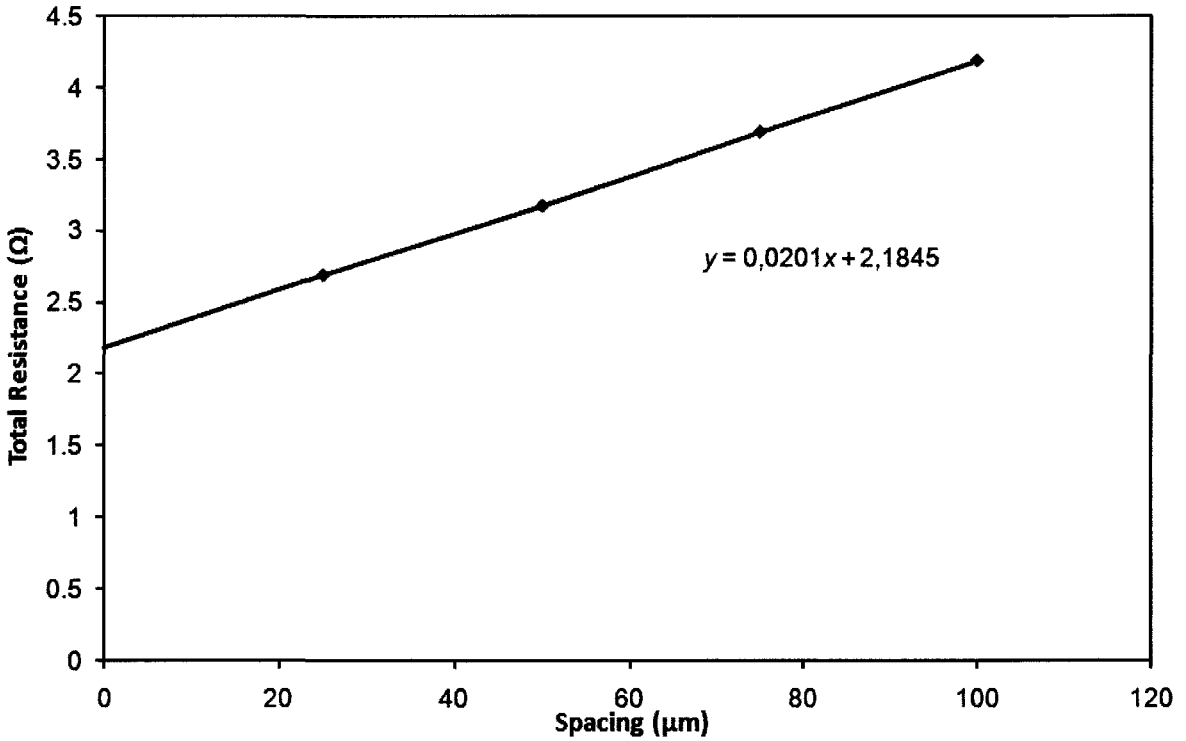

Figure 2-20: Example graph of the total resistance as a function of the spacing between TLM pads.

$$R_T = \frac{R_S d}{W} + 2R_C, \tag{2.3.16}$$

where R_S is the sheet resistance of the semiconductor layer, R_C is the resistance of the metal contact, d is the spacing between two adjacent pads, and W is the width of the pads. From Eq. (2.3.16), the sheet resistance can be extracted from the slope while the contact resistance is given be the y-intercept [50-52]. The resistance of the edges is neglected. The sheet resistance is used to calculate the resistivity of a material using the following relation:

$$R_S = \frac{\rho}{t}, \tag{2.3.17}$$

where ρ is the resistivity and t is the thickness of the layer. The resistance of the layer of material can be calculated as it is a function of the resistivity of the material and the dimensions of the layer of material through which the current passes, given by

$$R = \frac{\rho Z}{Wt}, \tag{2.3.18}$$

where Z and W are the dimensions of the layer. In the case of a square, Z=W.
Using the value of the resistance, the specific resistivity can be calculated. The specific resistivity is given by slope of a *V-J* curve. It is used to compare the resistance of samples of different dimensions. In the case of TJ, the resistance is highly dependent on the dimensions of the samples. It is a way of calculating a resistance independent of the surface [53-55]. The specific resistivity is given by

$$R' = R \cdot Area. \tag{2.3.19}$$

The units of the specific resistivity are $\Omega \cdot cm^2$.

2.3-4.2 Corbino method

Another method widely used to determine the internal resistance of a semiconductor device is the Corbino method, also called circular transmission line measurements (CTLM) method [53]. Corbinos are similar to TLM pads but they use a cylindrical geometry. As shown in Figure 2-21, they consist in a series of concentric discs deposited on a layer of semiconductor separated by a distance *s*. They avoid current spreading as well as edge current both of which can seriously affect the results. They are therefore more accurate than TLM pads [54-56].

The *I-V* curves are measured by applying a voltage between the inner and the outer metal contacts, for different gap spacing *s*. Similarly to the TLM method, the *I-V* characteristics are linear, enabling us to extract the total resistance using Ohm's law (Eq. (2.3.15)). Plotting the resistance as a function of *s* gives a nonlinear relation that can be transformed into a linear relation using the correction factor given by [55]

$$c = \frac{r_1}{s} \ln\left(\frac{r_1 + s}{r_1}\right), \tag{2.3.20}$$

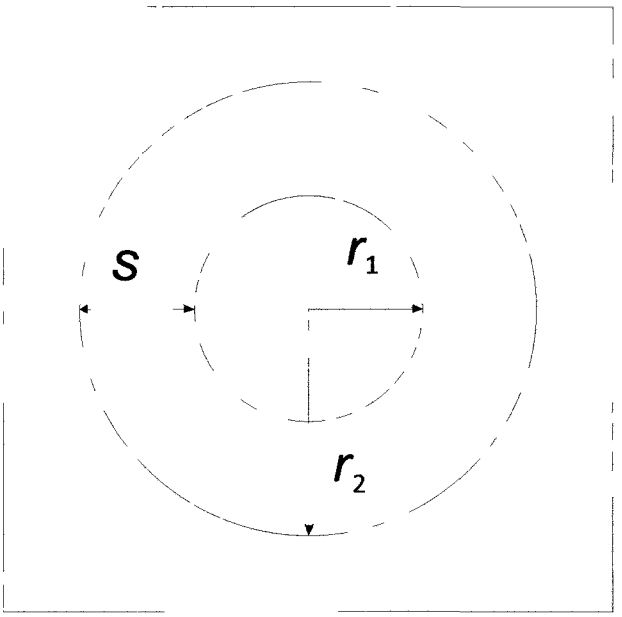

Figure 2-21: Schematic of a Corbino structure, where r_1 is the inner radius, r_2 is the outer radius and s is the spacing between the contacts; the metal contact is deposited on the semiconductor layer.

where s is the spacing between the contacts, and r_1 is the inner radius, as shown in Figure 2-21. The derivation of the correction factor is developped in Appendix A.

A typical graph of the total resistance of a Corbino as a function of the spacing is shown in Figure 2-22. The corrected values give a linear curve, and its equation is given by [54]

$$R_T = \frac{R_s s}{W_C} + 2R_C, \tag{2.3.21}$$

where R_S is the sheet resistance, R_C is the contact resistance and W_C is the area of the inner disc, given by $W_C = 2\pi r_1$. Thus R_C is given by the y-intercept while R_S is given by the slope.

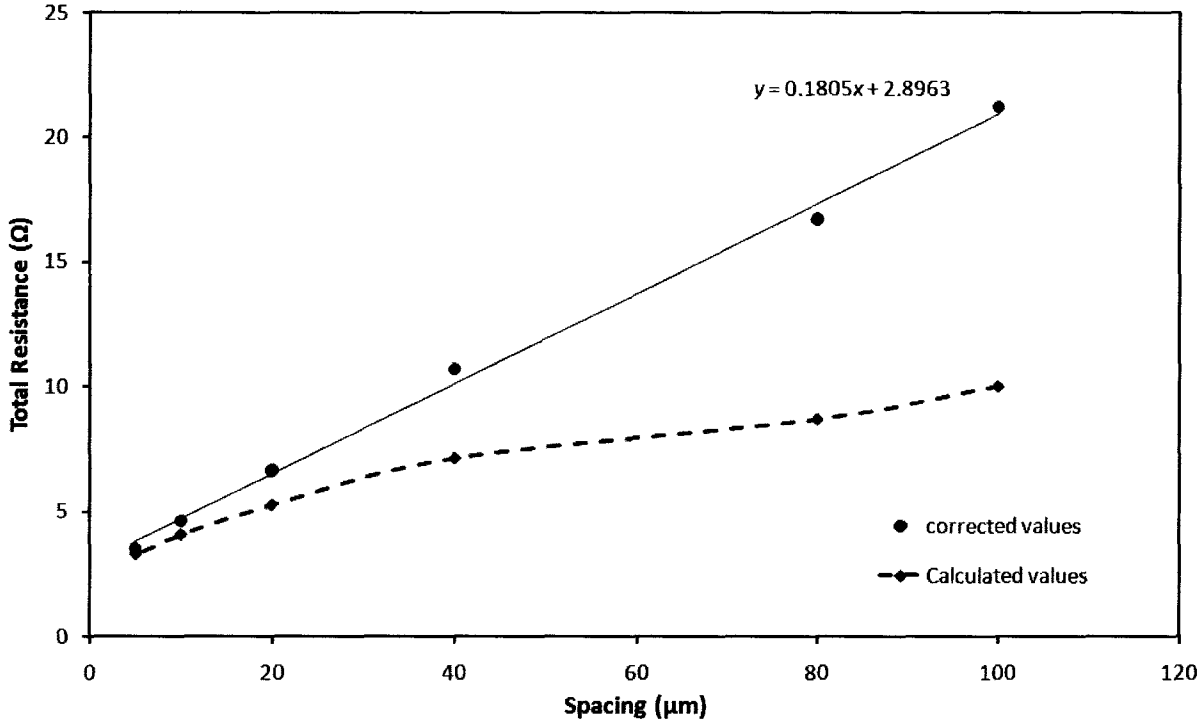

Figure 2-22: Total resistance as a function of the gap spacing between the inner and the outer metal contact of Corbinos before (black dashed line) and after (full red line) applying the correction factor for sample TJ1-B.

2.4 Band Structure of a Multi-Junction Solar Cell

As mentioned previously, a MJ solar cell consists of three *p-n* junctions connected in series via tunnel junctions. When a *p-n* junction is illuminated, electron-hole pairs are created inside the depletion region. In the energy band diagram, an electron created at a *p-n* junction rolls down the slope towards the *n*-side, while the hole goes to the *p*-side, until they reach the energy barrier of the nearest TJ. At the next *p-n* junction, another electron-hole pair is formed and the electron drifts in the potential gradient towards the energy barrier of the first TJ. Because of the hole created in the first *p-n* junction, there is now an available state for the electron to fill on the other side of the TJ. Given a narrow enough barrier, the electron will tunnel through, filling the empty state created by the hole and hence flowing to the next section of the device. The same process occurs for each *p-n* junction across each TJ.

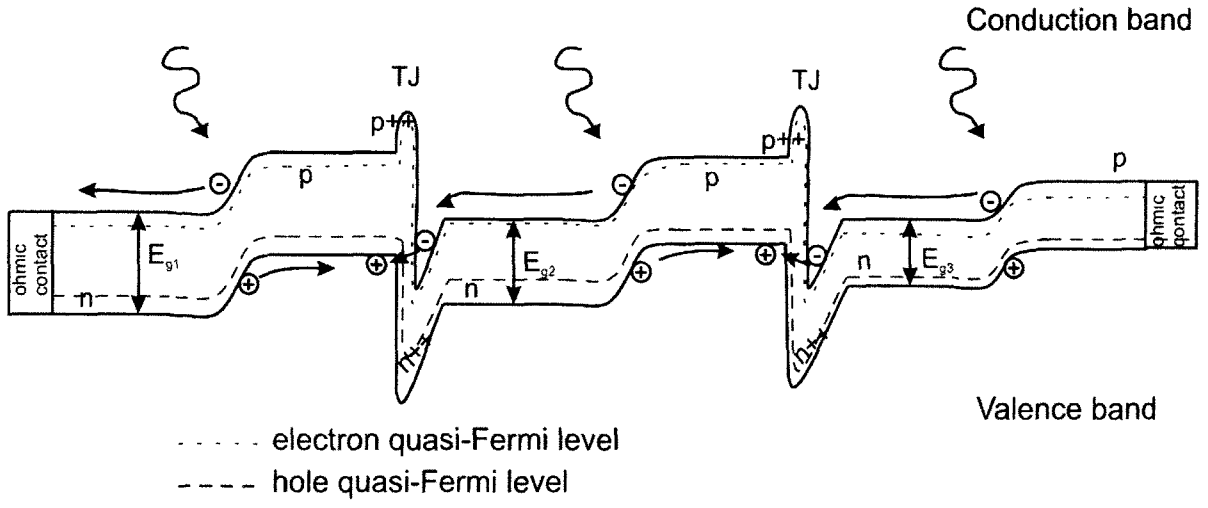

Figure 2-23: Energy band diagram of a multi-junction solar cell at 0 V bias under short-circuit conditions.

Assuming perfectly ohmic contacts, current will flow through the solar cell and every electron in the last junction will be collected. This phenomenon, illustrated in Figure 2-23 presents the energy band diagram in short-circuit current conditions. In most cases, ohmic metal-semiconductor contacts are used because they have low resistance and thus minimize the current loss. An ohmic contact is created by heavily doping a semiconductor, narrowing the width of the depletion region, which allows carriers to tunnel through the barrier. The work function of an ohmic contact is lower than the work function of the last junction, enabling current flow [2, 33, 57].

The output current of the MJ solar cell is limited by the smallest of the currents produced by any of the sub-cells. In this work, the current is limited by the middle sub-cell. If three photons are absorbed, three electron-hole pairs are created and the current can flow across the solar cell, but if only two photons are absorbed, i.e. one in the lower sub-cell and one in the higher sub-cell, there are no electron-hole pair created in the middle sub-cell. Therefore, there is no available state to be filled in the middle *p-n* junction, and the electron will not be able to tunnel through the second TJ. As a consequence, no current will flow. Hence, if one sub-cell has fewer holes created than the others, there is one less available state

to be filled by an electron, and the excess electron will be lost. At equilibrium, the electron and hole quasi-Fermi levels are equal and constant across the entire device. Therefore, no current flows when no bias is applied. At short circuit current, carriers are redistributed across the device due to the absorption of photons, resulting in a separation of the quasi-Fermi levels for electrons and holes. Current is created because of the sunlight illumination. At open circuit voltage, the slopes of the quasi-Fermi levels are negligible and any gradient on the quasi-Fermi levels in one sub-cell is cancelled out later in another sub-cell. Thus no current flows [58].

Chapter 3 – Tunnel Junction Measurements

In this section, TJ devices are studied. Two sets of samples of AlGaAs/AlGaAs TJ are measured, the first ones with a high contact resistance, the second ones with a low contact resistance. The mesa structure resistance of the devices is calculated using TLM and Corbinos measurements. A comparison between the two methods is presented to determine which is the most precise. A time-dependent analysis of an AlGaAs/AlGaAs TJ is performed to extract more precise values for the tunneling peak and valley currents. Next, the impact of the temperature on the *J-V* characteristics is studied by measuring the TJ samples over temperature. Finally, the performance of TJ fabricated in the InGaP/AlGaAs material system is presented.

3.1 Experimental Setup

The experimental setup is presented in Figure 3-1(a). The measurements are done using the four-wire remote sensing measurement technique, under dark, temperature controlled, conditions. The voltage is applied across the device using 0.0127 cm diameter tungsten tip probes held by probe holders. The samples are positioned on the gold plate as shown in Figure 3-1(b), and held by a vacuum suction as shown in Figure 3-1(c). As illustrated in Figure 3-1(c), a thermo-electric cooler (TEC) positioned between the aluminum plate and the gold plate and a resistance temperature detector (RTD) inserted inside the gold plate are used to control the temperature. The RTD is made of platinum which has a resistance sensitive to temperature. By measuring the variation in the resistance, the temperature can be inferred. The TEC uses electrical energy to transfers heat from one side of the device to the other side against the temperature gradient. It cools down the system by transferring heat from the gold plate to the aluminum plate. Both TEC and RTD are

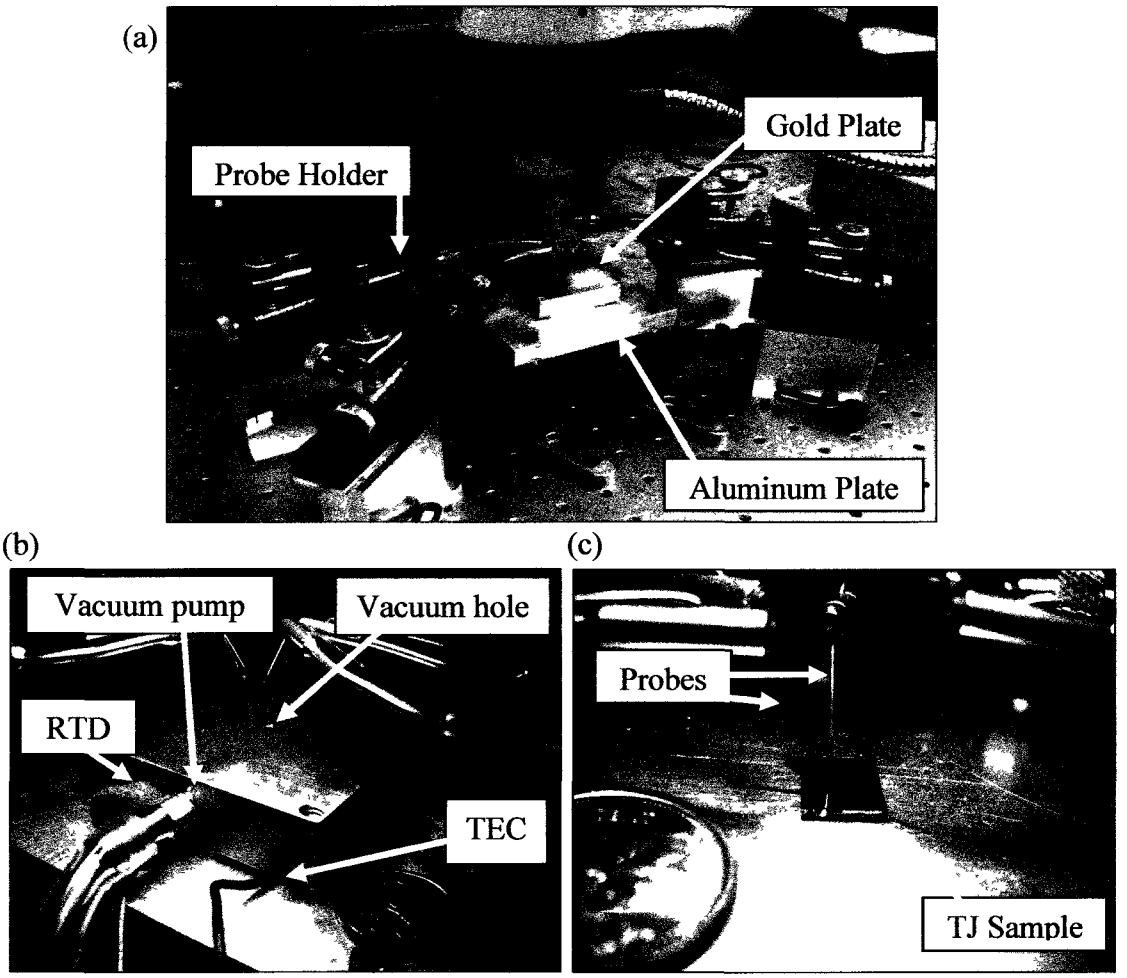

Figure 3-1: Pictures of the experimental setup presenting (a) the test stage including the probe holder, (b) a close-up of the test stage showing the vacuum pump, the RTD and the TEC and (c) a close-up of a sample in position over vacuum seal.

controlled by a Series 800 Alpha Omega Industries temperature controller. A Keithley 2601A sourcemeter is used as a power source, while the *J-V* characteristics are recorded using a LabView program. The error on the Keithley 2601A sourcemeter is ±0.3%; for more details, see Appendix B. The four-wire measurement technique is used to remove the effect of the resistance due to the experimental circuit. As shown in Figure 3-2, it consists in adding two sense connections to the usual two-wires. Ideally, no current flows through the sense wires, and thus the voltage drop is very low. The sense wires measure the voltage across the device under test (DUT), and the current going across the other connections varies to ensure the right voltage across the DUT [59].

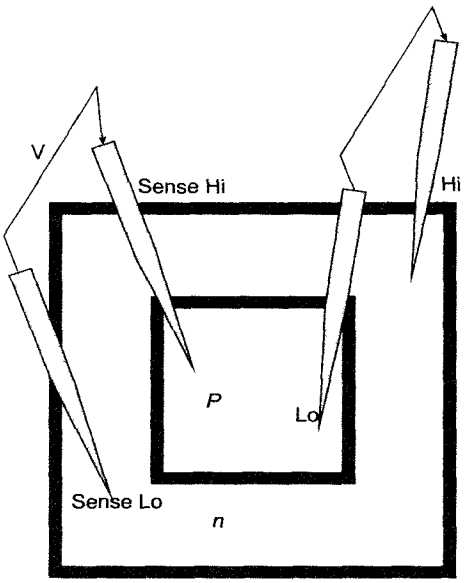

Figure 3-2: Schematic of the four-wire measurement technique.

3.2 Structure of the AlGaAs/AlGaAs and AlGaAs/InGaP TJ

In this work, two different TJ designs are studied; AlGaAs/AlGaAs and AlGaAs/InGaP, where the first compound is p++ side and the second is the n++ side (p++/n++). The n-doped GaInAs layer was lattice-matched to the Ge using 1% of In. The structure of an AlGaAs/AlGaAs TJ is depicted in Figure 3-3(a). The n-doped GaInAs layer was lattice-matched to the Ge wafer using 1% In. The AlGaAs/AlGaAs p-n junction is formed by two highly doped p++/n++ $Al_xGa_{1-x}As$ layers with a molar constant $x < 0.2$, and surrounded by two additional p+/n+ layers of $Al_xGa_{1-x}As$ with lower dopant concentration. A GaInAs encapsulating layer caps the structure. The thicknesses t_1 and t_2 are less than 50 nm while t_3 is larger than 100 nm. The TJ were grown by Metalorganic Chemical Vapour Deposition (MOCVD) on a Ge wafer and fabricated into a mesa structure for characterization, as shown schematically in Figure 3-3(b). The p++/n++ layers have an effective doping concentration of ~2.7×10^{19} cm^{-3}. The effective doping concentration N_{eff} is described by Eq.(2.3.7).

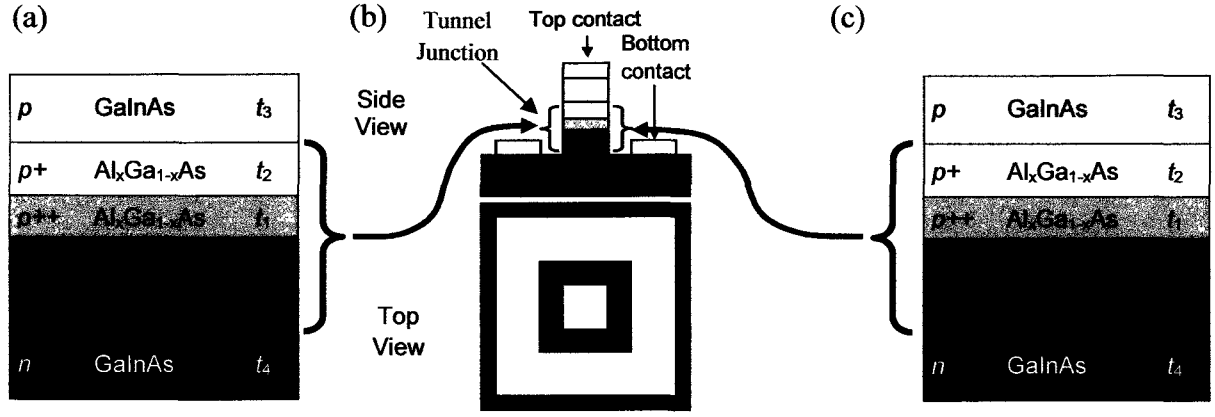

Figure 3-3: (a) Expanded view of a single AlGaAs/AlGaAs TJ, where $x < 0.2$; (b) side and top views of a single tunnel junction mesa structure; (c) expanded view of a single AlGaAs/InGaP TJ.

For the AlGaAs/InGaP TJ, shown schematically in Figure 3-3(c), the p++ layer is made of $Al_xGa_{1-x}As$ while $In_yGa_{1-y}P$ forms the n++ layer, surrounded by two buffers layers of $Al_xGa_{1-x}As$ for the p+ layer and an $In_zAl_{1-z}P$ for the n+ with lower dopant concentration, with molar constant y and z chosen to lattice-match the Ge wafer. A GaInAs encapsulating layer caps the structure. The samples were designed by Cyrium Technologies Inc., and fabricated at the Université de Sherbrooke.

Figure 3-4 shows a scanning electron microscope (SEM) image of a device having a top contact of dimension 70 μm × 70 μm, and a gap spacing of 10 μm. The outer dimensions are 200 μm × 200 μm. The TJ structures were fabricated by standard photolithography and chemical etching in a self-aligned process, using the metallic contacts as a mask for etching of the mesas that contain the TJ heterostructures. The center mesas were fabricated first by photolithography using the positive-tone resist Shipley S1813 spun on a previously deposited Microchem LOR-A lift-off resist layer. The surface of TJ structure was cleaned and deoxidized in HCl:H_2O (1:1) for 30 s prior to metallization. The metallization of the top emitter contacts was done by e-beam evaporation, followed by lift-off, and the collector contacts were fabricated in a second step of lithography. The OAI 200 mask aligner used was capable of aligning features with a precision of 2 μm. The samples were then annealed for 1

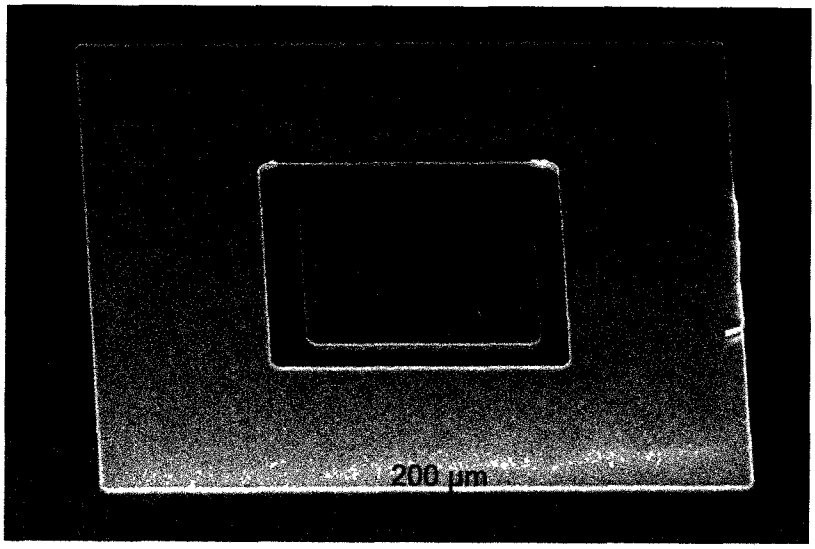

Figure 3-4: SEM image of a TJ mesa structure of top contact dimensions 70 µm × 70 µm and a gap spacing of 10 µm width.

minute at 300-350°C under N_2 atmosphere in order to diminish the specific resistance of the contacts [45].

3.3 High resistance TJ sample study

3.3-1 *J-V* measurements at 25°C

The first set of tunnel junctions, referred to as sample TJ1-A, was fabricated using Au/Ti contacts. A picture of this sample is shown in Figure 3-5. The contacts consist of 30 and 150 nm layers of Ti and Au, respectively. The metallization of the top emitter contacts with Ti (5 nm) and Au (150 nm) was done by electron beam evaporation, followed by lift-off. The mesas containing the TJ have been etched in H_3PO_4:H_2O_2:H_2O (3:1:40), using the emitter Au/Ti contacts as a mask. The collector contacts (outer ring) were fabricated by the same procedure in a second step of lithography.

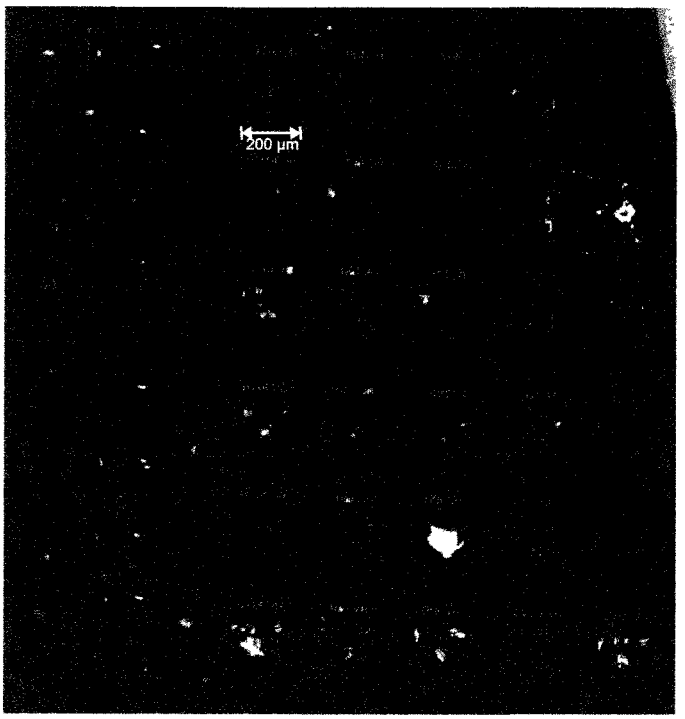

Figure 3-5: Picture displaying multiple TJ mesas from TJ1-A.

The *J-V* curve of a TJ of dimension 70 µm × 70 µm, shown in Figure 3-6, is measured at 25°C using the four-wire configuration. The three main regions described in section 2.3-2 are observed; the initial slope region goes from 0 to 0.5 V, where it reaches the tunneling peak which has a current density value of ~950 A/cm^2. Then, the current density decreased with the voltage until it reaches the valley at 0.75 V. The valley current density value is ~250A/cm^2. At 1.4 V, the current density is higher than the tunneling peak current density as the current is governed by the thermal current. The initial slope region shows a pronounced positive curvature due to high nonlinear resistance. The experimental curve is compared the Sentaurus simulation curve by adding a 9.7 Ω resistance to the simulation data. When this resistance is added to the simulation data, the simulated curve is folded over, changing the direction of the slope in the NDR region. In the Sentaurus simulation data, only the TJ is present. It can be observed that this nonlinearity is not only due to the isolated TJ, but also to a nonlinear parameter in the mesa structure of the TJ. To calibrate the simulation

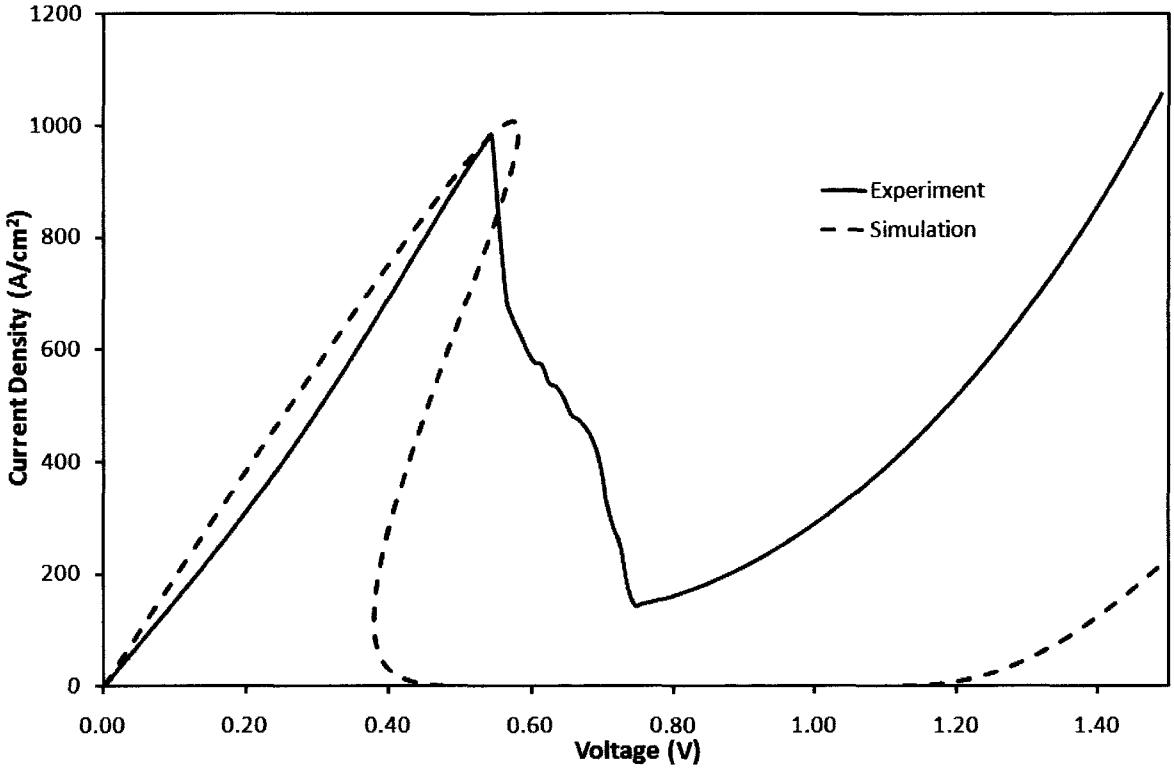

Figure 3-6: *J-V* curve at 25°C of a TJ from sample TJ1-A of top contact dimension 70 μm × 70 μm and of gap spacing 6 μm.

models, the value of the mesa structure resistance needs to be determined. The next section will present the calculations done to estimate the value of this resistance.

3.3-2 Determination of the mesa structure resistance

In a TJ device, the total resistance is given by

$$R_{TOT} = R_{NC} + R_{NTJ} + R_{PC} + R_{PTJ} + R_{TJ} + R_{NL}, \tag{3.3.1}$$

where R_{NCTJ} is the n-contact resistance, R_{PCTJ} is the p-contact resistance, R_{TJ} is the resistance of the TJ, R_{NTJ} is the resistance of the n-layer, and R_{PTJ} is the resistance of the p-layer. R_{NL} is any additional nonlinear resistance, and will be included in R_{TJ} and R_{PCTJ} in our calculations.

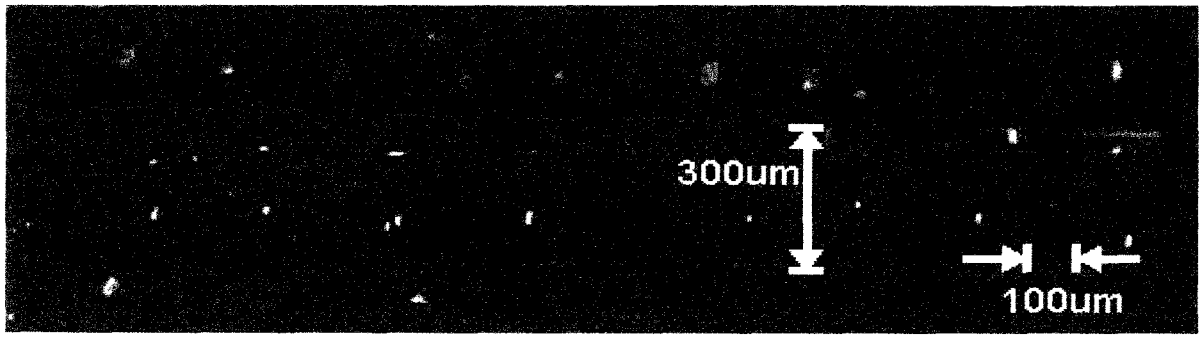

Figure 3-7: Picture of the TLM pads of sample TJ1-A; the series on the right is the *n*-type TLM pads, while the series on the left corresponds to the *p*-type TLM pads.

In this work, these resistances are referred to as internal resistances. As explained in Chapter 2, the internal resistances can be determined using TLM pads or Corbinos. The TLM pads, illustrated in Figure 3-7, are located on the TJ samples. On this sample, only the TLM method is used because the Corbinos are broken. As shown in Figure 3-7, there are two series of pads. The first one, the *n*-type pads, corresponds to the bottom contact while on the other series, referred to as *p*-type pads in the following analysis, the entire mesa structure of a TJ is etched under the *p*-contact and deposited on an *n*-doped layer of GaAs. The *n*-type pads are used to calculate R_{NC} and R_N, from which R_P can also the determined. The *p*-type pads are used to calculate R_{PC}. R_{TJ} is calculated using the simulations.

3.3-2.1 *n*-type TLM pads

In this section, the *n*-sheet resistance and the *n*-contact resistance are calculated using *n*-TLM pads. These *n*-type pads consist of a series of pads fabricated using the bottom contact of the TJ, or *n*-contact, separated by a distance *d* by the *n*-doped GaInAs layer, as shown in Figure 3-8(a). Figure 3-8 (b) presents the internal circuit of these *n*-type TLM pads. In this circuit, the total resistance is given by

$$R_{TOT} = 2R_{NC} + R_N . \tag{3.3.2}$$

The equation of the voltage is given by Ohm's law

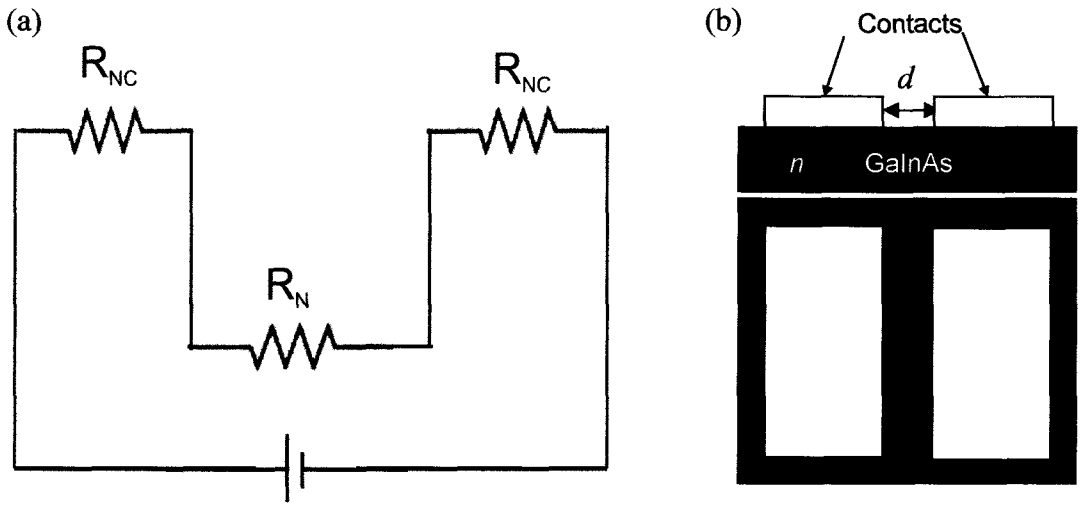

Figure 3-8: (a) Diagram presenting the structure of the *n*-type TLM pads. (b) Circuit schematic of the *n*-type TLM pads.

$$V = RI\,. \tag{3.3.3}$$

Replacing Eq. (3.3.2) in Eq. (3.3.3) gives

$$V = I\left(2R_{NC} + R_N\right). \tag{3.3.4}$$

I-V measurements are performed on these pads, showing a linear relation between the current and the voltage, as illustrated in Figure 3-9. The total resistance can be extracted using Eq. (3.3.3): the slope of the *I-V* curve corresponds to $1/R_T$, where R_T is the total resistance of the circuit. Measurements are done for different values spacing between the contacts, as shown in Figure 3-9. R_T is then plotted as a function of the spacing d, giving the linear relation described in Eq. (2.3.16), as shown in Figure 2-20.

From Eq. (2.3.16), the slope is given by

$$slope = \frac{R_{NS}}{W}, \tag{3.3.5}$$

where W is the width of the pads.

Thus the *n*-sheet resistance is calculated to be

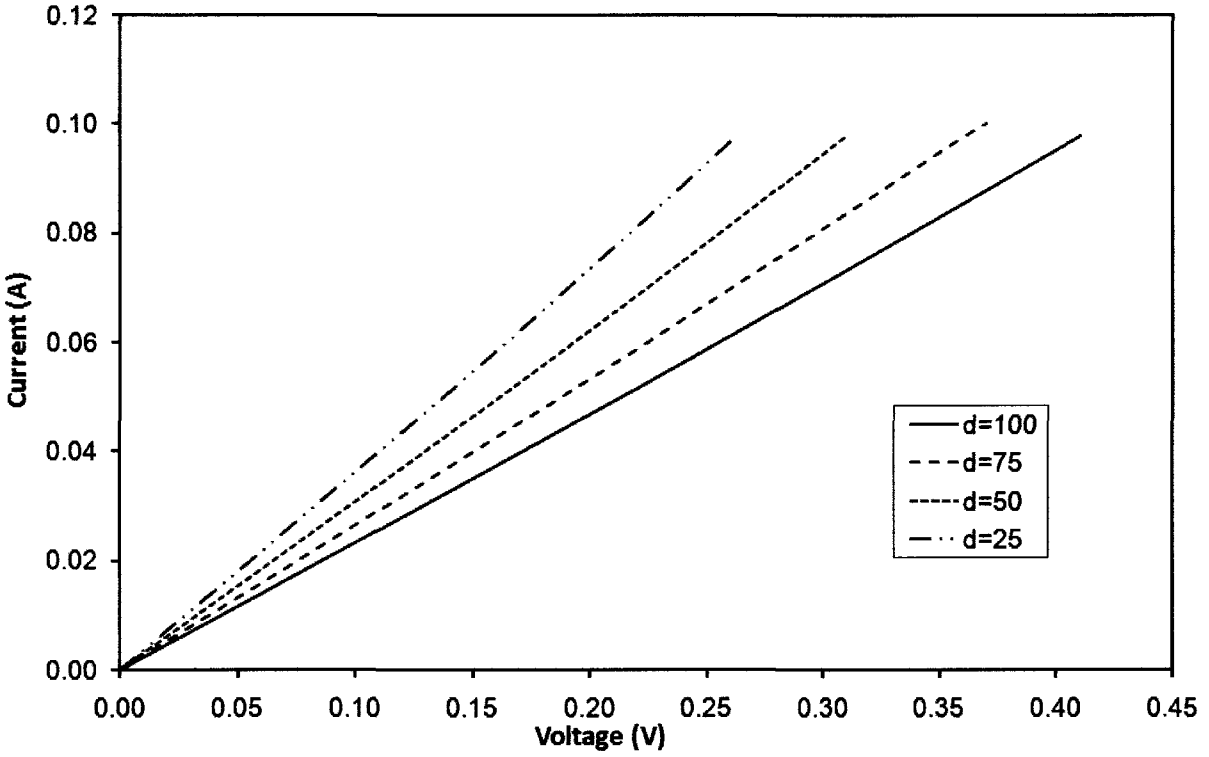

Figure 3-9: *I-V* measurements of the *n*-type TLM pads at 25°C for different spacing between the pads.

$$R_{NS} = (slope)W = \left(0.0201\times10^{4}\ \Omega/\text{cm}\right)(0.0300\ \text{cm}) = 5.1\ \Omega/\square\,. \tag{3.3.6}$$

The *n*-resistivity can be extracted using $\rho_N = (R_{NS})(n\text{-thickness}) = 3.08\times10^{-4}\ \Omega\cdot\text{cm}$.

The *y*-intercept gives

$$y(0) = 2R_{NC}\,. \tag{3.3.7}$$

Hence

$$R_{NC} = \frac{y(0)}{2}, \tag{3.3.8}$$

and the value of the *n*-contact resistance is

$$R_{NC} = 1.109\ \Omega\,. \tag{3.3.9}$$

Dividing by the area of the pads gives the value of the specific contact resistivity:

$$R'_{NC} = R_{NC}\text{Area} = 1.109\,\Omega \times 0.0150\,\text{cm} \times 0.0300\,\text{cm} = 0.5\,\text{m}\Omega\cdot\text{cm}^2. \quad (3.3.10)$$

3.3-2.2 *p*-contact resistance calculations

The purpose of this section is to determine the *p*-contact resistance R_{PC}. The *p*-contact resistance is calculated using two different methods. First, the total circuit of the TLM pads is taken into consideration. Using Ohm's law, and knowing V from the experimental measurements, the contact resistance can be extracted. V is a function of I^3, whereas R, the total resistance, is a function of I^2. The different resistances of the circuit have to be calculated. R_N, the resistance due to the *n*-layer, is determined using the *n*-type TLM pads measurements, and R_P, the resistance due to the *p*-layer, is determined using another series of TLM pads. R_{TJ}, the resistance of the tunnel junction, is calculated using the simulations and is a function of I^2. R_{PC} is the unknown, and is also defined as a function of I^2. The nonlinear contribution comes from both R_{TJ} and R_{PC}. The calculations are then done for a TJ mesa structure of dimensions 70 μm × 70 μm. The obtained results should be the same when expressed in current density. To test the validity of the results, both values obtained are used to fit the simulation data to the experiment[+].

[+] In this work, R_N and R_P are the total sheet resistances, in Ω, and R_{NS} is the sheet resistance in Ω/□. R is a resistance in Ω, and R' is the specific resistivity in $\Omega\cdot\text{cm}^2$.

Table 2: Dimensions of the TLM pads and the TJ used in the calculations

TLM-Pad Sizes	Value	Units
Small gaps (5-25 um)		
Length of the pad *(Z)*	0.0150	cm
W	0.0200	cm
Large gaps (25-100 um)		
Z	0.0150	cm
W	0.0300	cm
Mesa Structure Sizes		
Mesa length	7.00×10^{-3}	cm
Mesa width	7.00×10^{-3}	cm
Mesa area	4.90×10^{-5}	cm^2
Mesa gap	1.00×10^{-3}	cm
Total Device Width	2.00×10^{-2}	cm
Total Device Length	2.00×10^{-2}	cm
Bottom Contact Area	3.19×10^{-4}	cm^2
p-GaAs Thickness	4.00×10^{-5}	cm
n-GaAs Thickness	6.00×10^{-5}	cm

A. Calculations using the TLM pads

The TLM pads are fabricated by etching over the entire TJ mesa structure. The TJ is deposited on an *n*-doped layer of GaAs and covered by a *p*-doped layer of GaAs. The *p*-contacts are deposited on the *p*-doped layer of GaAs, as shown in Figure 3-10 (a). The circuit, shown in Figure 3-10 (b), is more complex than for the *n*-TLM pads. As the TLM

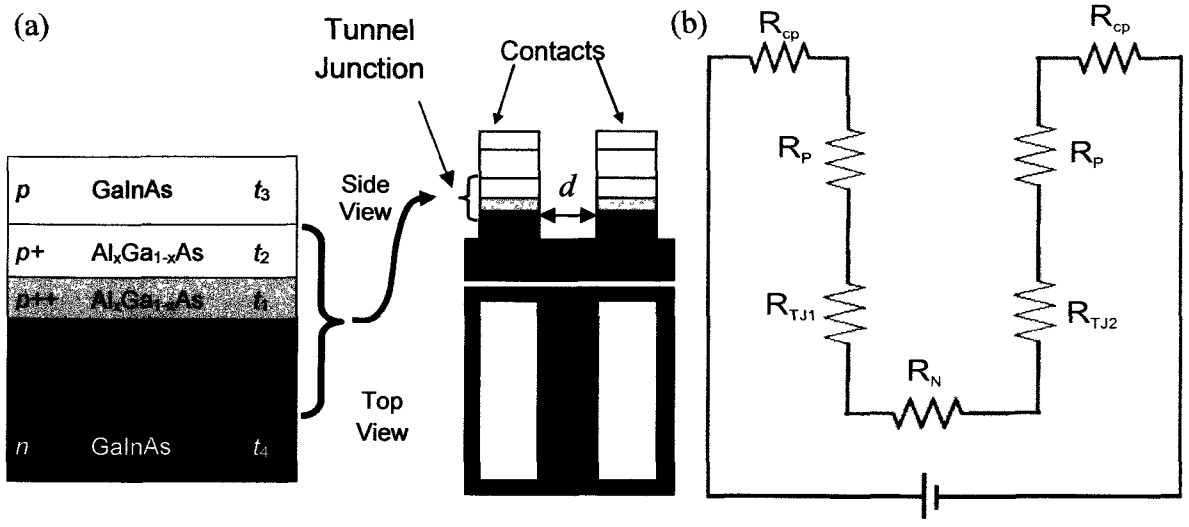

Figure 3-10: (a) Diagram presenting the structure of the *p*-type TLM pads. (b) Circuit schematic of the *p*-type TLM pads.

pads are deposited on the *n*-doped layer of GaAs only, no lateral contribution is due to the *p*-doped layer of GaAs.

The total resistance of the circuit of the *p*-type TLM pads, is

$$R_{TOT} = R_N + 2R_{PC} + R_P + 2R_{TJ}. \tag{3.3.11}$$

Replacing Eq. (3.3.11) in (3.3.3) gives

$$V = I\left(2R_{PC} + 2R_P + R_{TJ1} + R_{TJ2} + R_N\right). \tag{3.3.12}$$

The *V-I* experimental curve measured on the *p*-type TLM pads depicts a nonlinear behavior that can be fitted in x^3, giving an expression of the form $V = aI^3+bI^2+cI+d$. A fit in x^3 was chosen as the *V-I* curve is nonlinear. Higher order terms did not contribute significantly. The different resistances of the circuit have to be calculated.

- Calculation of R_N

R_N can be determined using the value of R_{NS} calculated using the *n*-TLM pads. In these pads, the current flows along *W*, and the cross section area is $A=Wt$. R_N is evaluated over the spacing ($Z=d$), and therefore changes for all the different *d*:

$$R_N = \frac{R_{NS} Z}{W} = \frac{R_{NS} d}{W}. \tag{3.3.13}$$

For d = 100 μm, R_N = 1.71 Ω. See Table 3 for the values for the different spacing. The equation of the sheet resistance for the *n*-contact is

$$R_{NS} = \frac{\rho_N}{t_N}, \tag{3.3.14}$$

where ρ_N is the resistivity of the *n*-layer and t_N is the thickness of the *n*-layer.

The resistivity is

$$\rho_N = R_{NS} t_N = 5.13\ \Omega/\square \times 6.00\times10^{-5}\,\text{cm} = 3.08\times10^{-4}\,\Omega\cdot\text{cm}. \tag{3.3.15}$$

- Calculation of R_P

The *p*-resistivity is determined using another series of *p*-TLM pads fabricated with the same design as the *n*-TLM pads; the *p*-contacts are deposited on a *p*-doped layer of GaAs as illustrated in Figure 3-11. Thus, the method used for the *n*-TLM pads is applicable, and the *p*-sheet resistance R_{PS} is determined to be 12.6 Ω/□ while *p*-resistivity is calculated to be 5.04×10^{-4} Ω·cm. This equates $\rho_P \sim 1.6\rho_N$.

For the *p*-TLM pads shown in Figure 3-10, the current flows along *t* and the cross section area is $A=WZ$, where Z is the length of the pads.Thus, using the calculated value of the *p*-resistivity, the total *p*-resistance is given by

$$R_P = \frac{\rho_P t_P}{Area}, \tag{3.3.16}$$

where t_P is the thickness of the *p*-layer.

Hence,

$$R_P = \frac{(5.04\times10^{-4}\ \Omega\cdot\text{cm})(4.00\times10^{-5}\ \text{cm})}{(0.0150\ \text{cm})(0.0300\ \text{cm})} = 4.48\times10^{-5}\ \Omega \tag{3.3.17}$$

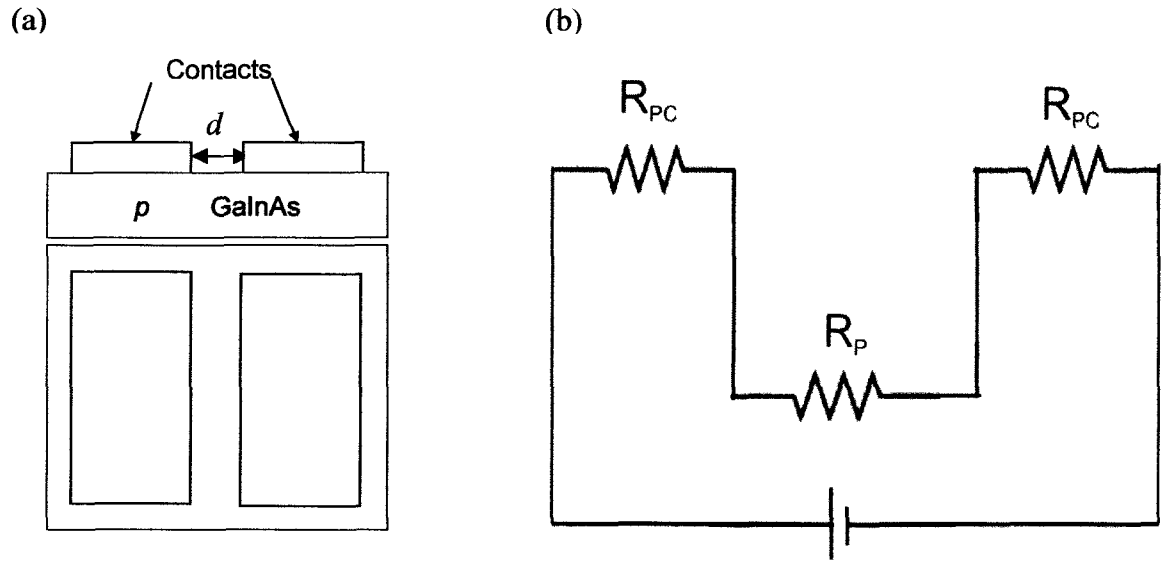

Figure 3-11: (a) Diagram presenting the structure of the new series of *p*-type TLM pads. (b) Circuit schematic of the new series of *p*-type TLM pads.

- Calculation of R_{TJ1} and R_{TJ2}

The resistance of the TJ, R_{TJ} is calculated by fitting the *V-J* Sentaurus simulation curve near the origin in x^3, giving $R_{TJx}=R_{TJxa}I^2+R_{TJxb}I+R_{TJxc}$. Similarly to the *V-I* curve of the TLM pads, Sentaurus simulation curve was fitted in x^3 as it depicts a nonlinear behavior and higher order terms do not contribute significantly. The current density *J* is used instead of the current *I* for the fit to be done over the same range as the fit of the experimental curve, giving a resistance in $\Omega\cdot cm^2$, which will then be converted in Ω using the dimensions of the TLM pads. R'_{TJ1} is calculated using the fit of the simulated *V-J* curve in forward bias, while R'_{TJ2} is calculated using the fit of the simulated *V-J* curve in reverse bias, shown in Figure 3-12. This gives

$$R'_{TJ1} = 7.9044\times10^{-12}J^2 + 1.2743\times10^{-8}J + 4.4363\times10^{-5}, \qquad (3.3.18)$$

and

$$R'_{TJ2} = 5.5591\times10^{-12}J^2 + 1.2774\times10^{-8}J + 4.4354\times10^{-5}. \qquad (3.3.19)$$

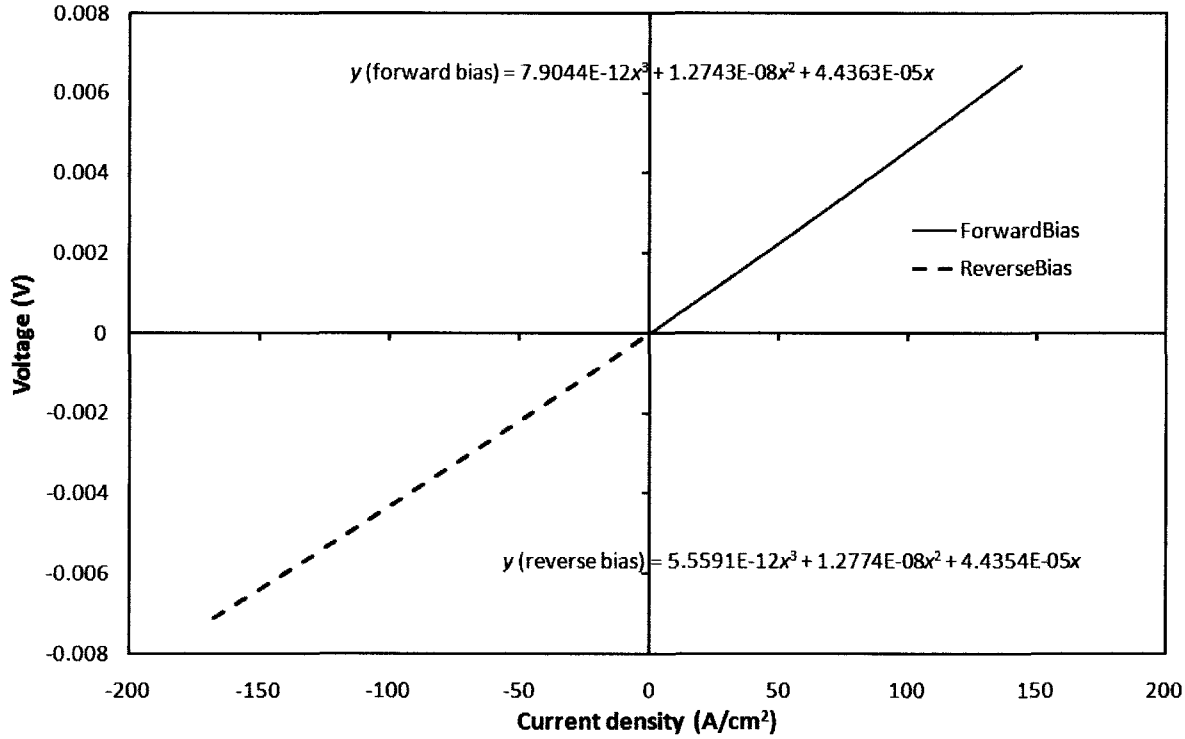

Figure 3-12: Sentaurus simulated *V-J* curve of a TJ of dimension 70 µm × 70 µm.

- Calculation of R_{PC}

R_{PC} can be defined as

$$R_{PC} = R_{PCa} I^2 + R_{PCb} I + R_{PCc}. \tag{3.3.20}$$

The experimental data and the Sentaurus simulation data are fitted over the same range in current density.

Replacing in Eq. (3.3.12) we get

$$aI^3 + bI^2 + cI + d = I\begin{pmatrix} 2R_{PCa} I^2 + 2R_{PCb} I + 2R_{PCc} + 2R_P + R_{TJ1a} I^2 + R_{TJ1b} I \\ + R_{TJ1c} + R_{TJ2a} I^2 + R_{TJ2b} I + R_{TJ2c} + R_N \end{pmatrix}. \tag{3.3.21}$$

When the voltage is 0, the current is also 0, thus $d = 0$. (3.3.22)

Matching the coefficients for I^3 gives

$$a = 2R_{PCa} + R_{TJ1a} + R_{TJ2a}. \tag{3.3.23}$$

Matching the coefficients for I^2 gives

$$b = 2R_{PCb} + R_{TJ1b} + R_{TJ2b}. \tag{3.3.24}$$

Matching the coefficients for I gives

$$c = 2\,R_{PCc} + R_{TJ1c} + R_{TJ2c} + 2R_P + R_N. \tag{3.3.25}$$

This method gives three equations with one unknown in each. These equations are solved for R_{PCa}, R_{PCb} and R_{PCc}, giving

$$R_{PCa} = \frac{\left(d - \left(R_{TJ1a} + R_{TJ2a}\right)\right)}{2}, \tag{3.3.26}$$

$$R_{PCb} = \frac{\left(c - \left(R_{TJ1b} + R_{TJ2b}\right)\right)}{2}, \tag{3.3.27}$$

and

$$R_{PCc} = \frac{\left(b - \left(R_{TJ1c} + R_{TJ2c} + 2R_P + R_N\right)\right)}{2}. \tag{3.3.28}$$

Solving Eq. (3.3.27) and (3.3.28) the p-contact resistance is calculated. The linear term of the contact resistance R_{PCc} calculated using the p-type TLM pads is between 8.6 Ω and 10.9 Ω. The average is 9.7 Ω or 4.4 mΩ·cm^2. See Table 3 for the values for the different spacing. The average value of the contact resistance for all the different spacing is

$$R_{PC} = 648.8I^2 - 118.6I + 9.7. \tag{3.3.29}$$

To verify the validity of our method, the values of the resistances are calculated for a TJ of dimension 70 μm × 70 μm. To fit the Sentaurus simulation to the experimental curve, the average of the results over all the different spacing is used. These values are converted in Ω·cm^2 by multiplying them by the area of the TLM pads, of which the dimensions are given in Table 2. The results are given in Table 4.

Table 3: Calculated values of the resistances for the *p*-type TLM pads of sample TJ1-A at 25°C.

d (μm)	R_N (Ω)	R_{PCa} (Ω/A^2)	R_{PCb} (Ω/A)	R_{PCc} (Ω)
100	1.7	789.0	-140.4	10.9
75	1.3	670.6	-120.2	9.6
50	0.86	659.3	-119.8	9.7
25	0.43	476.3	-94.1	8.6

Table 4: average values of the resistances and the specific contact resistivities calculated using the TLM pads.

R_N (Ω)	1.1
R_{PCa} (Ω /A^2)	649
R_{PCb} (Ω /A)	-119
R_{PCc} (Ω)	9.7
R'_{PCa} (Ω·cm^2/A^2)	0.29
R'_{PCb} (Ω·cm^2/A)	-5.3×10^{-2}
R'_{PCc} (Ω·cm^2)	4.3×10^{-3}

- Calculation of R_{PC}

The *p*-contact resistance is calculated using the value given in Table 4, and the area of a tunnel junction. The values obtained are

$$R_{PCaTJ} = \frac{R'_{PCa}}{4.9\times10^{-5}} = 6.0\times10^{3}\ \Omega/A^2, \tag{3.3.30}$$

$$R_{PCbTJ} = \frac{R'_{PCb}}{4.9\times10^{-5}} = -1.1\times10^{3}\ \Omega/A, \tag{3.3.31}$$

and

$$R_{PCcTJ} = \frac{R'_{PCc}}{4.9\times10^{-5}} = 88\,\Omega. \tag{3.3.32}$$

- Calculation of R_{PTJ}

Using(3.3.16), the resistance of the *p*-layer of a TJ of dimension 70 μm × 70 μm is calculated, giving

$$R_{PTJ} = \frac{(5.04\times10^{-4}\ \Omega\cdot\text{cm})(4\times10^{-5}\ \text{cm})}{4.90\times10^{-5}\ \text{cm}^2} = 4.11\times10^{-4}\ \Omega\ . \tag{3.3.33}$$

- Calculation of R_{NCTJ}

From the *n*-type TLM pads, we know R_{NC} and R_N. The n-contact resistance is calculated using the bottom contact area given in Table 2:

$$R_{NCTJ} = \frac{R'_{NC}}{BottomContactArea} = \frac{0.0005\ \Omega\cdot\text{cm}^2}{3.9\times10^{-4}\ \text{cm}^2} = 1.56\,\Omega\ . \tag{3.3.34}$$

- Calculation of R_{NTJ}

R_{NTJ} can be determined using the sheet resistance R_{NS}. The general formula for the resistance, knowing the sheet resistance, is given by Eq.(3.3.13). For the TJ structure, we first need to determine *Z* and *W*. The *n*-sheet resistance has a contribution only within the gap. The calculations are done under the assumption that the gap between the top contact and the bottom contact of the TJ is made of four rectangles of the *n*-layer, as illustrated in Figure 3-13. Thus, we have two rectangles of dimensions *MesaGap* × *MesaLength*, and two rectangles of dimensions *MesaGap* × *MesaWidth*.

Therefore, $Z = MesaGap$, and $W = 2MesaLength + 2MesaWidth$.

$$R_{NTJ} = \frac{R_{NS}Mesagap}{(2MesaLength + 2MesaWidth)}, \tag{3.3.35}$$

and

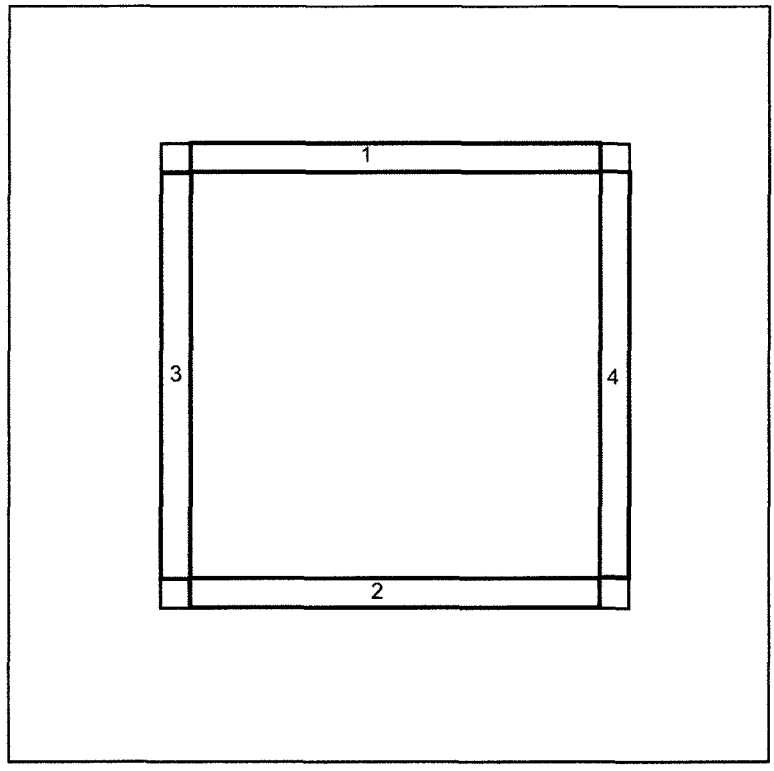

Figure 3-13: Calculations of R_{NTJ}: R_{NTJ} is calculated as if the gap between the top contact and the bottom contact of a TJ was made of four rectangles of the *n*-layer, labelled 1,2,3 and 4.

$$R_{NTJ} = \frac{5.13\ \Omega/\square \times 10\ \mu m}{(2\times 70\ \mu m + 2\times 70\ \mu m)} = 0.2\ \Omega. \qquad (3.3.36)$$

These calculations were done for a spacing of 10 μm. See Table 5 for the other dimensions.

- Total mesa resistance

The values added together give a total specific resistivity of 5 mΩ·cm^2 for the linear term, and a total mesa resistance 88 Ω for a TJ of dimension 70 μm × 70 μm. When this value is added to the simulation data, the initial slope is four times higher compared to the experimental curve, meaning the calculated resistance is too high. Another method needs to be used to accurately determine the mesa structure resistance.

B. Calculations for the TJ Mesa structures

The same calculations are done for a TJ.

The total resistance of the circuit of a TJ, shown in Figure 3-14 is

$$R_{TOT} = R_{NCTJ} + R_{NTJ} + R_{PCTJ} + R_{PTJ} + R_{TJ}. \tag{3.3.37}$$

Replacing Eq. (3.3.37) in (3.3.3) gives

$$V = I\left(R_{NCTJ} + R_{NTJ} + R_{PCTJ} + R_{PTJ} + R_{TJ}\right). \tag{3.3.38}$$

The *V-I* experimental curve measured on the TJ is fitted in x^3 from the origin to the tunneling peak, giving an expression of the form $V = aI^3+bI^2+cI+d$.

As previously for the *p*-TLM pads, all the resistances of the circuit have to be calculated.

- Calculation of R_{NTJ}, R_{NCTJ} and R_{PTJ}

  R_{PTJ}, R_{NCTJ} and R_{NTJ} are given by Eq. (3.3.33), (3.3.34) and (3.3.36).

- Calculation of R_{TJ}

R_{TJ} is calculated the same way as for the TLM pads. The *V-I* simulation curve is fitted in x^3 from the origin to the peak, giving

$$R_{TJ1} = 360I^2 - 6I + 0.8833. \tag{3.3.39}$$

- Calculation of R_{PCTJ}

Using the same method used previously for the *p*-type TLM pads, we get the following equation:

$$aI^3 + bI^2 + cI + d = I\left(R_{PCaTJ}I^2 + R_{PCbTJ}I + R_{PCcTJ} + R_{PTJ} + R_{NTJ} + R_{NCTJ} + R_{TJ1a}I^2 + R_{TJ1b}I + R_{TJ1c}\right). \tag{3.3.40}$$

When the voltage is 0, the current is also 0, thus $d = 0$. (3.3.41)

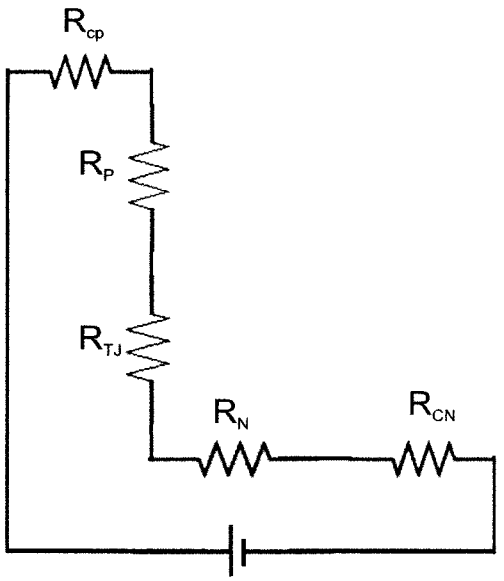

Figure 3-14: Circuit schematic of a TJ.

Matching the coefficients for I^3, gives

$$a = R_{\mathrm{PCaTJ}} + R_{\mathrm{TJ1a}}\,. \tag{3.3.42}$$

Matching the coefficients for I^2, gives

$$b = R_{\mathrm{PCbTJ}} + R_{\mathrm{TJ1b}}\,. \tag{3.3.43}$$

Matching the coefficients for I, gives

$$c = R_{PCcTJ} + R_{TJ1c} + R_{NCTJ} + R_{PTJ} + R_{NTJ}\,. \tag{3.3.44}$$

Solving for R_{PCaTJ}, R_{PCbTJ} and R_{PCcTJ} gives

$$R_{\mathrm{PCaTJ}} = a - R_{\mathrm{TJ1a}}, \tag{3.3.45}$$

$$R_{\mathrm{PCbTJ}} = b - R_{\mathrm{TJ1b}}, \tag{3.3.46}$$

and

$$R_{PCcTJ} = c - \left(R_{TJ1c} + R_{NCTJ} + R_{PTJ} + R_{NTJ}\right). \tag{3.3.47}$$

Replacing Eq. (3.3.33) (3.3.34) (3.3.36) and (3.3.39) in Eq. (3.3.45) (3.3.46) and (3.3.47), the *p*-contact resistance is calculated. The linear term of the contact resistance calculated using the TJ mesa structure is 1.08 mΩ·cm^2.

The equation of the *p*-contact resistance is

$$R_{PCTJ} = 4140I^2 - 444I + 21, \tag{3.3.48}$$

and

$$R'_{PCTJ} = 2.03\times10^{-01}J^2 - 0.0218J + 1.05\times10^{-3}. \tag{3.3.49}$$

The calculations were done for a gap of 10 μm. See Table 5 for the other sizes of the gap.

Table 5: *p*-contact resistance values for a TJ of dimension 70 μm × 70 μm of sample TJ1-A for different gap width at 25°C

d (μm)	R_{NTJ} (Ω)	R_{NCTJ} (Ω)	R_{PTJ} (Ω)	R_{PCTJ} (Ω)	R'_{PCTJ} (Ω)
10	0.183	1.56	4.11×10^{-4}	$4140I^2$-$444I$+21.4	$2.03\times10^{-1}J^2$-$0.0218J$+1.05×10^{-3}
6	0.110	1.56	4.11×10^{-4}	$4040I^2$-$434I$+20.9	$1.98\times10^{-1}J^2$-$0.0213J$+1.03×10^{-3}
4	0.073	1.56	4.11×10^{-4}	$3940I^2$-$424I$+20.5	$1.93\times10^{-1}J^2$-$0.0208J$+1.00×10^{-3}
2	0.037	1.56	4.11×10^{-4}	$4140I^2$-$424I$+20.5	$1.93\times10^{-1}J^2$-$0.0208J$+1.01×10^{-3}

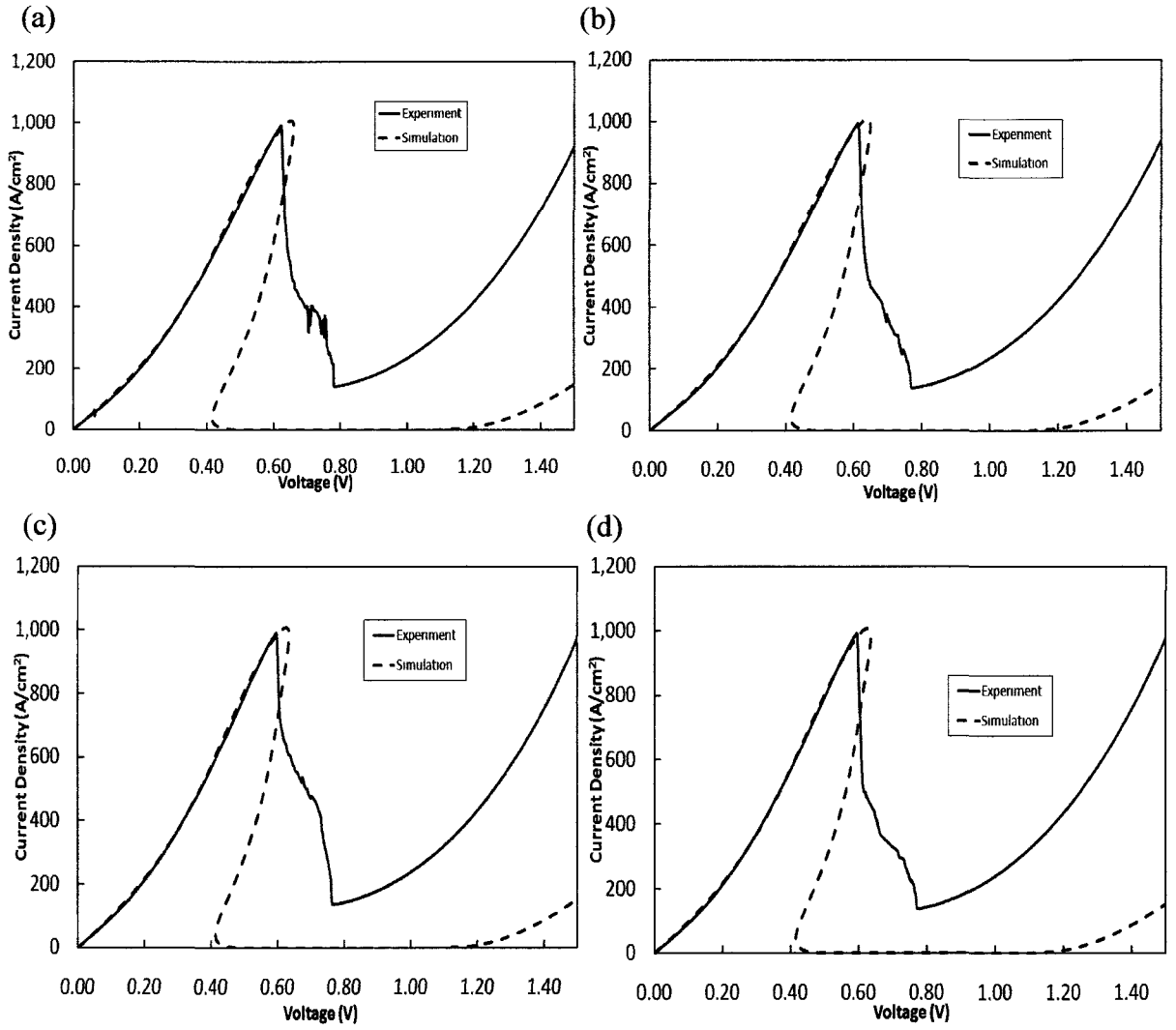

Figure 3-15: Comparison between simulation and experimental data using the calculated resistance, for TJ gap width between top and bottom contacts of (a) 10 μm (b) 6 μm (c) 4 μm and (d) 2 μm.

If only the size of the gap varies, and the TJ stays the same, the *p*-contact resistance is expected not to vary. All the values for the different gap widths are close, the difference being within 5%, which is acceptable. Using these calculations, the total resistance of the mesa structure was calculated, giving a specific resistivity of 1.08 mΩ·cm^2 and a resistance of 22.1 Ω for a TJ of dimension 70 μm × 70 μm. To verify our calculated resistance values, the calculated resistances are added to the Sentaurus simulation curve to match the experimental curve in the initial slope region. As shown in Figure 3-15, the two curves are almost identical in the initial slope region. Thus, the calculated values are acceptable.

Furthermore, the higher contribution to the mesa structure resistance comes from the *p*-contact resistance (21 Ω using the TJ circuit and 88 Ω using the TLM pads). The second higher resistance is the *n*-contact resistance with a value of 1.6 Ω. In comparison, the resistance of the *p*-doped layer which has a value of 4.11×10^{-4} Ω is negligible.

C. Conclusion

The *p*-contact resistance was calculated for the TLM pads, as well as for the TJ mesa structure, giving values of the linear term of respectively 4.90 mΩ·cm^2 and 1.05 mΩ·cm^2. After comparing both values, we can say the difference is a factor of four for the TLM pads. Using the calculations presented above, the total mesa resistance was calculated to be 5 mΩ·cm^2 for the linear term, or 88 Ω using the TLM pads and 1.08 mΩ·cm^2 or 22.12 Ω using the TJ circuit for a TJ of dimension 70 μm × 70 μm. These values are higher than expected, showing that fabrication adds resistances. The total mesa structure resistance calculated using the TJ circuit was used to match the simulation *J-V* curve to the experiment. The curves overlapped leading to the conclusion that the values calculated using the TJ measurements are acceptable, whereas when the values calculated using the TLM pads are added to the simulation curve, the initial slope of the simulation curve is to high compared to the experimental curve. Both results show a nonlinear component due to the *p*-contact resistance. This high *p*-contact resistance is indicative of metal insulator semiconductor (MIS) contacts created by the presence of oxygen in the fabrication chamber. MIS contacts are contacts in which an oxide layer is placed between the metal and the semiconductor, causing a current loss and thus increasing the resistance [26, 60]. The resistance calculations enable us to fit the simulation data to the experimental curve, but only in the initial slope region. Both curves are still very different within the NDR region and the excess current region. Additional information is required to fit the simulation to the experiment. The *J-V* behavior in the NDR region will be investigated in depth in a following section.

3.4 Low resistance TJ sample study

3.4-1 *J-V* curve at 25°C

The other TJ sample, referred to as sample TJ1-B, was fabricated using Zn/Au (75 nm thick) *p*-type contacts and Ti/Au (5/150 nm) *n*-type contacts. Figure 3-16 shows the *J-V* curve of a tunnel junction of dimension 70 μm × 70 μm at 25°C. The three main parts of the curve are observed. Similarly to TJ1-A, the tunneling peak current density value is ~950 A/cm^2 and the valley current density is ~250 A/cm^2. The tunneling peak voltage is 0.2 V while the valley voltage is 0.7 V. The resistance is much lower than on the previous sample. When comparing the simulation to the experiment, it can be observed that the nonlinear component of the initial slope region is due to the TJ only. In Figure 3-16, the Sentaurus simulation data is fitted to the experimental curve by adding a total resistance of 2.3 Ω. In the following sections, the mesa structure resistance of the TJ is calculated using two different methods introduced in Chapter 2, the TLM method and the Corbino method.

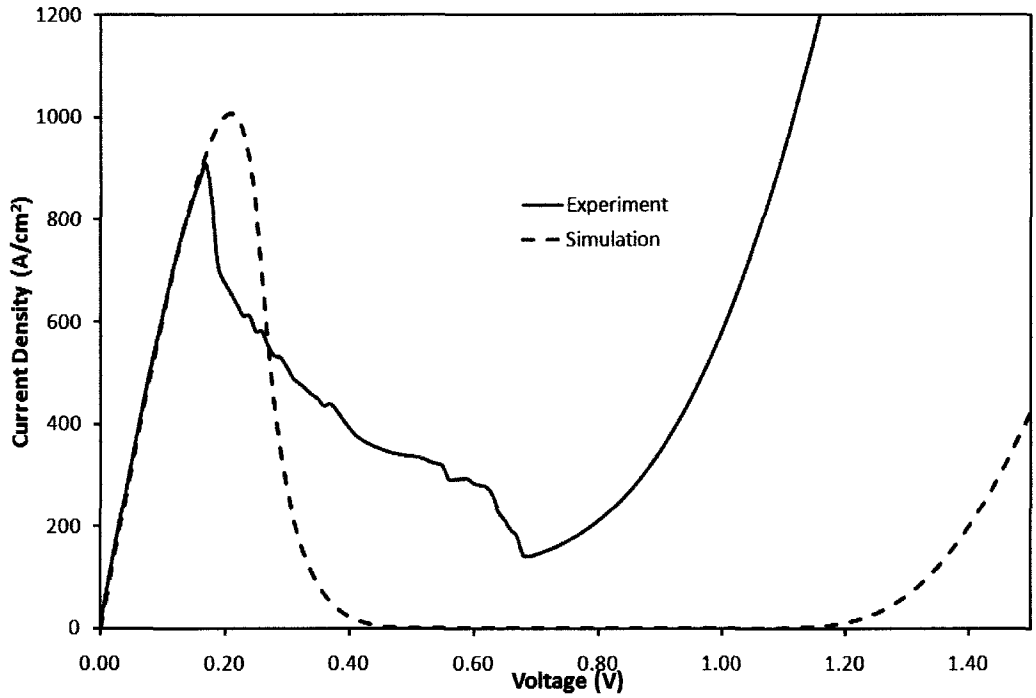

Figure 3-16: *J-V* curve of a tunnel junction from sample TJ1-B a top contact area of 70 μm × 70 μm at 25°C.

3.4-2 Mesa structure calculations

3.4-2.1 TLM method

On this sample, the *p*-TLM pads are fabricated the same way as the *n*-TLM pads; only the *p*-contact is etched over the semiconductor layer as shown in Figure 3-11. The *I-V* curves of *n*-type and the *p*-type TLM pads are linear, as shown in Figure 3-17 in the case of the *p*-type TLM pads. The method used on the *n*-type TLM pads in section 3.3 is applicable, and gives

R_{PS}=3.93 Ω/□, ρ_P = 0.16 mΩ·cm, where ρ_P is the resistivity of the *p*-layer,

R_{PC}= 0.43 Ω, R'_{PC}= 0.19 mΩ·cm^2;

R_{NS}=12.36 Ω/□, ρ_N = 0.74 mΩ·cm;

and R_{NC}= 1.05 Ω; R'_{NC}= 0.47 mΩ·cm^2;

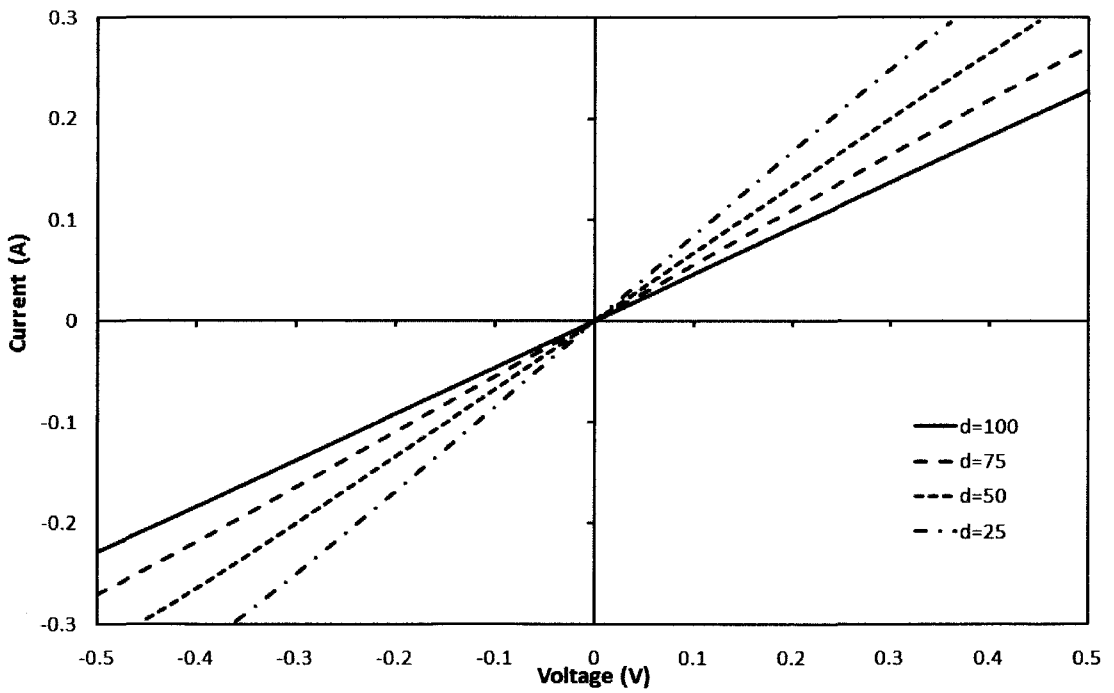

Figure 3-17: *I-V* curve of the *p*-type TLM pads of sampleTJ1-B.

3.4-2.2 Corbino method

Corbino are similar to TLM pads, but they use a cylindrical geometry, as shown in Figure 3-18. As explained in Chapter 2, they avoid current spreading and crowding as well as edge current, which can seriously affect the results. They are therefore more accurate than TLM pads. The *I-V* curves are measured by applying a voltage between the inner and the outer metal contact, for different gap spacing. The spacing values are 5, 10, 20, 40, 80 and 100 μm. The *I-V* characteristics are linear between -0.3 and 0.3 V, as shown in Figure 3-19 enabling us to extract the total resistance using Eq. (3.3.3).

Figure 3-18: Picture of a series of fabricated Corbinos.

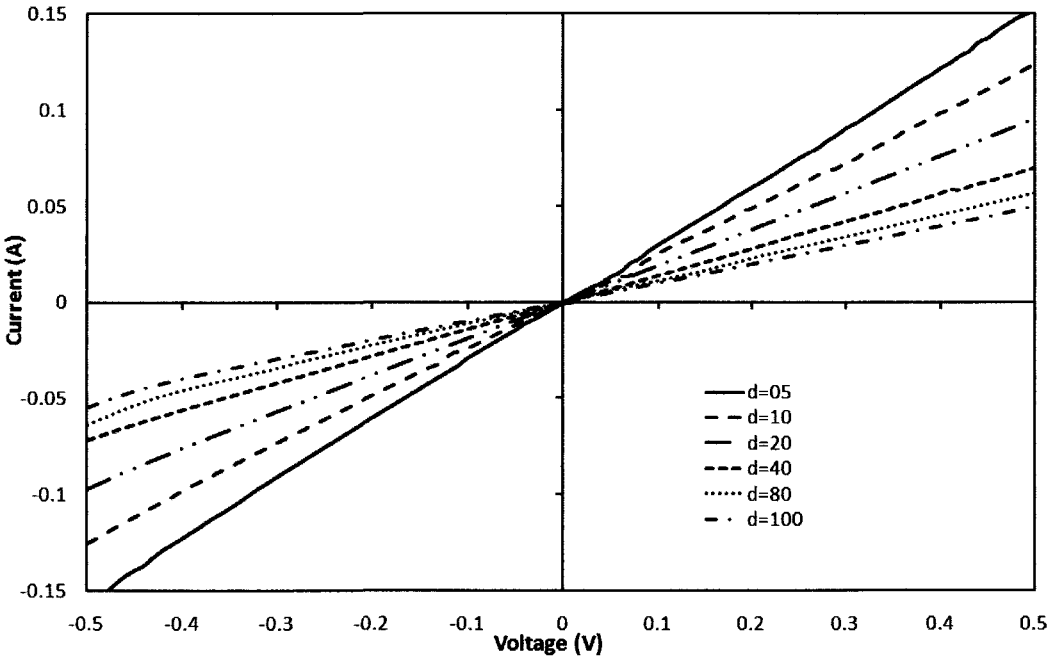

Figure 3-19: *I-V* curves measured on *n*-Corbinos for different spacing between the inner and the outer metal contacts.

Plotting the resistance as a function of the spacing gives a nonlinear relation, that can be transformed into a linear relation using the correction factor from Eq. (2.3.20). The graph of the total resistance as a function of the spacing for the *n*-Corbinos is shown in Figure 2-22. The corrected values give a linear curve, and its equation is given by Eq. (2.3.21).
From Eq. (2.3.21), the slope is given by

$$slope = \frac{R_S}{W_C}. \tag{3.4.1}$$

Isolating R_S gives

$$R_S = slope W_C, \tag{3.4.2}$$

with

$$W_C = 2\pi r_1. \tag{3.4.3}$$

Replacing Eq. (3.4.3) in Eq. (3.4.2) gives

$$R_S = 2\pi r_1 slope. \tag{3.4.4}$$

The y-intersept gives the contact resistance, $y(0) = 2R_C$. Thus,

$$R_C = \frac{y(0)}{2}. \tag{3.4.5}$$

The measurements are done for *n*-structure and *p*-structure.

- For the *n*-Corbinos, the total resistance is

$$R_T = 0.1805s + 2.8963, \tag{3.4.6}$$

where s is the spacing between the inner and the outer metal contacts.
Replacing the value in Eq. (3.4.4) and (3.4.5) gives

$$R_{NS} = (1805\ \Omega/\text{cm})2\pi(0.0035\ \text{cm}) = 39\ \Omega/\square, \tag{3.4.7}$$

and

$$R_{NC} = \frac{2.8963}{2} = 1.5\ \Omega, \tag{3.4.8}$$

and the specific contact resistivity is

$$R'_{NC} = R_{NC}Area = R_{NC}\pi(r_1)^2 = (1.45\ \Omega)\pi(0.0035\ \text{cm})^2 = 0.056\ \text{m}\Omega\cdot\text{cm}^2. \tag{3.4.9}$$

Using Eq.(3.3.15), the resistivity can be calculated, giving

$$\rho_N = 39\ \Omega/\square \times 6.00\times10^{-5}\text{cm} = 2.4\ \text{m}\Omega\cdot\text{cm}. \tag{3.4.10}$$

- For the *p*-CTLM, the total resistance is

$$R_T = 0.0517s + 1.7957. \tag{3.4.11}$$

Using these values in Eq. (3.4.4) and (3.4.5) gives

$$R_{PS} = (517\ \Omega/\text{cm})2\pi(0.0035\ \text{cm}) = 11\ \Omega/\square, \tag{3.4.12}$$

and

$$R_{PC} = \frac{1.7957}{2} = 0.9\ \Omega. \tag{3.4.13}$$

Multipliying by the area gives the specific contact resistivity:

$$R'_{PC} = R_{PC}Area = R_{PC}\pi(r_1)^2 = (0.90\ \Omega)\pi(0.0035\ \text{cm})^2 = 0.035\ \text{m}\Omega\cdot\text{cm}^2. \tag{3.4.14}$$

Using Eq. (3.4.9), the resistivity can be calculated, giving

$$\rho_P = 11\,\Omega/\square \times 4.00\times10^{-5}\ \text{cm} = 0.40\ \text{m}\Omega\cdot\text{cm}\,. \tag{3.4.15}$$

3.4-2.3 Mesa structure resistance of a TJ of dimension 70 μm × 70 μm

The values of the resistances of the *n*-layer and the *p*-layer and the contact resistances were then calculated for a TJ mesa structure of dimension 70 μm × 70 μm. The values of R_{NC} and R_N can be calculated, using Eq. (3.3.34) and (3.3.35), giving $R_{NC} = 1.48\ \Omega$ and $R_N = 0.4\ \Omega$ using the TLM measurements, and $R_{NC} = 0.18\ \Omega$ and $R_N = 1.4\ \Omega$ using the Corbino measurements.

The *p*-contact resistance and the resistance of the *p*-layer can be calculated using

$$R_{PC} = \frac{R'_{PC}}{MesaArea}, \tag{3.4.16}$$

and

$$R_P = \frac{\rho_P t_P}{MesaArea}\,. \tag{3.4.17}$$

Using Eq. (3.4.16) and (3.4.17) gives $R_{PC} = 3.9\ \Omega$ and $R_P = 0.1\ \text{m}\Omega$ using the TLM pads and $R_{PC} = 0.7\ \Omega$ and $R_P = 0.3\ \text{m}\Omega$ using the Corbinos. The total resistance of the mesa structure is then calculated, giving a specific resistivity of $2.9\times10^{-4}\ \Omega\cdot\text{cm}^2$ and a total mesa structure resistance of 5.9 Ω using the TLM pads and a specific resistivity of $1.1\times10^{-4}\ \Omega\cdot\text{cm}^2$, and a total mesa structure resistance of 2.3 Ω using the Corbinos. These values are substracted to the experimental *J-V* curves of the TJ in order to compare both method, as shown in Figure 3-20. The resistance calculated using the TLM pads is too high. After substracting the resistance calculated using the Corbinos, the experimental *J-V* curve matches the simulation curve in the initial slope region, while the *J-V* curve is shifted towards the negative voltages when the resistance calculated with the TLM pads is used, meaning the Corbinos gives more accurate results than the TLM pads. The calculated value of the total mesa structure resistance using the Corbino method is 2.3 Ω, which corresponds to the value used to fit the simulation to the experiment in Figure 3-16.

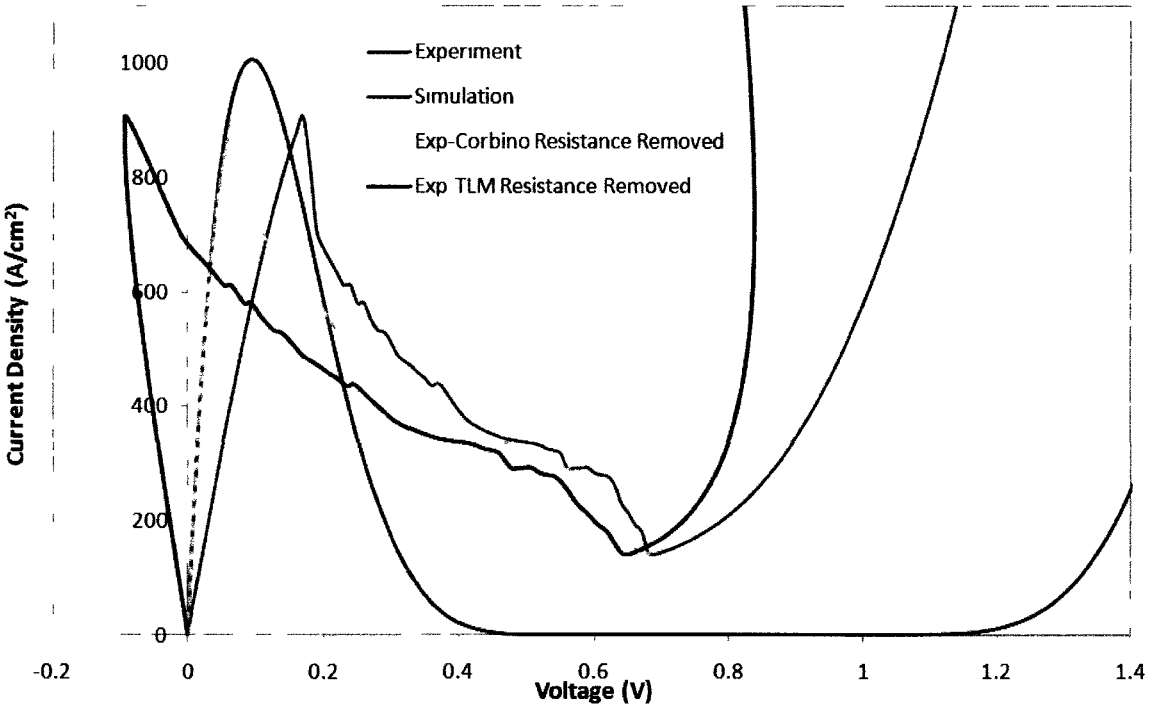

Figure 3-20: Comparison between simulation (red line) and experimental *J-V* curve of a TJ of top contact area of 70 μm × 70 μm after subtracting the mesa structure resistance calculated using the TLM pads (black line) and the Corbino (green dashed line). The initial experimental *J-V* curve is shown (blue line).

As explained previously for sample TJ1-A, the resistance calculations enable us to fit the experimental curve to the simulation in the initial slope region, but not in the NDR region and the excess current region. The simulation data can be fitted analytically to the experimental curve based on the following equation [26]

$$J_{excess} = J_V \exp(A(V - V_V)), \tag{3.4.18}$$

where J_{excess} is the excess current density, J_V and V_V are the valley current density and valley voltage respectively, and A is a constant. The result is shown in Figure 3-21. The simulation now agrees with the experimental curve in the initial slope region and the excess current region, but the shape of the experimental *J-V* curve does not follow the simulation data in NDR region. To get a better understanding of the TJ characteristic, section 3.5 will present a study of the TJ behavior in the NDR region.

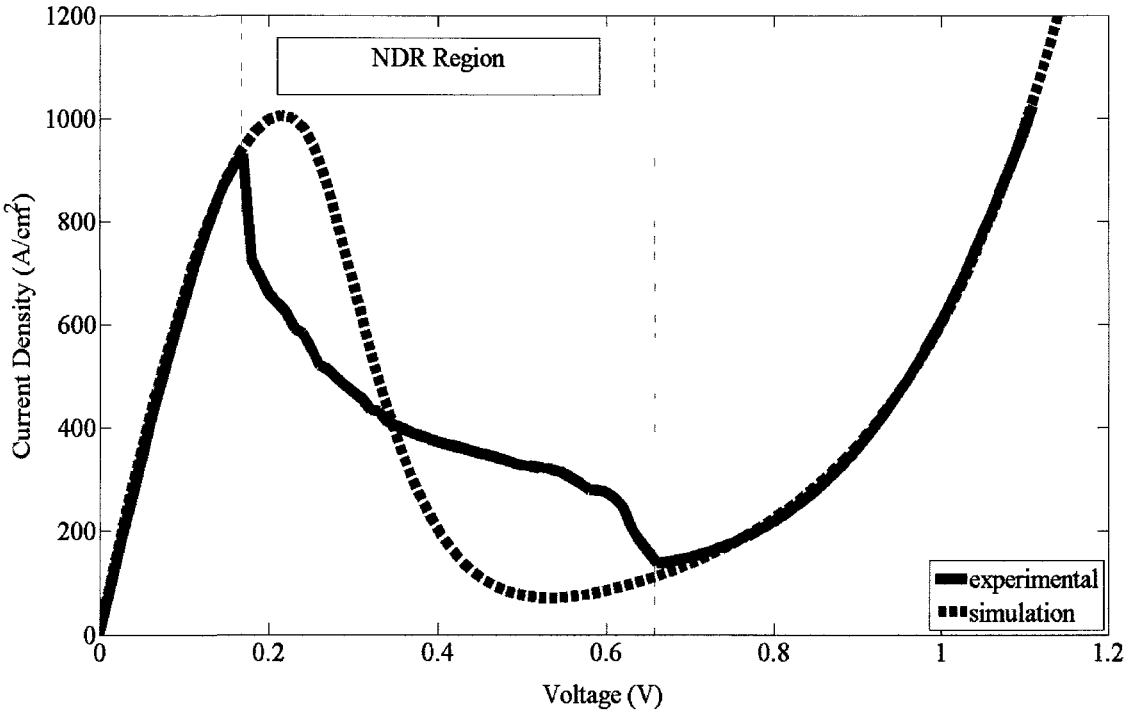

Figure 3-21: Comparison between experimental data (red line) and simulation curve (blue dashed line) after fitting analytically the simulation data in the excess current region.

3.5 Time-dependent measurements of the sample TJ1-B

Even though only the initial slope region is relevant for MJ solar cells (which have an operating point at ~7 A/cm^2 at 500 suns), the characterisation of TJ over their whole operating range is needed to calibrate in detail the solar cell – and particularly the TJ – numerical models. This section presents a study of the time-dependent behavior of a TJ biased within the NDR region to obtain a more accurate location of the peak and valley currents from the *J-V* curve, and fit the simulation models to the experiment [58]. First, a typical *J-V* curve of a TJ is presented, and the physical processes responsible for the NDR region of the curve are discussed. This is followed by the experimental method used to obtain the time-dependent measurements. Using the oscillations in current density and voltage, the current density is graphed as a function of the voltage, giving a more complete *J-V* curve than the time-averaged measurement. Knowing the exact value of the tunneling

peak current density will provide us with the theoretical maximum current density for which a MJ solar cell could operate using an AlGaAs/AlGaAs TJ. If the tunneling peak is close to the operating point of the solar cell, the overall MJ solar cell will be sensitive to a change in illumination. If the current flowing through the cell increases higher than the peak, it will experience a substantial voltage drop across the TJ as the operating point moves into the excess and thermal currents region of the *J-V* curve.

3.5-1 Theory

As mentioned previously in section 2.3, an ideal TJ *J-V* curve, shown in Figure 3-22(a), consists of three main regions: the initial slope region, dominated by band-to-band tunneling, the NDR region, and the excess and thermal current region [26] where each current component varies exponentially with the voltage. The thermal current is the current of a *p-n* junction diode in forward bias, while the excess current is due to tunneling through interface states located within the bandgap [26]. The NDR region is very different from the other regions: the current decreases when the voltage increases creating a slope in the opposite direction than the initial slope region. Furthermore, time-averaged measurements are accurate in the initial slope and the excess current regions, but they are unable to give the exact positions of the peak and valley currents because of nonlinear oscillations induced by the equivalent circuit in the NDR region [61]. When the system is biased inside the NDR region, the measurement circuit becomes unstable and the voltage and current oscillate, leading to inaccuracy in measuring the peak and valley currents [61]. Due to these nonlinear oscillations, the experimental *J-V* curve presents a plateau-like behaviour on the time-averaged measurements instead of following the theoretical curve, as illustrated in Figure 3-22(b) [40, 62].

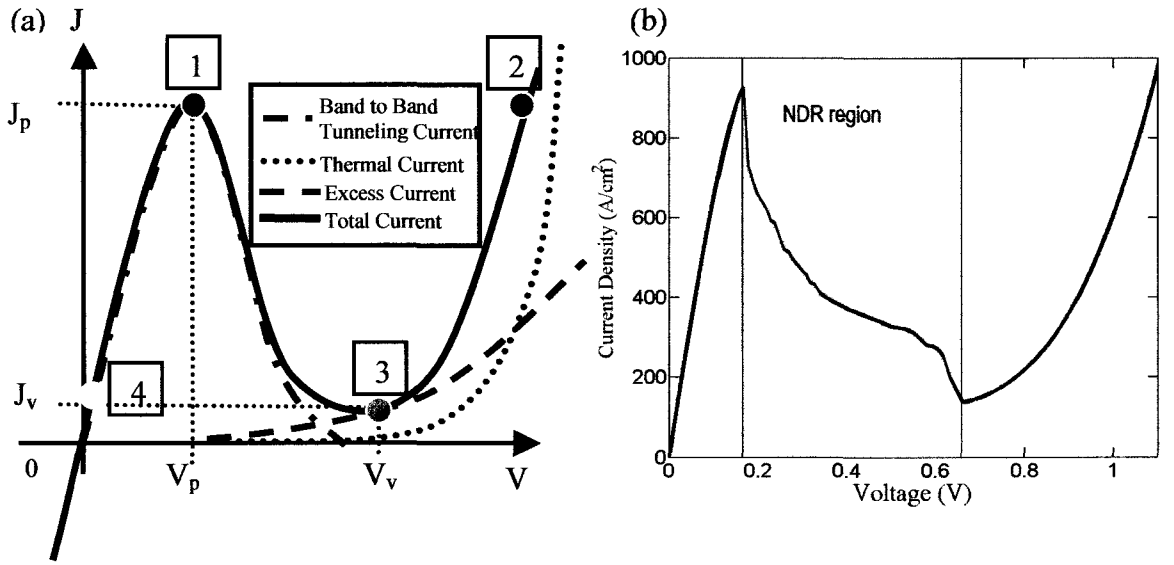

Figure 3-22: (a) Ideal *J-V* characteristics of a TJ, displaying its main components: band-to-band tunneling current (dash-dotted line); exponential excess current (dashed line); and thermal current (dotted line). The circles indicate the peak (blue, #1) and valley (green, #3) of the *J-V* behaviour. (b) Experimental *J-V* curve of an AlGaAs/AlGaAs TJ at 25°C; the NDR region is located between the peak tunneling current density and the valley current density, as identified by the shaded region [40].

The origin of the oscillations can be understood by studying the equivalent circuit shown in Figure 3-23 and using the load-line analysis method. The equivalent circuit consists of a tunnel diode in series with an inductance L and a series resistance R_S, and in parallel with a capacitor C. Experimentally, the parasitic inductance L originates from the measurement probes and the parasitic capacitance C is created by the depletion region of the *p-n* junction. The capacitance, the inductance and the series resistance created by the mesa structure and the measurement setup are represented on the experimental TJ *J-V* characteristic, but they are not present in a full MJ solar cell.

From Kirchhoff's voltage law, the external voltage V_{ext} is described by

$$V_{ext} = L\frac{dI_{TOT}}{dt} + R_S I_{TOT} + V_{\text{int}}, \tag{3.4.19}$$

where V_{int} is the internal voltage of the TJ, V_{ext} is the total output voltage and I_{TOT} is the total current.

The total current I_{TOT} is given by

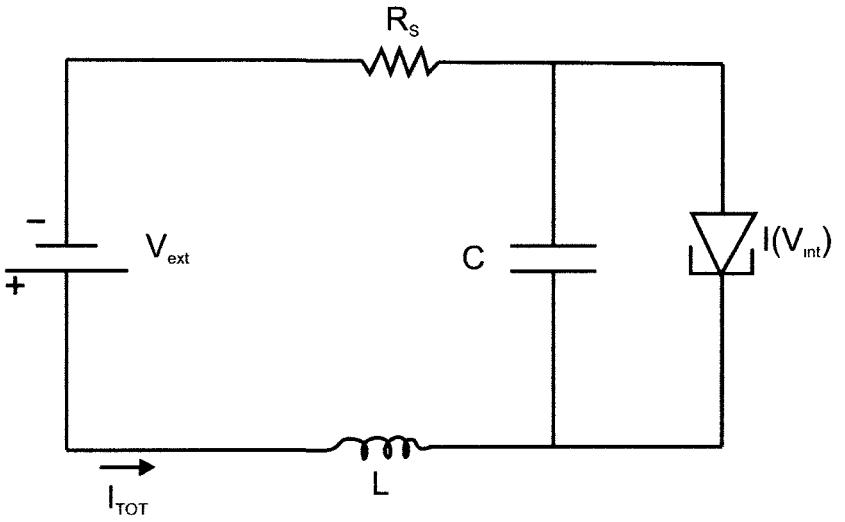

Figure 3-23: Equivalent circuit including a TJ and the experimental circuit [40].

$$I_{TOT} = C\frac{dV_{int}}{dt} + I(V_{int}). \tag{3.4.20}$$

By combining both Eq. (3.4.19) and (3.4.20), the differential equation describing the equivalent circuit is obtained [43]:

$$V_{ext} = LC\frac{d^2V_{int}}{dt^2} + R_SC\frac{dV_{int}}{dt} + V_{int} + L\frac{dI(V_{int})}{dt} + R_SI(V_{int}). \tag{3.4.21}$$

Eq. (3.4.21) can be solved over the three domains corresponding to the initial slope region, the NDR region, and the excess and thermal currents region. The solutions for the initial slope region and the excess and thermal currents region are finite and stable, whereas the solution for the NDR region is unstable. As a result, when the system is biased in the NDR region, the instability of the circuit leads to a quick transition to the thermal current region; this can be seen as a transition from point 1 to 2 in Figure 3-22(a). From this point on the *J-V* curve, the system moves along the curve to the valley current, or point 3 in Figure 3-22(a). This point is also within the unstable NDR region, and leads to another quick transition to the initial slope region from point 3 to point 4. More detailed explanations can be found in the literature [43] and this phenomenon will be studied experimentally later on.

Eq. (3.4.21) is analogous to the equation describing a Van der Pol oscillator [63]. A Van der Pol oscillator is a nonlinear oscillator showing nonlinear damping. It is described by the following equation

$$\frac{d^2x}{dt^2} + \mu(x^2 - 1)\frac{dx}{dt} + x = 0, \tag{3.4.22}$$

where $\mu > 0$ is a parameter [64].

The Van der Pol equation is similar to the equation of a simple harmonic oscillator, but with a nonlinear damping term $\mu(x^2 - 1)\frac{dx}{dt}$ describing a negative damping in the case where $|x| < 1$. This negative damping increases the magnitude of the oscillation. For $|x| > 1$, the equation describes a positive damping that decreases the amplitude of the oscillations. The Van der Pol oscillator can be generalised by the Liénard systems. These systems are described by differential equations of the form [64]

$$\frac{d^2x}{dt^2} + f(x)\frac{dx}{dt} + g(x) = 0 \tag{3.4.23}$$

where $f(x)$ is a nonlinear damping force while $g(x)$ is a nonlinear restoring force. Therefore, the amplitude is increased for small oscillations, and decreased for large oscillations. Such a system has a unique stable limit cycle, or isolated closed trajectory. Eventually, the system settles at intermediate amplitude with self-sustained oscillations. In this case, the energy dissipated over one cycle balances the energy gained to increase the amplitude of the oscillations over another cycle. The shape of the oscillations can be explained using the Van der Pol equation. In the case where $\mu >> 1$, the limit cycle consists of a slow build-up, corresponding to a transition from 1 to 2 on Figure 3-22(a), followed by a sudden discharge corresponding to a transition from 2 to 3 on Figure 3-22(a) and so on. Such oscillations are called relaxation oscillations, because stress is accumulated during the build-up and relaxed during the sudden discharge [63]. This explains the behavior of the oscillations observed when a TJ is biased in the NDR region.

3.5-2 Methodology

The time-averaged measurements are performed with a Keithley 2601A sourcemeter using the four-wire remote sensing measurement technique with an integration time at each data point of 84 ms. As displayed in Figure 3-22(b), the NDR region is located between 0.2 and 0.7 V. The Keithley 2601A sourcemeter has an internal feedback, which tries to stabilize the circuit and therefore interferes with the nonlinear oscillations of the tunnel junction. To accurately measure these oscillations a Tektronix DC Power Supply model 280 is used in a 2-wire configuration to bias the voltage within the NDR region at 0.6 V, as illustrated in Figure 3-24. The width of the NDR region is narrowed to 0.1 V by the addition of a series resistance. The oscillations in current and voltage are measured using an Agilent oscilloscope model DSO6014A; one oscilloscope probe measures the voltage across the TJ, while the other measures the voltage across both the TJ plus a 3 Ω resistance. The value of the resistance was chosen to obtain the best possible accuracy in measuring the oscillations with the available equipment. The voltage across the 3 Ω resistance is calculated from the difference between the voltages measured by both probes, giving the value of the current using Ohm's law. The experimental circuit is illustrated in Figure 3-25. Both time-dependent and time-averaged measurements were conducted under dark, temperature-controlled conditions with the temperature set at 25.0±0.1°C using a thermo-electric cooler and a resistance temperature detector.

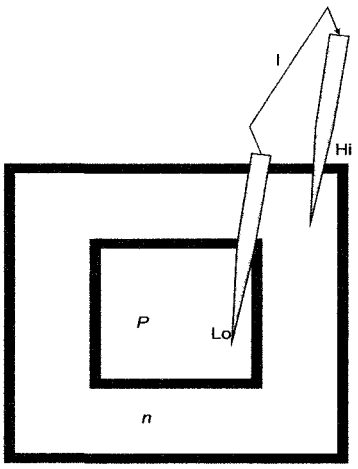

Figure 3-24: Schematic of the two-wire measurement technique.

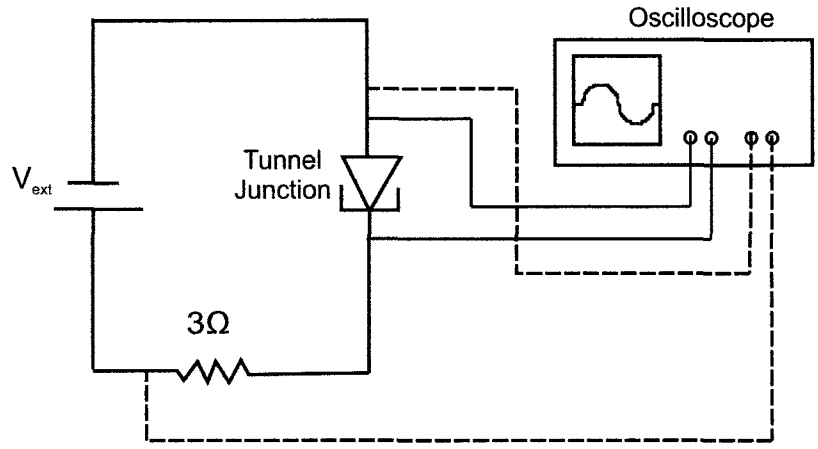

Figure 3-25: Schematic of the experimental circuit used to measure the time-dependent behavior of a TJ; one probe of the oscilloscope (red dashed line) measures the voltage across the TJ and a 3 Ω resistance while the other probe (blue line) measures the voltage across the TJ [40].

3.5-3 Results

A typical time-averaged AlGaAs/AlGaAs TJ *J-V* curve is presented in Figure 3-22(b), showing a tunneling peak of 950 A/cm^2. Oscillations in the current density and voltage of the circuit are measured for a bias corresponding to the NDR region, as shown in Figure 3-26. The period is observed to vary from 1.1×10^{-6} to 1.9×10^{-6} s between two consecutive oscillations, corresponding to a variation of ~0.8×10^{-6} s. It has been found in the literature that the period depends on the bias in the NDR region [65]. Therefore, the variation in the period could be due to the precision of the power supply (0.01% + 3 mV) under the varying load of the oscillating TJ. Furthermore, the shape of the oscillations is consistent with the theory presented in section 3.6-1. Due to these oscillations, an average of the signal over time results in the loss of important information, such as the precision in the tunneling peak's magnitude, the valley current and voltage, and the shape of the *J-V* curve within the NDR region. A more accurate *J-V* curve is recreated from the time-dependent measurement in Figure 3-27, revealing a larger tunneling peak current. Using this new *J-V* curve, the

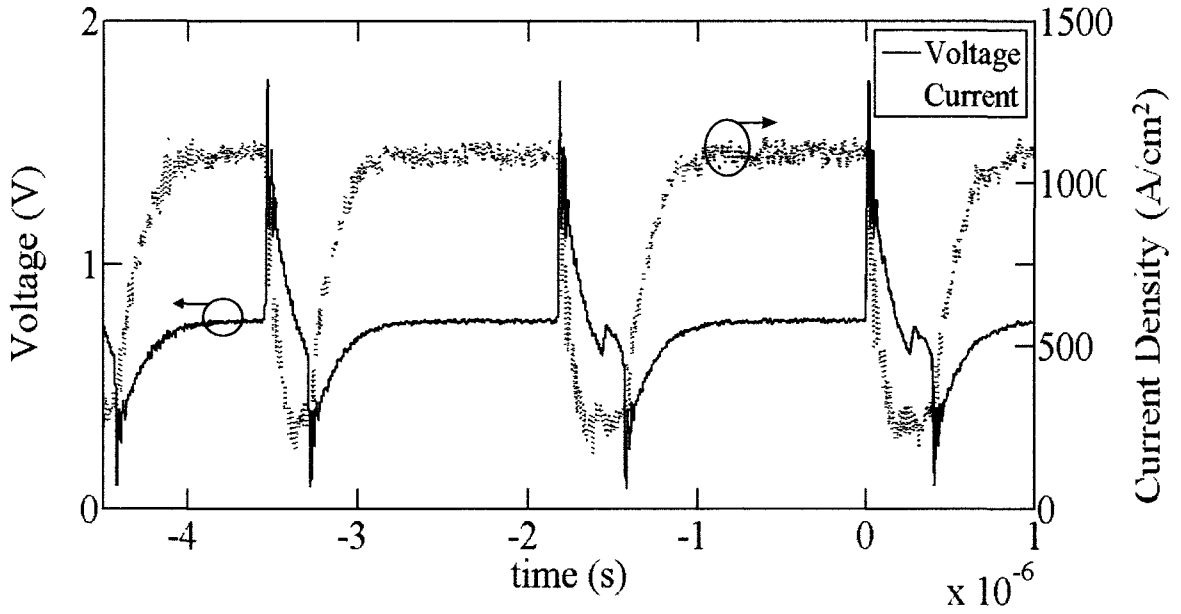

Figure 3-26: Sample of time-dependent current-density and voltage oscillations measured over time when the system is biased inside the NDR region. The oscillations in voltage are displayed by the left *y*-axis and correspond to the blue line, while the oscillations in current are displayed by the right *y*-axis, corresponding to the red dotted line [40].

position of the peak was measured to be between 1050 A/cm^2 and 1150 A/cm^2, which corresponds to a variation of ~9%. The value of the peak current obtained is between 10 and 20% higher than the one obtained using the time-averaged measurements, which confirms that the time-averaged data obscures some information.

Ideally, the time-dependent curve would follow exactly the time-averaged curve and the simulated curve in the initial slope region and the excess current region, giving an extended peak corresponding to the exact value of the peak and the valley current densities. In our measurements, the time-dependent data does not follow exactly the time-averaged data especially in the excess current region, but shows smaller oscillations. These differences are due to sources of error in the measurements.

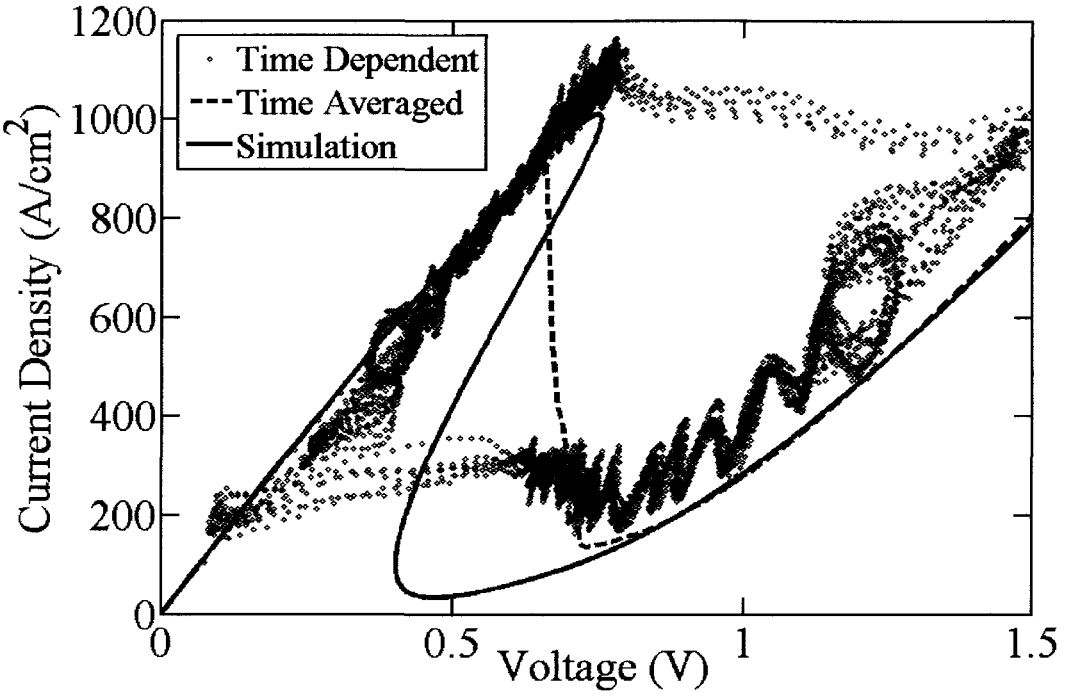

Figure 3-27: *J-V* curve of an AlGaAs/AlGaAs TJ presenting time-dependent (black dots) and time-averaged (blue dashed line) measurements plus the simulated curve (red line) [40].

The major source of measurement error comes from the oscilloscope. The error on the voltage measurements done using the oscilloscope is ±80 mV. The sample rate of the oscilloscope is 2 GSa/s, which corresponds to 2000 data points per oscillation. Thus, the sample rate is much larger than the frequency of the oscillations, in the range of 5×10^5 Hz to 9×10^5 Hz. The error on the oscilloscope measurements comes from its sensitivity, which did not allow us to use a resistance lower than 3 Ω.

Furthermore, a larger series resistance (on the order of 10 Ω) would reduce the noise in the current density measurements. However, when the series resistance is added, the width of the NDR region is significantly narrowed due to a tilt of the *J-V* curve towards the right, making it more difficult to bias the system within this region. A 3 Ω resistance gives a more manageable NDR width of 0.1 V, which requires a power supply with a resolution of at least 0.01 V. The Tektronix power supply used in this experiment only has a resolution of 0.1 V, which limited the accuracy of the measurements. On the other hand, using a 1 Ω resistance

would increase the width of the NDR region, but the oscilloscope was not sensitive enough to accurately measure the oscillations. A more sensitive oscilloscope would improve the noise at low-resistance measurements. To accurately measure the voltage across a 1 Ω resistance, the oscilloscope should be able to measure at least the minimum current density, corresponding to the valley current, which has a value of 150 A/cm^2, corresponding to 7 mV. Thus, the minimum sensitivity of the oscilloscope should be 7 mV.

Finally, the system is not perfectly isolated and external factors affect the oscillations. Electronic noise from high current sources such as the temperature controller near the apparatus interferes with the frequency of the oscillations.

The time-dependent behavior of the oscillations was simulated using MATLAB and compared to the experimental data, as illustrated in Figure 3-28. J and the V obtained from the Sentaurus simulations are input as the characteristics of the isolated TJ. Eq. (3.4.21) is solved numerically using Euler's method [66] for an initial voltage bias corresponding to V_{ext} and given values of R_S, L and C, allowing one to simulate the oscillations in current density and voltage across the device. The results vary as a function of time in the NDR region. V_{int} is calculated for each time step of the simulation and the corresponding current density is determined, resulting in the oscillations depicted in Figure 3-28(a) and (b). The time step used is 1×10^{-10} s. V_{ext} is the bias voltage used for the experimental measurements, while R_S, L and C are estimated to match the MATLAB simulation to the experiment.

R_S takes into account the 3 Ω series resistance plus the resistance inherent to the measurement setup. R_S was estimated to be 10 Ω using the MATLAB simulations. The amplitude and the period were calibrated to match the experimental curve. The amplitude and the period depend on the inductance and the capacitance: the amplitude of the oscillations increases with the capacitance, while the period increases with the inductance. Using these simulations, the value of the capacitance and the inductance were estimated at 3×10^{-9} F and 3500×10^{-9} H. The MATLAB simulation results accurately follow the experimental curve in the time-dependent current density oscillations, shown in Figure

3-28(a). The shape of the oscillations is the same for both the experimental curve and the MATLAB simulation data. Moreover, the shape of the simulated voltage oscillations, shown in Figure 3-28(b), does not follow exactly the experimental curve. The amplitude and the period agree, but the shape of the peak is different and could not be improved by changing the parameters of the MATLAB simulation. This could be corrected by improving the MATLAB simulation model. Furthermore, a time-dependent *J-V* curve is obtained by plotting the simulated current density and voltage against each other, as presented in Figure 3-28(c). This curve is compared to the experimental time-averaged and time-dependent *J-V* curves. The time-dependent experimental and simulated curves agree with each other, confirming the values of the capacitance and the inductance.

These values are different from the ones given in the literature for a GaAs/GaAs TJ [61], which were 54×10^{-6} H for the inductance 15×10^{-9} F for the capacitance and 1.4 Ω for the resistance. These values are highly dependent on the measurement setup because the inductance comes from the measurement circuit; different probes were used than in the literature. The capacitance is different because different material thicknesses and dopants were used, and the resistance is due to the measurement setup, it is different between each touchdown with the probes because the two-wire measurement technique is used.

The simulation model could be improved. Using fourth order Runge-Kutta method would solve the differential equation more accurately [66]. With this method, it takes more time to generate the simulations and the computer could not support them. Improving this as well as the experimental setup would help match the simulation to the experiment.

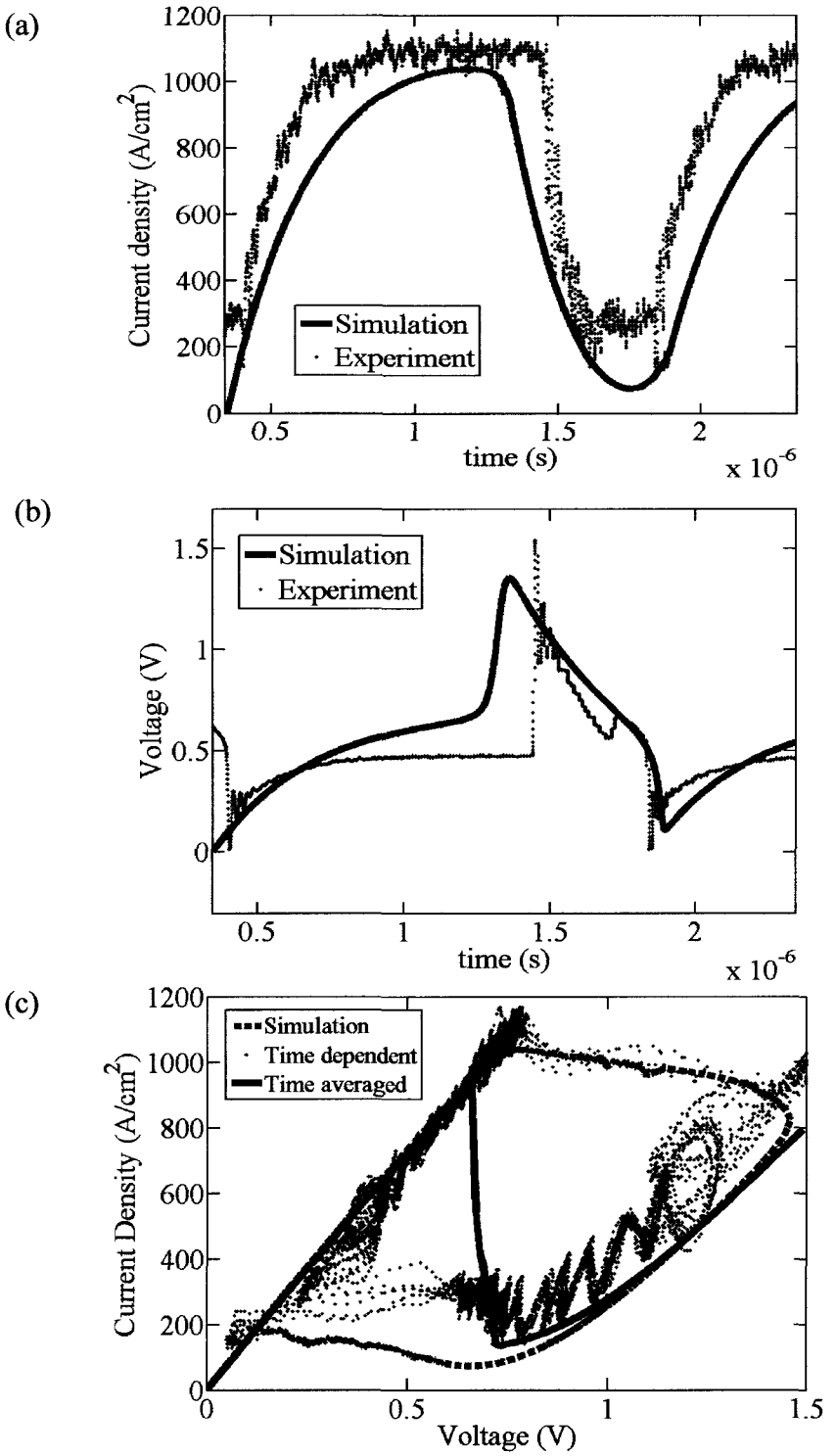

Figure 3-28: Sample of experimental (red dots) and simulated (blue line) time-dependent (a) current-density and (b) voltage oscillations measured over time when the system is biased inside the NDR region. (c) *J-V* curve of an AlGaAs/AlGaAs TJ presenting the simulated curve (blue dashed line) plotted using the simulated oscillation from (a) and (b), plus the experimental time-dependent (red dots) and time-averaged (black line). [Simulation model developed by Florent Chagnoleau]

The oscillations were measured with the Keithley 2601A sourcemeter using the four-wire remote sensing technique and the two-wire measurements technique as shown in Figure 3-29. The period of the oscillations measured using the four-wire configuration is ~ 3×10^{-5} s, while the period of the oscillations using the two-wire measurements technique is ~1.5×10^{-5} s. The values of C and L are higher with the Keithley 2601A sourcemeter using the two-wire configuration than with the Tektronix, by 0.5×10^{-9} F and 3.7×10^{-5} H. When the Keithley 2601A sourcemeter is used in the four-wire configuration, C is higher by 1×10^{-9} F than when the Tektronix was used while L is twice the value obtained with the Tektronix. Thus, the value of C is almost the same with the different setups while L undergoes high variation. This result can be explained by saying C is due to the depletion region of the device, which was the same for the different power supplies, while L is highly dependent of the measurement setup. This confirms the four-wire technique influences the oscillations by trying to stabilise them. The shape of the oscillations in both two-wire and four-wire measurements is very different from the one obtained using the Tektronix, and does not correspond to what we would expect from the simulations shown in Figure 3-28(a) and (b). These observations lead to the conclusion that the Keithley 2601A sourcemeter is not suitable for accurate time-dependent measurements. The results obtained using the different setups are summarised in Table 6.

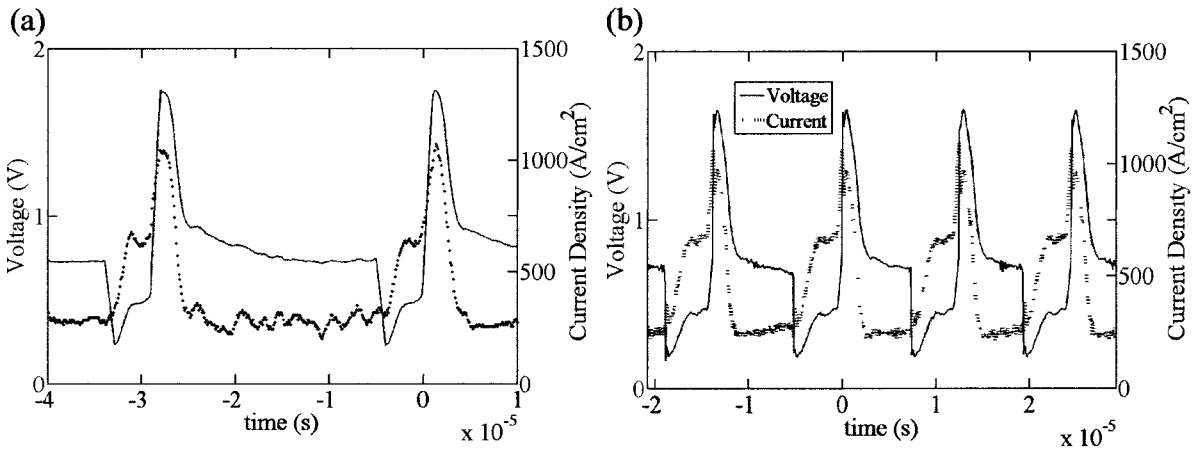

Figure 3-29: Sample of time-dependent current-density (red line) and voltage (blue line) oscillations measured over time when the system is biased inside the NDR region using (a) the Keithley 2601A sourcemeter in four-wire configuration and (b) the Keithley 2601A sourcemeter in two-wire configuration. The oscillations in voltage are displayed by the left *y*-axis and correspond to the blue line, while the oscillations in current are displayed by the right *y*-axis, corresponding to the red dotted line.

A *J-V* curve is reconstructed using the oscillations in current density and voltage measured with the Keithley 2601A sourcemeter in the two-wire configuration. Less noise is present than when the oscillations are measured with the Tektronix power supply, but an offset is observed in the excess current region and the time-dependent curve is arched in the initial slope region. No additional oscillations can be observed in the excess and thermal current region, leading to the conclusion that the Keithley 2601A sourcemeter internal feedback stabilises the oscillations, even when the two-wire measurement technique is used.

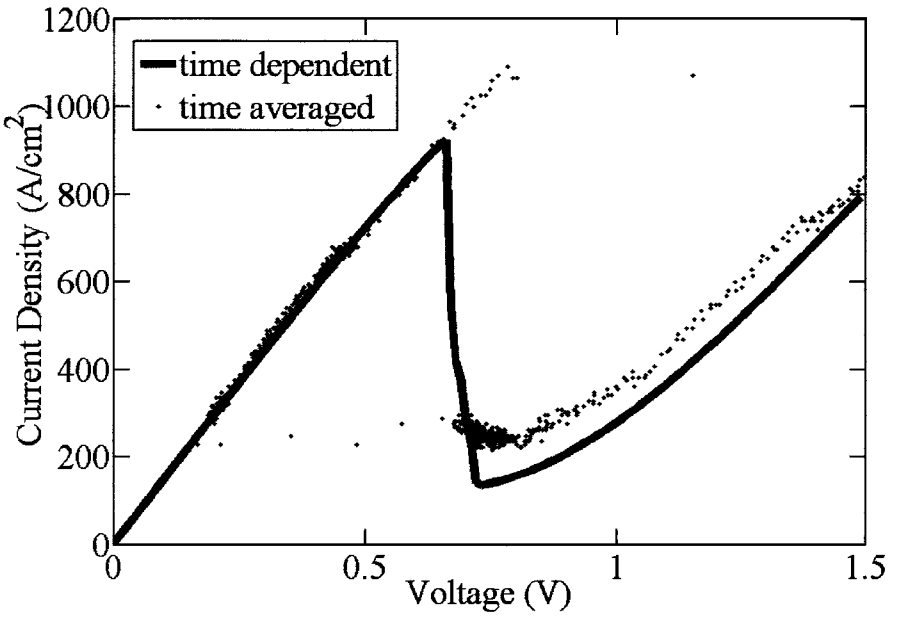

Figure 3-30: *J-V* curve of an AlGaAs/AlGaAs TJ presenting time-dependent (black dots) and time-averaged (full line) measurements performed using the Keithley 2601A sourcemeter in two-wire configuration.

Table 6: *Frequency Period L* and *C* calculated using different power supplies.

Power supply	*Frequency* (Hz)	*Period* (s)	*L* (H)	*C* (F)
Tektronix power supply	5×10^{5}-9×10^{5}	1.1×10^{-6} -1.9×10^{-6}	350×10^{-8}	3.0×10^{-9}
Keithley 2601A sourcemeter in two-wire configuration	6.7×10^{4}	1.5×10^{-5}	400×10^{-7}	3.5×10^{-9}
Keithley 2601A sourcemeter in four-wire configuration	3.3×10^{4}	3×10^{-5}	800×10^{-7}	4.0×10^{-9}

3.5-4 Conclusion

The time-dependent behavior of an AlGaAs/AlGaAs tunnel junction has been studied when biased in the NDR region. Nonlinear current density and voltage oscillations were observed using an oscilloscope. This phenomenon enabled the reconstruction of the complete TJ *J-V* curve, giving more details concerning the location of the tunneling peak current density and the valley current density. A tunneling peak of between 1050 and 1150 A/cm^2 was recorded by this method, the highest value published in the literature for a TJ. The tunneling peak current density allows us to understand the theoretical maximal current density for which a solar cell could operate using this type of tunnel junction. The origin of the oscillations can be understood by studying the equivalent circuit. Upgrading the power supply, the oscilloscope and improving the electronic isolation setup could increase the accuracy of the nonlinear oscillation measurements. This study provides a better understanding of the TJ to accurately calibrate the simulations over their full operating range and, as a result, optimise the MJ solar cell structure.

3.6 Measurements over temperature

On Earth, solar cells are subjected to different temperature conditions. At 25°C, the current density going through each sub-cell of a MJ solar cell is about 7 A/cm^2. When the temperature increases, the current density going through the solar cell also increases. For the overall MJ solar cell to have the highest possible efficiency, the TJ inside the MJ solar cells must be able to conduct the current density at different temperatures. In this section, the TJ behavior is measured at different temperatures to ensure it can still conduct the current density through a MJ solar cell. According to the theory presented in section 2.3-3, the resistance of a TJ is expected to decrease as the temperature is increased. Moreover, the tunneling peak current density and the thermal current density are expected to increase with temperature.

The measurements are first performed on sample TJ1-A, and then on sample TJ1-B. The measurements performed on TJ1-A, shown in Figure 3-31, are done at five different temperatures: 5, 25, 45, 65 and 85°C. The expected trend can be observed, meaning the peak current density increases with temperature, as summarised in Table 8. Moreover, the total resistance, determined by the inverse of the slope near the origin, decreases as the temperature increases, causing the peak voltage to decreases as well. The linear term of the total specific resistivity decreases with increasing temperature from 1.3 mΩ·cm^2 at 5°C to 0.5 mΩ·cm^2 at 85°C, corresponding to a variation of 0.8 mΩ·cm^2. The initial slope of the *J-V* curve corresponds to the sum of the TJ resistance and its mesa structure resistance. The behavior of the mesa structure resistance over temperature could not be accurately calculated because the TJ was not simulated at different temperatures, therefore, it cannot be verified that the majority of the temperature-dependent resistance is due to the isolated TJ. To evaluate the contribution of the mesa resistance to the change in the initial slope region, the *n*-TLM pads are measured over temperature, resulting in a variation in the *n*-contact resistance from 0.50 mΩ·cm^2 at 25°C to 0.43 mΩ·cm^2 at 85°C, which is small, compared to the overall resistance. Thus, the majority of the temperature-dependent resistance is due either to the isolated TJ, or to the *p*-resistance. In the previous section, the *p*-contact

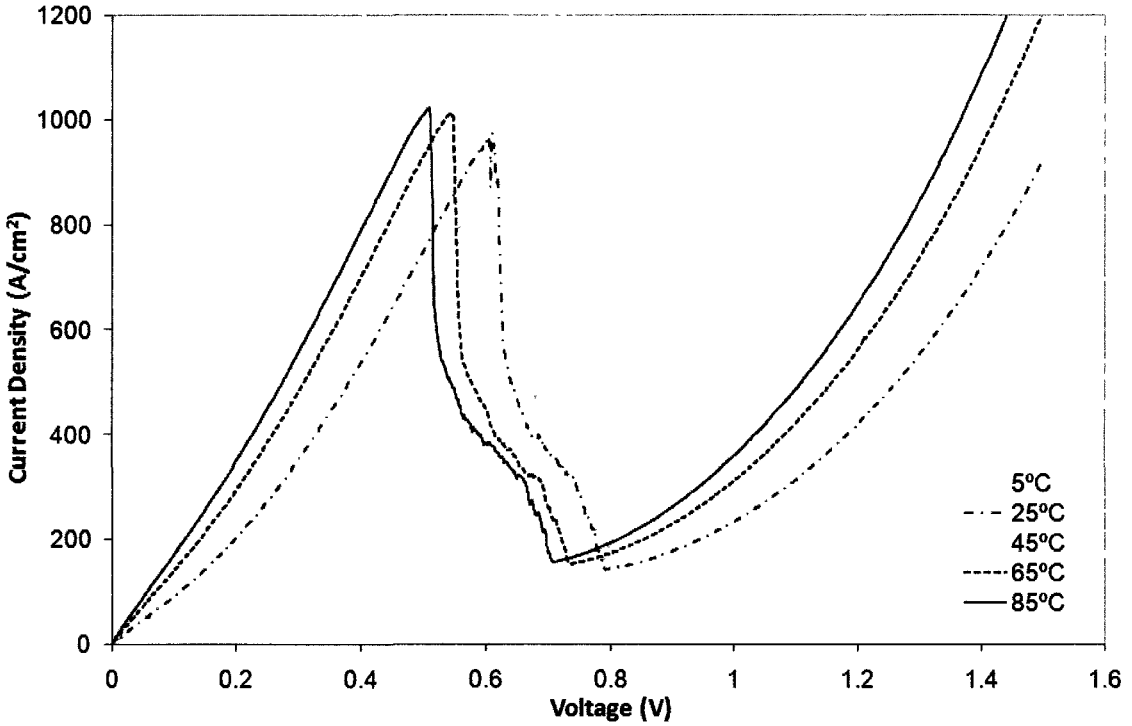

Figure 3-31: *J-V* curve of sample TJ1-A at different temperatures [45].

resistance was calculated to be ~1.05 mΩ·cm^2. For the total resistance of the TJ plus the mesa structure to decrease by 0.8 mΩ·cm^2, the *p*-contact resistance would have to decrease by ~50%. This means the temperature-dependent resistance is mostly due to the *p*-contact. The contacts being Schottky contacts, this result is in agreement with the theory presented in section 2.1-7. Furthermore, as the temperature decreases, the positive curvature in the initial slope region becomes more pronounced revealing a nonlinear increase in the resistance. The same phenomenon can be observed when the *p*-TLM pads are measured over temperature: the nonlinear terms decrease when the temperature increases. At higher temperatures, the NDR region starts at lower voltages as indicated by the shift in the plateau-like profile [45].

To verify this analysis, sample TJ1-B is measured at different temperatures: 25, 45, 65 and 85°C. As illustrated in Figure 3-32, thermal current density increases with temperature, while the initial slope region shows a slight variation of 0.09×10^{-4} Ω·cm^2 between 25 and 85°C, as summarized in Table 8. The mesa resistance is calculated using the Corbino method to be 1.1×10^{-4} Ω·cm^2 at 25°C and 1.3×10^{-4} Ω·cm^2 at 85°C, corresponding to

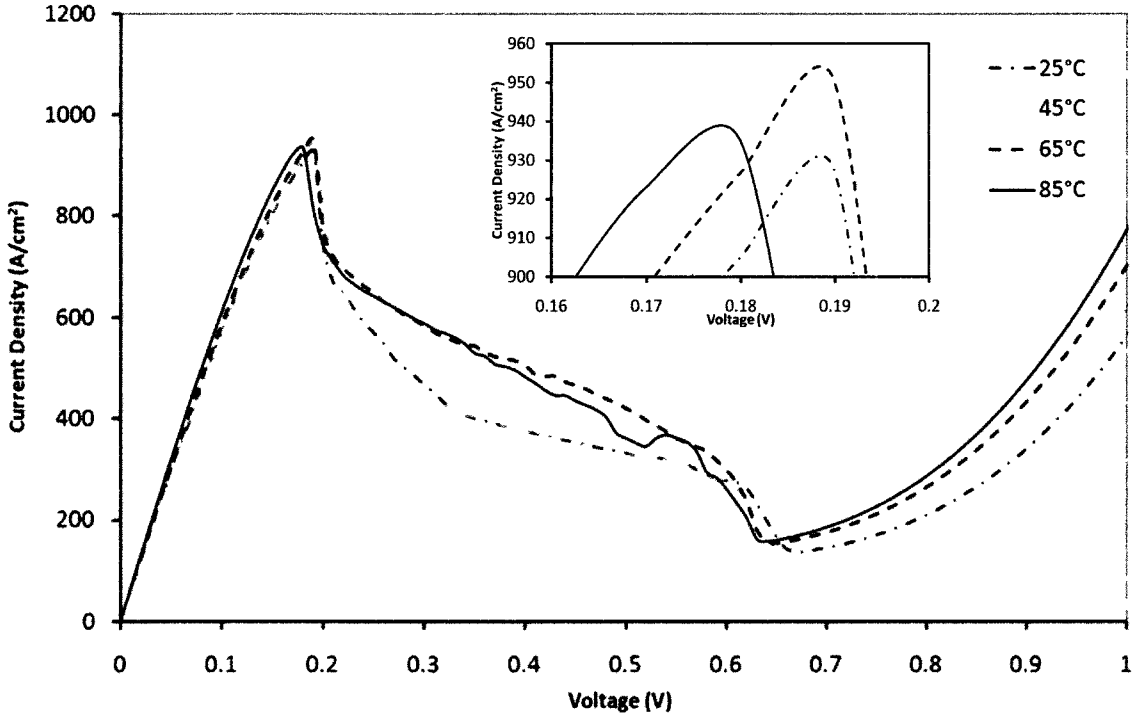

Figure 3-32: *J-V* curve of sample TJ1-B at different temperatures, including an inset highlighting the tunneling peak.

a variation of 0.2×10^{-4} $\Omega\cdot cm^2$, which is within the uncertainty on our calculations ($\pm0.2\times10^{-4}$ $\Omega\cdot cm^2$), as demonstrated in Appendix B. The tunneling peak current density increases with temperature at 25, 45 and 65°C, but its exact value is obscured by the NDR region. The curve measured at 85°C depicts the correct behavior in the initial slope and the thermal current density regions but the peak is not as high as expected. This could be due to the NDR region which obscures the exact location of the tunneling peak, as explained in the previous section.

Table 7: Position of the tunneling peak and resistance of the *J-V* curve measured on TJ1-A at different temperatures.

Temperature (°C)	Peak voltage (V)	Peak current density (A/cm^2)	Specific resistivity ($\Omega \cdot cm^2$)	Resistance (Ω)
5	0.64	960	13.1×10^{-4}	26.7
25	0.61	970	11.6×10^{-4}	23.6
45	0.55	1000	9.9×10^{-4}	20.2
65	0.54	1100	8.2×10^{-4}	16.8
85	0.51	1200	6.7×10^{-4}	13.7

Table 8: Position of the tunneling peak and resistance of the *J-V* curve measured on TJ1-B at different temperatures.

Temperature (°C)	Peak voltage (V)	Peak current density (A/cm^2)	Specific resistance ($\Omega \cdot cm^2$)	Resistance (Ω)
25	0.19	927	1.76×10^{-4}	3.59
45	0.19	941	1.75×10^{-4}	3.58
65	0.19	948	1.72×10^{-4}	3.51
85	0.18	934	1.65×10^{-4}	3.36

3.7 AlGaAs/InGaP sample

Another potential TJ design is AlGaAs/InGaP, which includes the III-V semiconductor material InGaP. InGaP is important because it is lattice matched to GaAs with 1% of In, while also having a bandgap larger than photon energies intended for lower sub-cells. This section presents measurements of an AlGaAs/InGaP sample, referred to as sample TJ2. The structure of TJ2 is depicted in Figure 3-3 (c). A picture of the sample is shown in Figure 3-33.

The measurements were done at 25.0±0.1°C, using the four-wire remote-sensing technique and the experimental setup described in section 3.1. The results are shown in Figure 3-34. The band-to-band tunneling region is difficult to identify. The tunneling peak current density is ~80 A/cm^2 and corresponds to the inflexion point on the *J-V* curve at 0.11 V, as expected from the literature [67]. The excess current density is much larger for the

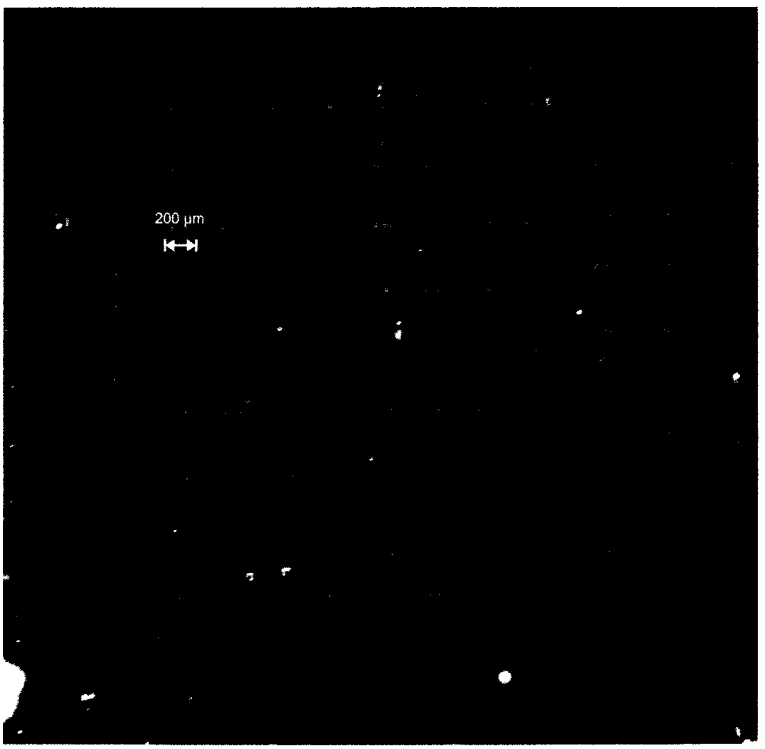

Figure 3-33: Picture displaying multiple mesas TJ from sample TJ2.

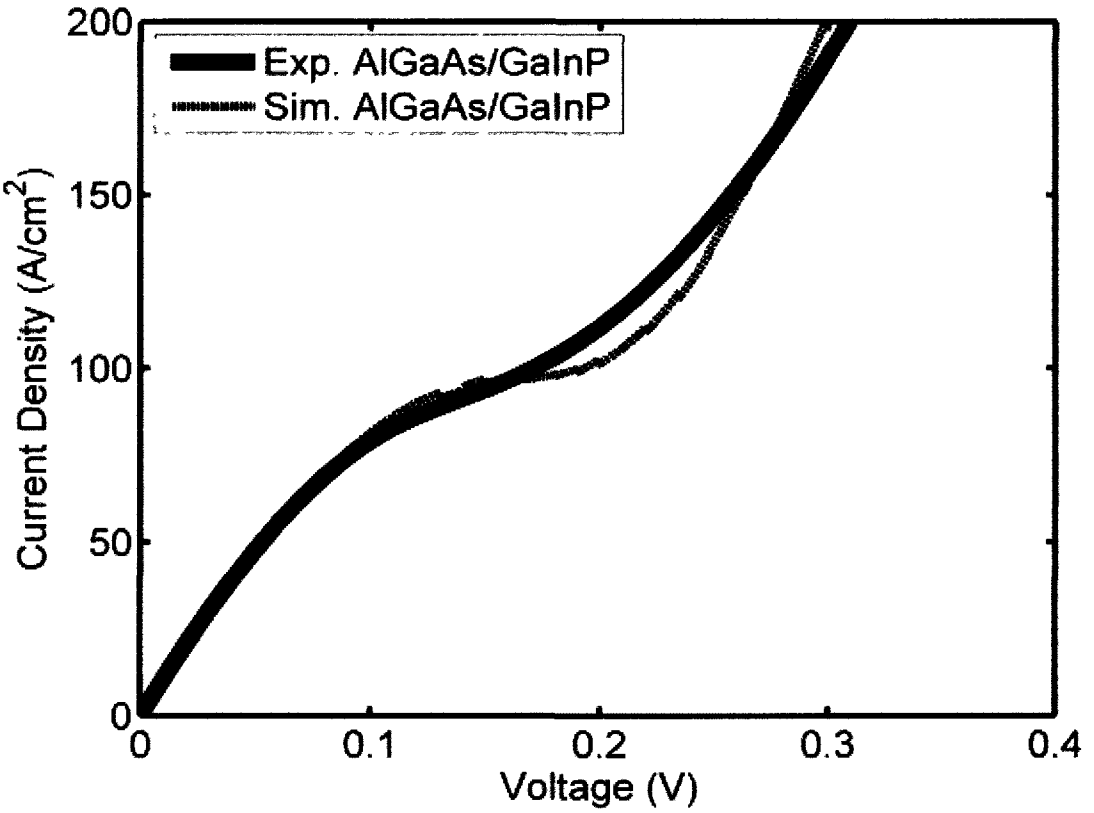

Figure 3-34: Simulated (black dashed line) and experimental (red line) *J-V* curves for the AlGaAs/InGaP TJ; the simulated curve includes numerical simulation plus analytical excess current and series resistance [19].

AlGaAs/InGaP TJ than for AlGaAs/AlGaAs TJ and dominates the *J-V* profile. As expected from Eq. (2.3.6), the tunneling peak current density of the AlGaAs/InGaP TJ with E_g~1.8 eV is much lower than the AlGaAs/AlGaAs TJ with E_g ~1.6 eV due to the differences in the bandgap. This difference in the tunneling peak current densities can be explained by studying the band structure of the AlGaAs/InGaP TJ. Both the conduction band and the valence band of AlGaAs have higher energies than those of InGaP, which decreases the built-in potential of the *p-n* junction. This reduces the depletion region which impacts strongly the tunneling region [67]. Moreover, no NDR region was observed due to a large mesa structure resistance (~9 Ω), a low tunneling peak and a high excess current density in comparison to the AlGaAs/AlGaAs TJ. Because the NDR region is quasi-inexistent, no time-dependent analysis could be performed.

Due to fabrication issues, the Corbinos were broken and the total mesa structure resistance could not be accurately determined. The TLM measurements were performed, and the total TJ mesa structure resistance was calculated to be about 19 Ω for a TJ, whereas the value used to fit the simulation to the experiment is 8.8 Ω. As demonstrated previously, the TLM pads are not accurate enough to determine the mesa structure resistance precisely, and the value they give is approximately twice the actual value. Moreover, the value used to fit the simulation to the experiment for the AlGaAs/AlGaAs TJ in section 3.4 is consistent with the value calculated using the Corbinos. Therefore, the total mesa structure resistance of the AlGaAs/InGaP can be estimated at 8.8 Ω using the simulation fit, or 4.3×10^{-4} Ω·cm^2.

In conclusion, this TJ shows a low tunneling peak current density of 80 A/cm^2, which is much lower than the tunneling peak current density obtained using an AlGaAs/AlGaAs TJ (~950 A/cm^2 using the time-averaged measurements and 1050-1150 A/cm^2 using the time-dependent measurements) due to the relative barrier height between the two materials. The NDR region is not well defined in the AlGaAs/InGaP TJ *J-V* curve, making it difficult to quantify the tunneling peak and valley current densities and voltages, and as a result, hinders the ability to calibrate the numerical model. The AlGaAs/AlGaAs TJ have a higher performance and are more suitable for the numerical model. Due to its lower tunneling peak current density in comparison to the AlGaAs/AlGaAs TJ, the resistance is higher at operating conditions of a MJ solar cell, with a value of 9.3×10^{-4} Ω·cm^2 for the AlGaAs/InGaP TJ compared to 1.4×10^{-4} Ω·cm^2 for the AlGaAs/AlGaAs TJ, thereby making it less suitable for integration in a MJ solar cell.

Chapter 4 – Solar Cell Measurements

In this section, solar cells fabricated using indium tin oxide films as a transparent top electrode to replace the front-side metallic electrode grid are studied. The measurement method used to test the efficiency of solar cells at low concentration is presented, and a section is dedicated to the calibration of the solar simulator. Three different designs are compared. In the first design, the top fingers are replaced by the ITO layer. In the second design, the ITO is deposited on top of a metallic layer and a metallic electrode grid consisting of two fingers. In the third design, the ITO layer is deposited on top of a metallic layer and a complete metallic electrode grid. The overall performance of the ITO solar cells is measured at 3 and 20 suns and compared to efficiency of a standard MJ solar cell.

4.1 ITO theory

Transparent conductive oxides (TCO) are used to fabricate optoelectronic devices. The most commonly used TCO is indium tin-oxide (ITO), which combines good electrical conductivity and high optical transparency over a wide spectral range [68]. ITO can be deposited using different methods, such as sputtering [35,69-71], evaporation [72], pulsed laser deposition [73], chemical vapor deposition and sol-gel deposition [74], but the most commonly used is magnetron sputtering. The properties of ITO are different depending on the deposition method. In this work, radio-frequency magnetron sputtering was used. ITO films deposited using this method exhibit an average transmittance of over 85% in the visible range (400-700 nm), as illustrated in Figure 4-1, and an electrical conductivity of 1000-5000 S/cm. The carrier concentration used in TCO is typically 10^{21} cm^{-3}. Because of its optical properties, an ITO layer can be used to replace the front-side grid metallic electrode, or fingers, of MJ III-V solar cells, potentially contributing to an increase of their overall

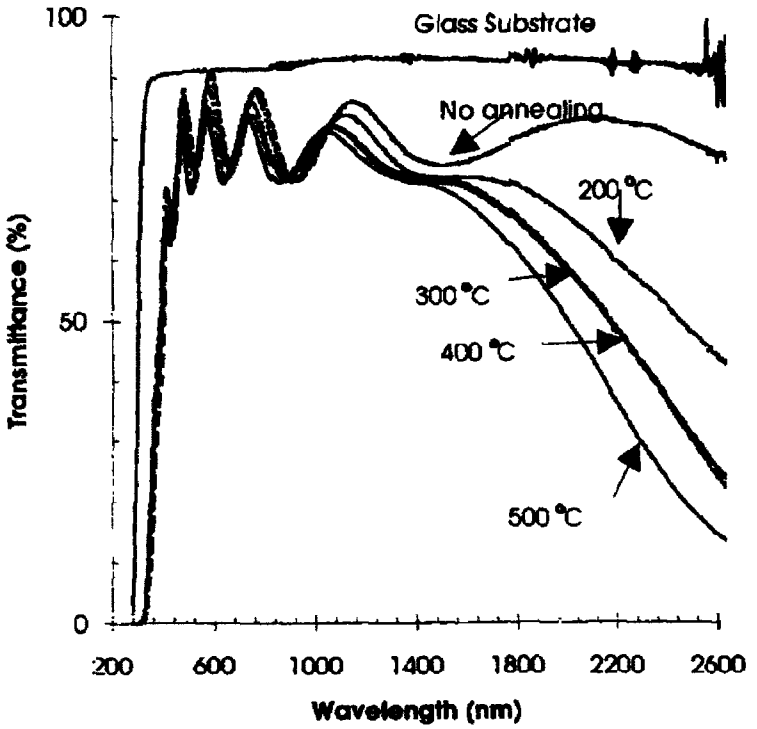

Figure 4-1: Transmittance of ITO deposited by radio frequency reactive magnetron sputtering at different annealing temperature; from Ref. [70].

performance by reducing losses due to shadowing. The ITO layer acts like a passivation layer, a layer grown at the surface of the semiconductor to tie up dangling bonds created by the interruption of the periodicity of the crystal lattice, and thus reduce the recombination rate. In the past, solar cell using ITO/Si junctions have been studied [75], and ITO is widely used in organic solar cells [76]. On MJ solar cells, ITO deposition simplifies the fabrication step and as a result, reduces the cost of solar cell fabrication. On the other hand, ITO is relatively expensive and does not have a high enough conductivity to conduct the high currents generated by concentrated photovoltaic systems. For concentrated photovoltaic use, the material must be transparent across the 300-1800 nm range [77]. ITO materials present low absorption in the UV and the infrared. It needs to have low resistance and high transparency to the wavelength absorbed by the sub-cells below, for the overall MJ solar cell to produce larger current.

4.2 Method

4.2-1 Setup

The samples are illuminated using a continuous-wave Oriel 92191 solar simulator powered by a 1600 W Ozone Free Xenon lamp model 62711. This solar simulator is capable of uniformly illuminating a solar cell and produces from 1 to 150 times the intensity of the sun over a beam of up to 5 cm × 5 cm. The Xe lamp is chosen because it has a sun-like spectrum, as shown in Figure 4-2. The solar simulator is run by a 69922 Power Supply that can vary the intensity of the lamp from 1300 to 1680 W. It also includes an electronic shutter. The output spectrum can be controlled using neutral density (ND) filters as well as air mass filters simulating both the terrestrial and extraterrestrial spectra including AM0, AM1, AM1.5G, AM1.5D and AM2. In this chapter, all the measurements are done using the AM1.5D filter. The ND filters attenuate the beam, enabling us to illuminate the solar cell with the intensity of 3 suns (ND10b filter), or the intensity of 150 suns. The solar simulator is powered by the lamp power supply shown in Figure 4-3.

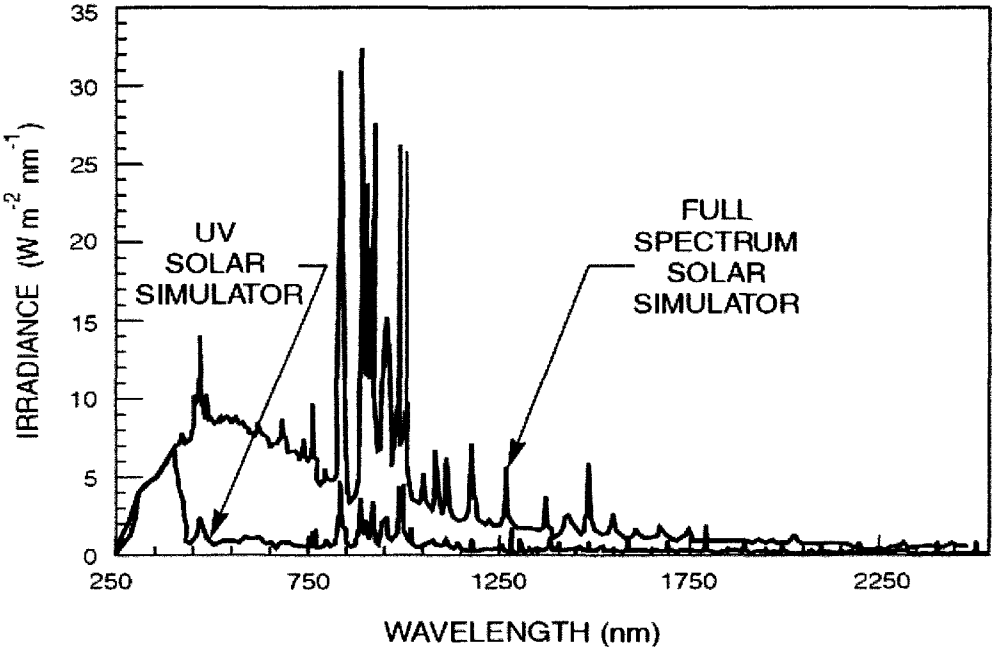

Figure 4-2: Spectral output of a full spectrum 1600 W Solar Simulator, compared to the output of a 1600 W UV Solar Simulator [78].

The Oriel solar simulator is accompanied by a photovoltaic characterization station depicted in Figure 4-4. This station includes a temperature-controlled platform consisting of an RTD and a TEC connected to a temperature-controller such that solar cells can be characterized over temperature and permitting the measurement of temperature dependant coefficients. A fan and a heat sink are used to cool down the sample. The solar cell is placed on the gold plate illustrated in Figure 4-4(b). A Keithley 2601A sourcemeter is used as a power supply to measure the *J-V* characteristics. Two alligator clips are connected to the gold plate to conduct the current through the bottom contact of the solar cell, which was deposited on the back of the solar cell as explained in Chapter 2. The top contact is made by using four probes touching the busbars on the top of the solar cell. An attenuator ND10b is placed between the output of the lamp and the sample for measurements at the intensity of ~3 suns. Finally, the solar cell is held in place using a vacuum seal. The vacuum pump, the TEC and the RTD are connected as shown in Figure 3-1 (c).

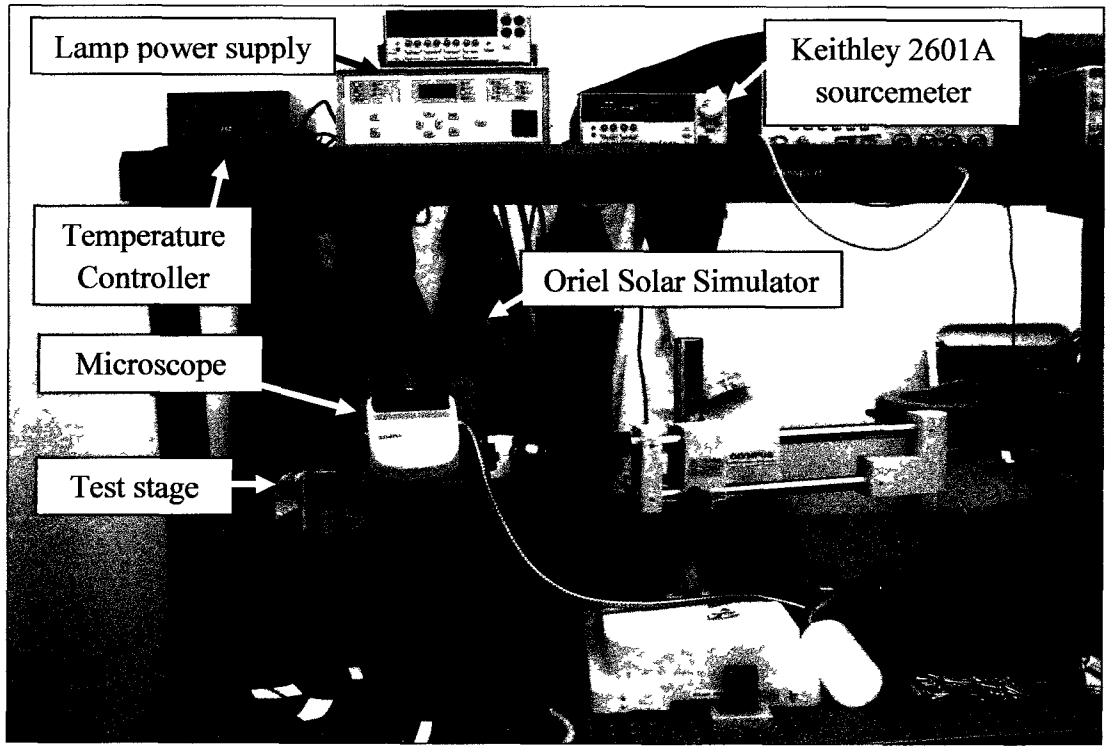

Figure 4-3: Pictures of the whole setup including the Oriel Solar Simulator temperature controller, the Keithley 2601A sourcemeter and the lamp power supply.

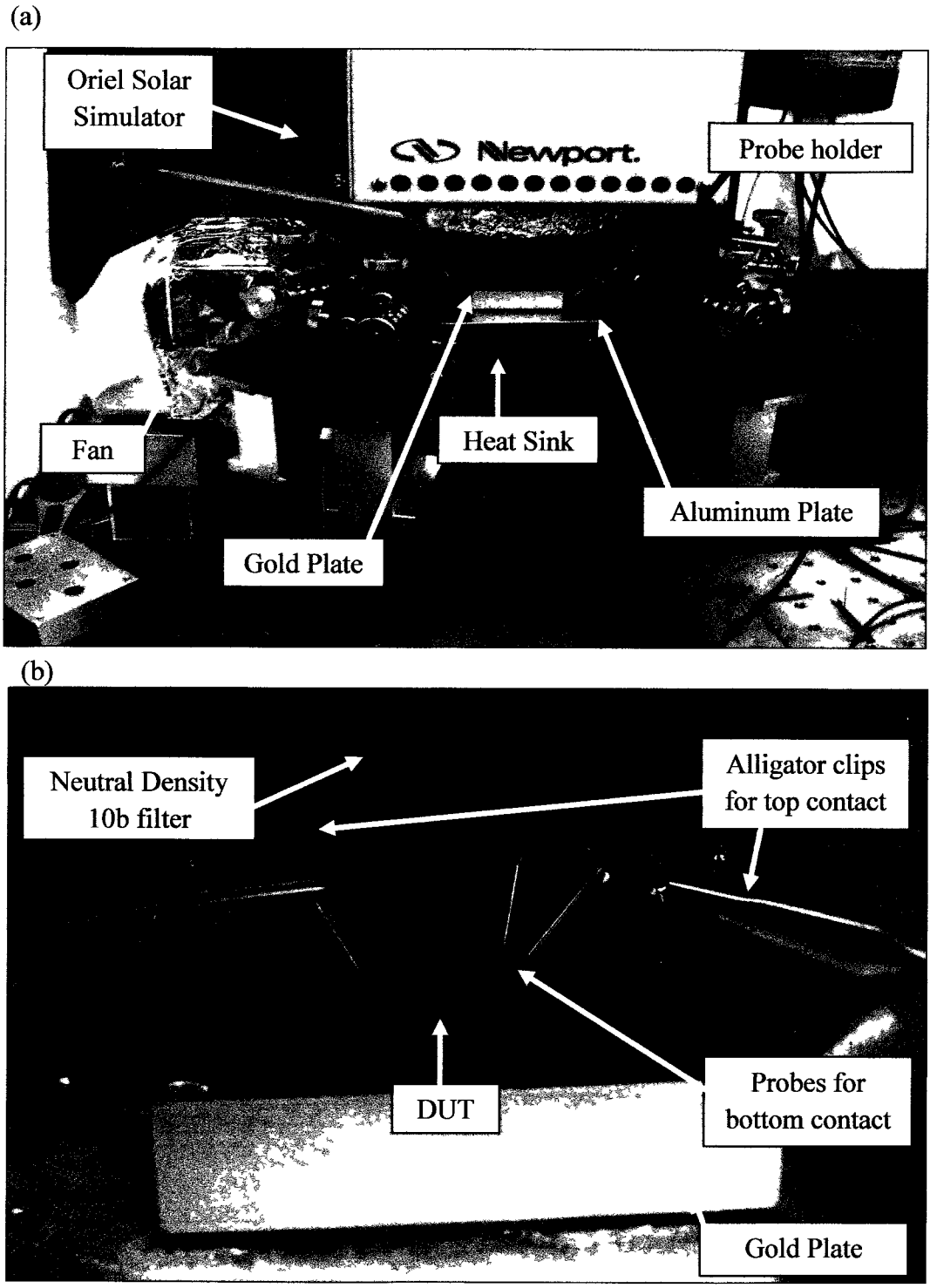

Figure 4-4: Pictures of the experimental setup presenting (a) the test stage including the probe holder and the cooling system and (b) a close-up of the gold plate and the attenuator showing the probes making contact on a sample in position over vacuum seal.

4.2-2 Calibration

The intensity of the sunlight delivered by the simulator varies on a daily basis. To determine it accurately, the system has to be calibrated. The calibration consists in two steps. First, a Si solar cell from the National Renewable Energy Laboratory (NREL), referred to as NREL calibrated cell, is measured at varying intensities between 1300 and 1680 W at 25°C with the attenuator ND10b and without attenuation. These cells are already calibrated and their J_{SC} at 1 sun is already known. J_{SC} is calculated at each value of the intensity knowing the cell area is 0.25 cm^2. By comparing the experimental J_{SC} with the given J_{SC}, the number of suns can be determined. The given value of J_{SC} is 14.3×10^{-3} A/cm^2/sun. From Eq. (4.2.1), the ratio of the experimental value of J_{SC} over the given J_{SC} gives the number of suns.

$$\frac{\exp J_{SC}}{\text{given } J_{SC}} = \#\,suns \tag{4.2.1}$$

The calculated concentration is ~3 suns with the attenuator and ~20 suns without the attenuator.

Next, a MJ solar cell fabricated by Cyrium Technologies Inc. is measured over the same intensities as the NREL cell. This new cell is referred to as the standard cell. J_{SC} is calculated knowing the cell area is 1 cm^2. For the previous step, the number of suns at these lamp powers is known. The concentration for all the new J_{SC} is known. The new J_{SC} at one sun can be calculated using Eq. (4.2.2). The value should be approximately the same for each J_{SC}.

$$J_{SC} \text{ at } 1\,\text{sun} = \frac{J_{SC}}{concentration} \tag{4.2.2}$$

This MJ solar cell becomes the new reference cell. Every day, before measuring other solar cells, the first step is repeated using the MJ solar cell. The intensity at each lamp power is then calculated by multiplying the number of suns by the intensity at one sun defined as 1000 W/m^2.

4.3 Fabrication

The samples studied in this section are InGaP/InGaAs/Ge triple-junction solar cells with lithographically-defined front-side metallic electrode. Figure 4-5 shows a schematic of a typical solar cell. The III-V materials (in our case InGaP and InGaAs) constituting the sub-cells are MOCVD grown on a Ge wafer. A window layer is deposited on the top layer to avoid surface recombination, and recovered by a passivation layer. Gold contacts are deposited on the back on the solar cell and a metallic electrode grid is deposited on the top. To maximise the absorption of the solar cell, an ARC is added on the top of the solar cell, covering the aperture area between the fingers of the top grid electrode. This method is used to fabricate the MJ solar cell used as a reference cell.

The three different designs of ITO solar cells depicted in Figure 4-7 are studied in this chapter. In the first design, design A, as shown in Figure 4-7(a), the top metallic electrode is removed by wet-etching and replaced by an ITO layer, and deposited on the top sub-cell of the MJ solar cell. Therefore, no fingers are present, as shown in Figure 4-6. Metallic frontside electrodes, or busbars, of thickness 175 nm, are deposited by evaporation and lift-off onto the ITO layer. Two samples are fabricated using design A, the first one without any passivation layer, while the surface of the top sub-cell of the second sample was

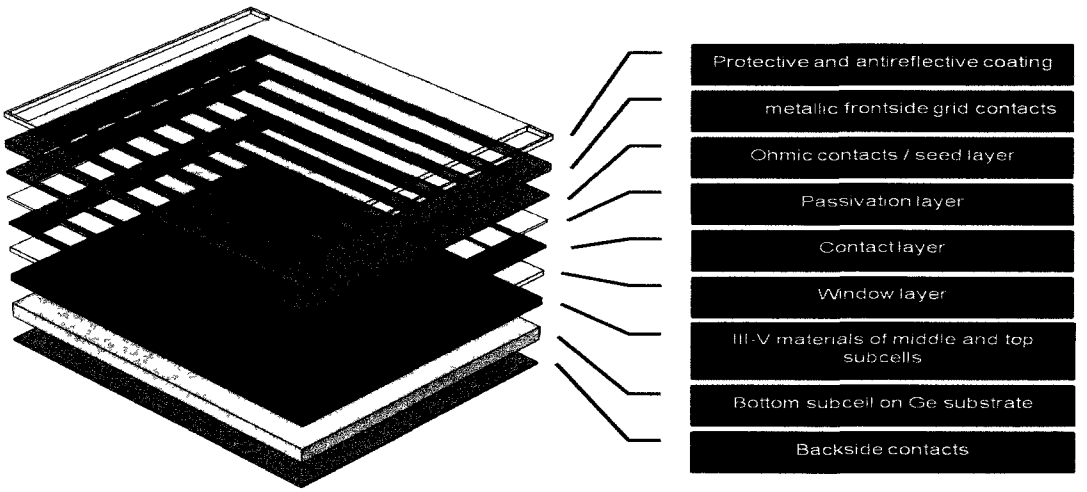

Figure 4-5: Typical design of a multi-junction solar cell. [Courtesy of Artur Turala, Université de Sherbrooke]

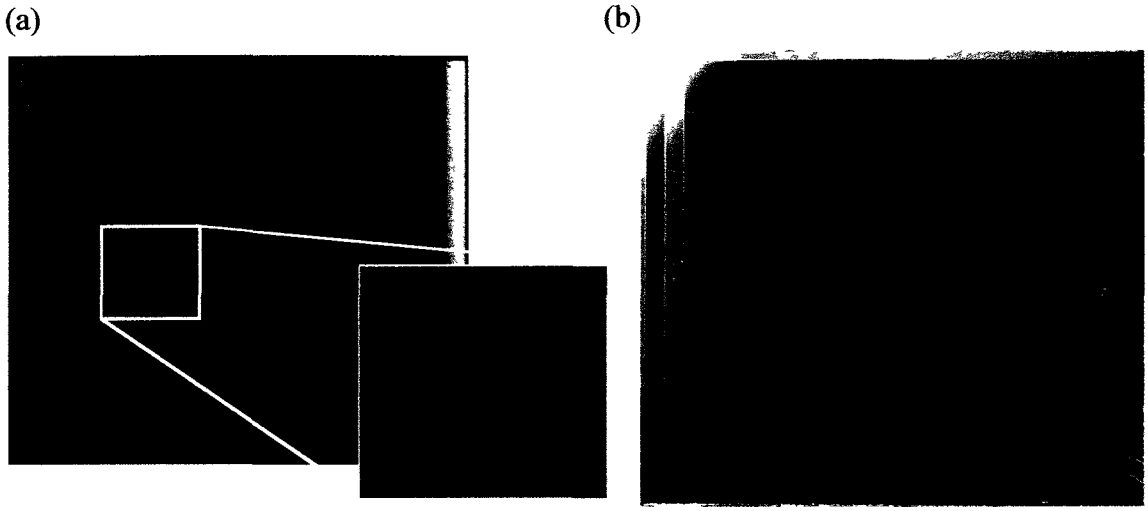

Figure 4-6: Picture of (a) a typical solar cell with a metallic electrode grid deposited on the top and (b) an ITO solar cell with no metallic electrode grid on the top. [Courtesy of Artur Turala, Université de Sherbrooke]

chemically passivated before ITO deposition (sample ITO-A1 and ITO-A2 respectively). In this design, there are no fingers on the top of the cell while the busbars are still present to provide electrical contact. In the design B (sample ITO-B1), illustrated in Figure 4-7(b), the ITO layer is placed between two metallic layers: the frontside contacts (175 nm) and another layer of metallic contacts (160 nm) containing only two fingers. The contact layer was etched away in self-aligned process using the metallic electrode layer as a mask. A layer of InGaAs in used as an encapsulation layer. The third design, referred to as design C and presented in Figure 4-7(c) is similar to design B, but the metallic layer deposited under the ITO layer is replaced by a metallic grid electrode of pitch 120 μm deposited by evaporation and lift-off. Three samples are fabricated using this design, one covered at 100% by the fingers (sample ITO-C1), the second one covered at 90% (sample ITO-C2) and the third one covered at 40% by the metallic grid electrode (sample ITO-C3). The fingers are present in this last design to increases the conductivity. The samples were annealed at 350°C for 5 min. For all the samples, the thickness of the ITO layer is 160 nm and its conductivity is 3050 $(\Omega \cdot cm)^{-1}$. The average optical transmission is 86.6%. The refractive index of the ITO layer varies with its thickness. At the interface with the III-V semiconductors, its value is 1.6 and on the surface it is 2.

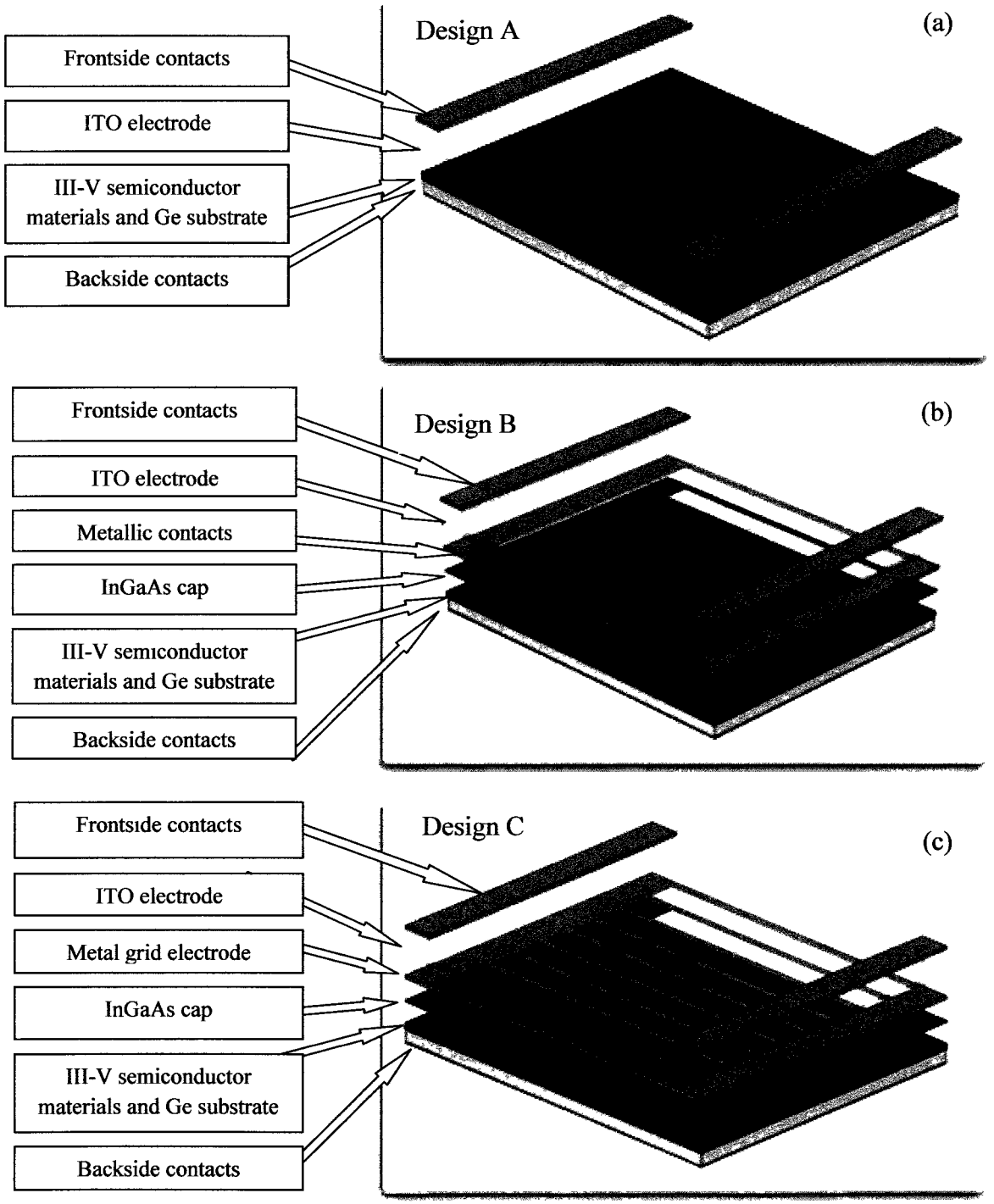

Figure 4-7: Three different ITO designs consisting of (a) an ITO electrode under one metallic layer; (b) an ITO electrode between two metallic layers and (c) an ITO electrode between two metallic layers with metallic fingers. [Courtesy of Artur Turala, Université de Sherbrooke]

4.4 Results and Discussion

All the samples are first measured at 1680 W, with the attenuator ND10b (~3suns) at 25°C. V_{OC} and J_{SC} are measured, and their *FF* and efficiencies are compared to determine the best design. All these parameters are listed in Table 9. First, the effect of passivation is studied. The two samples fabricated using design A, ITO-A1 and A2, are measured at 1680 W, at 25°C and compared in Figure 4-8. Sample ITO-A2, which was chemically passivated has a lower *FF* but a higher efficiency than sample ITO-A1. Thus, the passivation layer increases the efficiency of a solar cell, even though it decreases the squareness of its *J-V* curve. Samples ITO-B1 C1 C2 and C3, fabricated using designs B and C, are then compared to study the effect of the fingers on the efficiency of a solar cell, as illustrated in Figure 4-9. The efficiency increases with the percentage of covering of the solar cell by the fingers. ITO-C1, the sample 100% covered with the electrode grid gives the best efficiency with a value of 22.9%, whereas ITO-B1, the sample with only two fingers gives the lowest efficiency, with a value of 19.4%. The fingers increase the conductivity. Even though they also increase the shadowing, they still contribute to increasing the efficiency of an ITO solar cell.

Table 9: V_{OC}, J_{SC}, *FF* and efficiency of the ITO solar cells at 3 suns illumination.

	V_{OC} (V)	J_{SC} (A/cm^2)	P_{MAX} (W)	*FF* (%)	η (%)
ITO-A1	2.48	2.88×10^{-2}	4.79×10^{-2}	67.0	15.1
ITO-A2	2.21	4.19×10^{-2}	5.85×10^{-2}	63.1	18.4
ITO-B1	2.53	3.55×10^{-2}	6.16×10^{-2}	68.5	19.4
ITO-C1	2.55	3.51×10^{-2}	7.28×10^{-2}	81.4	22.9
ITO-C2	2.53	3.34×10^{-2}	6.77×10^{-2}	80.2	21.3
ITO-C3	2.52	3.41×10^{-2}	6.29×10^{-2}	73.3	19.8
Reference Cell	2.69	4.36×10^{-2}	8.39×10^{-2}	83.9	39.7

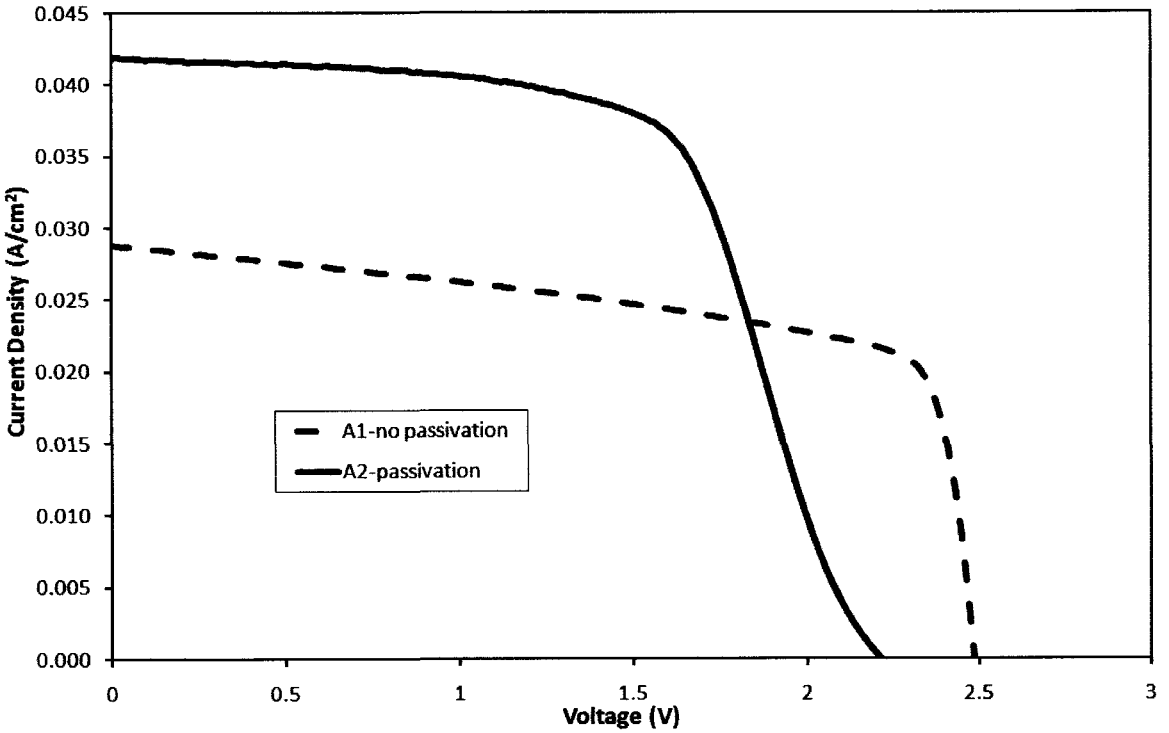

Figure 4-8: *J-V* comparison between a chemically passivated sample (full line) and a sample with no passivation (dashed line).

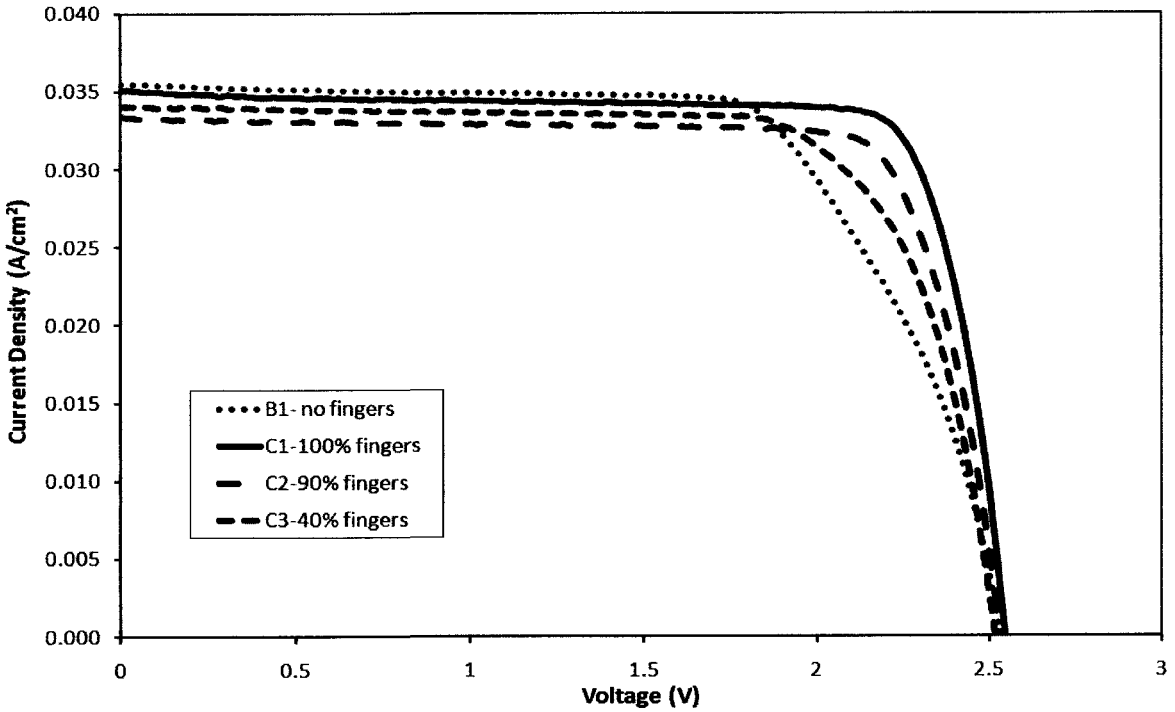

Figure 4-9: *J-V* curves of ITO solar cells covered with fingers (blue, green and orange line) without fingers (red line).

All the measurements are summarised in Figure 4-10 and compared to the reference cell. Overall, ITO-C1 gives the highest efficiency and the highest *FF* of the ITO solar cell. Its efficiency is still 50% lower than the reference cell value, which has an efficiency of 39.7%. This difference could be largely due to the absence of ARC deposited on the ITO solar cell. The next step will be to add an ARC onto these ITO solar cells and compare the results to the reference cell.

The measurements are repeated at 20 suns to observe the impact of a change in illumination on the samples, and the results are listed in Table 10. Once again, when ITO-A1 and A2 are compared, ITO-A2 shows a higher efficiency, meaning the passivation of the top sub-cell increases the efficiency of the overall solar cell. ITO-C1, the sample covered at 100% with fingers gives the highest efficiency with a value of 21.7%. Moreover, the efficiencies of all the samples decrease by ~1% when the illumination changes from 3 and 20 suns. V_{OC} and J_{SC} increase at higher intensity, while the *FF* decreases between 3 and 20 suns.

The sample giving the highest efficiency of 22.9% at 3 suns and 21.7% at 20 suns is ITO-C1. This sample was measured at five different lamp powers, ranging from 1300 to 1680 W at both 3 and 20 suns. The results are depicted in Figure 4-11. As expected from the theory presented in section 2.2-3, J_{SC} increases with the lamp power while V_{OC} slightly decreases.

Next, a SiO2 layer of refractive index 1.5-1.52 at 632.8 nm was deposited on the ITO layer of those cells to act as an ARC. The same measurements were performed at 3 and 20 suns and summarised in Table 11 and 12. The same way as without the ARC, the cell giving the highest efficiency is ITO-C1, with an efficiency of 25.1% at 3 suns and 26.1% at 20 suns, 5% higher than the efficiencies measured without ARC. The cell giving the lowest efficiency is ITO-A1 with a value of 18.4% at 3 suns and 18.1% at 20 suns, 3-4% higher the values obtained without the ARC. Figure 4-12 shows a comparison between the *J-V* curves measured with and without the ARC. These values are now ~40% lower than the efficiency of the standard MJ solar cell. J_{SC} is higher with the ARC, as we would expect.

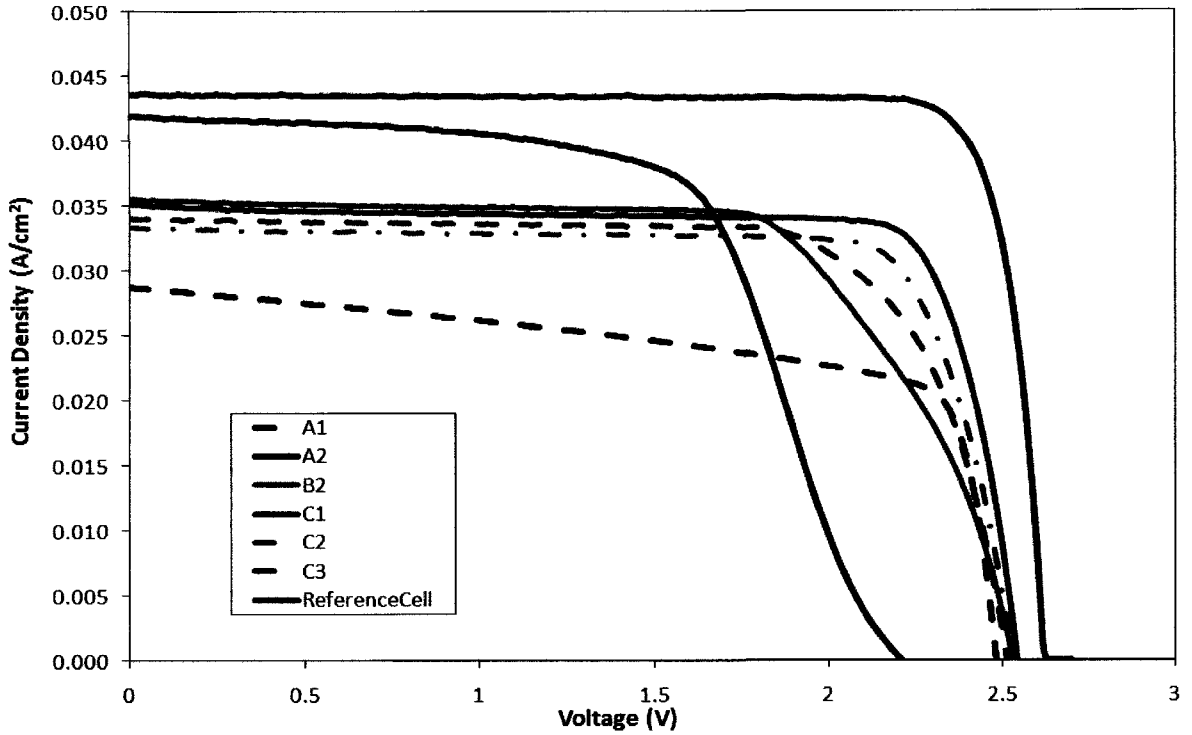

Figure 4-10: *J-V* curve of the ITO samples at 3 suns at 25°C.

Table 10: V_{OC}, J_{SC}, *FF* and efficiency of the ITO solar cells at 20 suns illumination.

	V_{OC} (V)	J_{SC} (A/cm^2)	P_{MAX} (W)	*FF* (%)	η (%)
ITO-A1	2.66	1.87×10^{-1}	3.18×10^{-1}	64.1	14.5
ITO-A2	2.39	2.72×10^{-1}	3.81×10^{-1}	58.5	17.3
ITO-B1	2.71	2.30×10^{-1}	3.68×10^{-1}	59.1	16.7
ITO-C1	2.75	2.19×10^{-1}	4.76×10^{-1}	78.9	21.7
ITO-C2	2.74	2.19×10^{-1}	4.54×10^{-1}	75.5	20.7
ITO-C3	2.72	2.25×10^{-1}	3.85×10^{-1}	62.8	17.5
Reference Cell	2.88	3.01×10^{-1}	7.45×10^{-1}	86.1	39.7

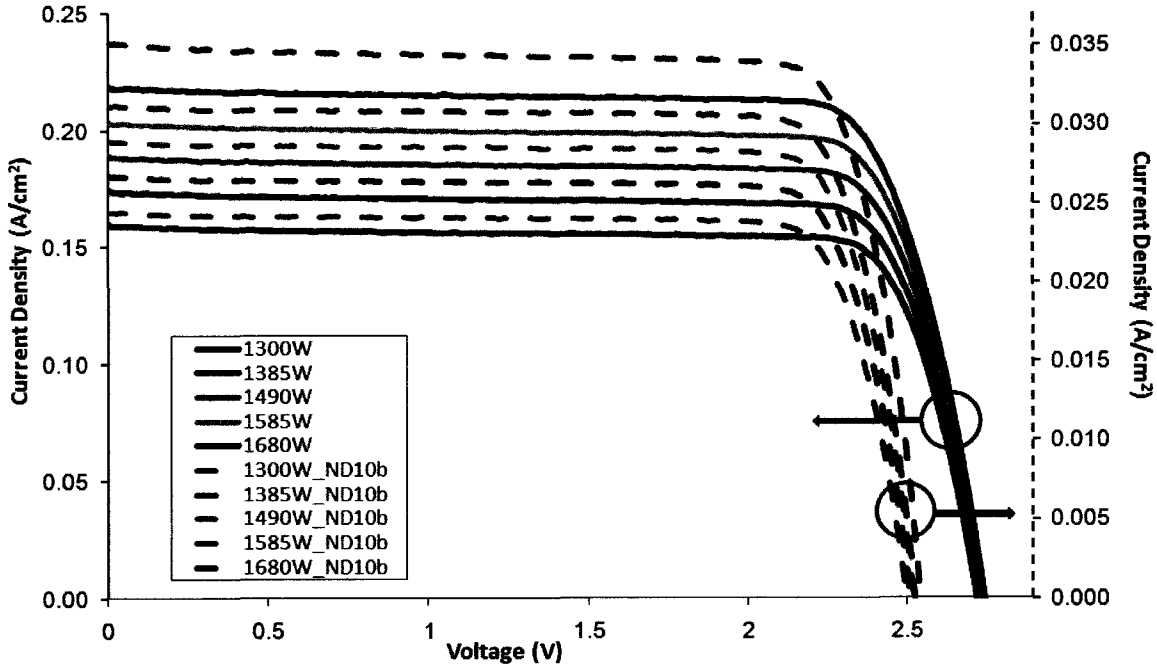

Figure 4-11: *J-V* curve of an ITO solar cell at five different lamp powers varying between 1300W and 1680W at 3 suns and at 20 suns. The measurements at 3 suns are displayed by the right *y*-axis, corresponding to the dashed lines, while the measurements at 20 suns are displayed by the left *y*-axis, corresponding to the full lines.

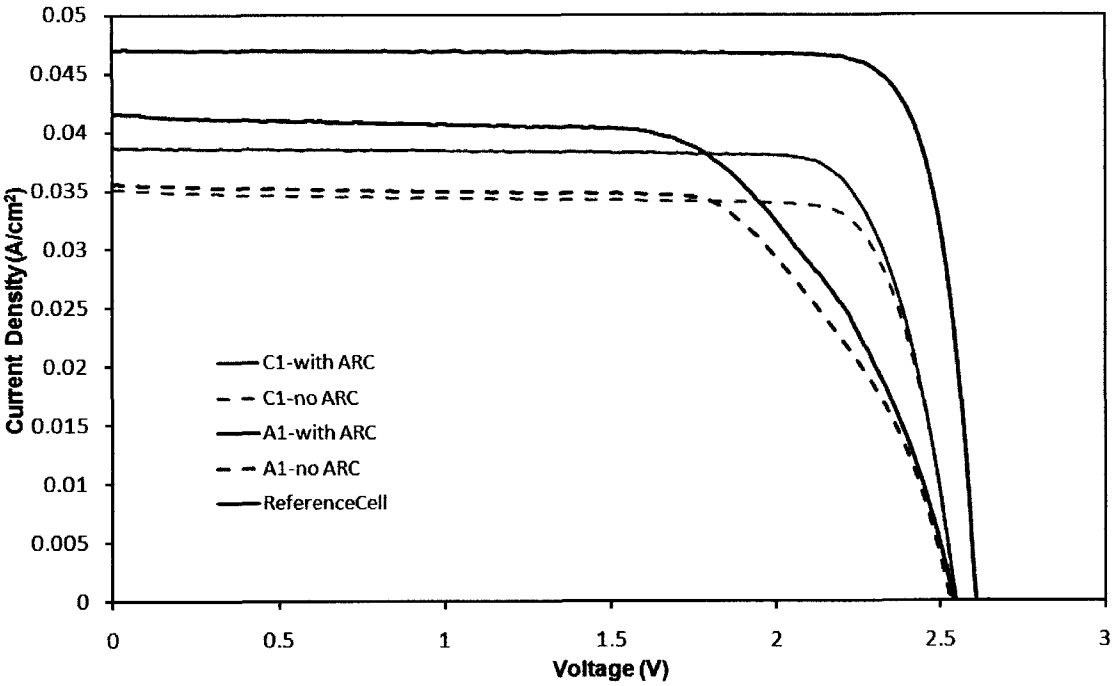

Figure 4-12: *J-V* curves of sample A1 (red line) and C1 (blue line) measured with the ARC (full line) and without the ARC (dashed line) at 3 suns.

Table 11: V_{OC}, J_{SC}, *FF* and efficiency of the ITO solar cells at 3 suns illumination.

	V_{OC} (V)	J_{SC} (A/cm^2)	P_{MAX} (W)	*FF* (%)	η (%)
ITO-A1	2.49	3.49×10^{-2}	5.85×10^{-2}	67.4	18.4
ITO-A2	2.27	4.94×10^{-2}	7.38×10^{-2}	66.2	23.2
ITO-B1	2.54	4.15×10^{-2}	6.83×10^{-2}	64.7	21.5
ITO-C1	2.55	3.87×10^{-2}	7.97×10^{-2}	80.8	25.1
ITO-C2	2.56	3.99×10^{-2}	7.60×10^{-2}	74.4	23.9
ITO-C3	2.55	3.95×10^{-2}	7.57×10^{-2}	75.0	23.8
Reference Cell	2.69	4.36×10^{-2}	8.39×10^{-2}	83.9	39.7

Table 12: V_{OC}, J_{SC}, *FF* and efficiency of the ITO solar cells at 20 suns illumination.

	V_{OC} (V)	J_{SC} (A/cm^2)	P_{MAX} (W)	*FF* (%)	η (%)
ITO-A1	2.67	2.38×10^{-1}	3.98×10^{-1}	62.6	18.1
ITO-A2	2.42	3.42×10^{-1}	4.74×10^{-1}	57.4	21.6
ITO-B1	2.73	2.79×10^{-1}	3.73×10^{-1}	53.9	18.6
ITO-C1	2.76	2.66×10^{-1}	5.73×10^{-1}	77.8	26.1
ITO-C2	2.76	2.69×10^{-1}	5.70×10^{-1}	77.1	26.0
ITO-C3	2.74	2.74×10^{-1}	4.64×10^{-1}	61.8	21.1
Reference Cell	2.88	3.01×10^{-1}	7.45×10^{-1}	86.1	39.7

4.5 Conclusion

The preliminary results show that the ITO samples reduce considerably the fabrication steps, which could result in a reduction of the cost of the solar cell fabrication. The ITO solar cells presented here can reach an efficiency of up to 22.9% at 3 suns and 21.7% at 20 suns. Chemically passivating the top sub-cell of the MJ solar cell increases the efficiency, but adding fingers improves considerably the conductivity and the efficiency of the ITO solar cell, even though it also increases the shadowing. The best of the three designs listed previously is the third design, design C, in which an electrode grid is added under the ITO layer. The efficiency of ITO sample is still 50% lower than the efficiency of a standard MJ solar cell, but their efficiency can be improved by adding an ARC on the ITO solar cells, thereby increasing their absorption. When an ARC is added, the efficiency of the solar cells is increased by 3-5% to a maximum of 25.1% at 3 suns and 26.1% at 20 suns, only ~40% lower efficiency than the standard MJ solar cell.

Chapter 5 – Conclusion and Future Work

State of the art MJ solar cells can reach high efficiencies up to 41%. They consist of three monolithically stacked *p-n* junctions connected in series by TJ. TJ are critical to conduct current through a MJ solar cell. To ensure they are able to support the amount of current going through a solar cell, their *J-V* behavior was studied. The theoretical maximal current density for which a solar cell could operate using one type of TJ is given by its tunneling peak current density value. For the first time according to the literature, AlGaAs/AlGaAs TJ were studied. These materials were chosen because their energy gap can be changed and still be lattice matched to GaAs.

Two TJ sets of samples fabricated using AlGaAs/AlGaAs were measured at 25°C using time-averaged measurements. These samples have internal resistances called mesa structure resistances due to fabrication that do not appear in the full MJ solar cell. To determine those resistances, two methods can be used: the TLM pads and the Corbino methods. On the first sample, the Corbinos were broken and the *J-V* curve depicted a nonlinear behavior due to the mesa structure resistance. A calculation method was developed in order to accurately determine the mesa structure specific resistivity value to be 1.08 $m\Omega \cdot cm^2$. On the second sample, the nonlinearity of the *J-V* curve was due to the TJ only. Both Corbinos and TLM pads were available, allowing the use of both techniques. The Corbino method was determined to be the most accurate, giving a value of 0.11 $m\Omega \cdot cm^2$. The *J-V* curves of the TJ were measured at different temperatures, verifying that it can still conduct the current density going through a solar cell at different temperatures. This study shows the resistance of the sample to decrease as the temperature increases, as expected by theory.

When the time-averaged measurement method is used, the exact location of the tunneling peak, the valley current density, and the exact shape of the curve in the NDR

region of the *J-V* curve are obscured due to nonlinear oscillations in the NDR region. The exact location of the tunneling peak is important as it provides a maximum current density at which the full MJ solar cell will operate. Moreover, in order for properly model calibration for specific design, the full TJ *J-V* curve is required to obtain the maximum tunneling peak current density. A time-dependent analysis was performed on an AlGaAs/AlGaAs TJ when biased in the NDR region. Nonlinear oscillations in current density and voltage were measured using an oscilloscope and plotted against each other, providing us with a more complete *J-V* curve, and a more accurate tunneling peak current density value. A better understanding of the TJ behavior was gained, helping us to calibrate accurate numerical models. The maximum value obtained was between 1050 and 1150 A/cm^2, the highest value ever reported in the literature for a TJ. The previous record was measured on an AlGaAs/InGaP TJ to be 80 A/cm^2 [67], attesting to the excellent quality of the TJ design and fabrication process.

For comparison, an AlGaAs/InGaP TJ was measured, showing a tunneling peak current density of 80 A/cm^2 and a higher specific resistivity with a value of 9.3×10^{-4} Ω·cm^2 for the AlGaAs/InGaP TJ compared to 1.4×10^{-4} Ω·cm^2 for the AlGaAs/AlGaAs TJ at the operating point of a MJ solar cell, thereby making it less suitable than the AlGaAs/AlGaAs TJ. This high resistance is due to the relative barrier height between the two materials. Whereas the energy gap was 1.6 eV for AlGaAs/AlGaAs, AlGaAs/InGaP has an energy gap of 1.8 eV. Thus, the AlGaAs/InGaP TJ can conduct less current at a given voltage. Furthermore, the height of the tunneling peak is highly dependent on the energy gap. According to theory, a material with a higher energy gap will have a lower tunneling peak current density. Thus, the difference in the tunneling peak current densities was expected.

The measurements still do not provide us with the exact values of the tunneling peak, the valley current densities and voltage. We estimate the variation on our measurement to be ~9%. This could be improved by getting a more precise power supply, which would enable the use a higher series resistance and reduce the noise in the measurements. A more sensitive oscilloscope would also allow us to get more accurate values. The exact location of the

tunneling peak will allow us to optimise the MJ solar cell structure as the models are then more accurately calibrated.

As the development of MJ solar cell progresses, both experimental and theoretical studies of various TJ designs must be performed to perfect optimal design in term of series resistance and tunneling peak. Material systems, thickness and dopants studies are required for a complete understanding of the TJ properties. In the short term, GaAs/GaAs and AlGaAs/GaAs TJ could be studied and compared to the AlGaAs/AlGaAs TJ. The differences in fabrication are an area of high interest. For example, during fabrication, if the sample is not rotated, the thickness could potentially change. The effect of the thickness of the devices on the TJ performance should be analysed. TJ fabricated using quaternary materials could be developed and compared as they can allow larger flexibility and bandgap offset designs.

MJ solar cells are now becoming widely available commercially. To study cost reduction strategy, a solar cell with a transparent electrode covering the surface of the top sub-cell was developed. ITO solar cells fabricated using three different designs were studied to determine the one giving the highest efficiency. The design consisting of an ITO layer deposited on top of the top sub-cell and a metallic layer and recovered by a complete electrode grid has proved to be the most efficient, with a value of 22.9% at 3 suns and 21.7% at 20 suns. An ARC increases the absorption of the ITO solar cells and thereby their overall efficiency by ~3-5%. ITO cells are promising, but their efficiencies are still ~40% lower than that of standard MJ solar cells. They could potentially be improved by further material and process development. Finding a material more transparent especially in the infrared would increase the efficiency of the ITO cells by as much as 5%. In order for these samples to be as performing as ones with regular grid line processing, a transparent electrode having an increased conductivity must be developed.

Appendix A - Derivation of the correction factor

In this appendix, the correction factor used to linearise the graph of the total resistance of the Corbinos as a function of the spacing between the contacts is derived. Starting with the expression of the total resistance and using the geometry of the Corbinos, a Taylor expansion can be applied. The correction factor can be extracted from the resulting expression.

The total resistance of a Corbino is given by

$$R_T = \frac{R_S}{2\pi}\left[\ln\left(\frac{r_2}{r_2 - s}\right) + L_t\left(\frac{1}{r_2 - s} + \frac{1}{r_2}\right)\right], \tag{A.1}$$

where R_S is the sheet resistance and L_t is the transfer length. The transfer length is the distance between the semiconductor and the metal over which most of the current transfers [79].

We want to change the previous expression into a linear relation of the form

$$R_T = \left[\frac{R_S}{W}s + 2R_C\right]c, \tag{A.2}$$

where c is a correction factor and the contact resistance is

$$R_C = \frac{R_S L_t}{W}. \tag{A.3}$$

In Eq. (A.1), we can make the following assumption [55]

$$r_2 = r_1 + s. \tag{A.4}$$

Replacing r_2 in Eq. (A.1) and simplifying gives

$$R_T = \frac{R_S}{2\pi}\left[\ln\left(\frac{r_1+s}{r_1}\right)+L_t\left(\frac{1}{r_1}+\frac{1}{r_1+s}\right)\right]. \tag{A.5}$$

The logarithmic term can be approximated using the following Taylor expansion

$$\ln\left(\frac{r_1+s}{r_1}\right)=\ln\left(1+\frac{s}{r_1}\right)\approx\frac{s}{r_1}+O\left(\left(\frac{s}{r_1}\right)^2\right). \tag{A.6}$$

Putting back in Eq. (A.5) gives

$$R_T = \frac{R_S}{2\pi}\left[\frac{s}{r_1}+O\left(\left(\frac{s}{r_1}\right)^2\right)+L_t\left(\frac{1}{r_1}+\frac{1}{r_1+s}\right)\right], \tag{A.7}$$

which can be rewritten using a correction factor c

$$R_T = \frac{R_S}{2\pi}\left[\frac{s}{r_1}+L_t\left(\frac{1}{r_1}+\frac{1}{r_1+s}\right)\right]c. \tag{A.8}$$

Simplifying gives

$$R_T = \frac{R_S}{2\pi}\left[\frac{s}{r_1}+L_t\frac{1}{r_1}\left(1+\frac{r_1}{r_1+s}\right)\right]c, \tag{A.9}$$

$$R_T = \frac{R_s}{2\pi r_1}\left[s+L_t\left(1+\frac{r_1}{r_1+s}\right)\right]c, \tag{A.10}$$

and using $r_1 >> s$ [55]

$$R_T = \frac{R_S}{2\pi r_1}\left[s+2L_t\right]c. \tag{A.11}$$

This gives a linear expression of the form of Eq. (A.2)

$$R_T = \left[s\frac{R_S}{2\pi r_1} + 2L_t \frac{R_S}{2\pi r_1} \right] c . \tag{A.12}$$

Replacing Eq. (A.3) in Eq. (A.12) gives

$$R_T = \left[\frac{R_S}{2\pi r_1} s + 2R_C \right] c . \tag{A.13}$$

Comparing Eq. (A.13) with Eq. (A.2) gives $W = 2\pi r_1$.

Thus

$$R_T = \frac{R_S}{2\pi}\left[\ln\left(\frac{r_1 + s}{r_1} \right) + L_t \left(\frac{1}{r_1} + \frac{1}{r_1 + s} \right) \right] = \frac{R_S}{2\pi r_1}\left[s + 2L_t \right] c . \tag{A.14}$$

We now need to find an expression for c.

The assumption $s >> L_t$ can be made, and Eq. (A.14) becomes

$$\frac{R_S}{2\pi}\left[\ln\left(\frac{r_1 + s}{r_1} \right) \right] = s\frac{R_S}{2\pi r_1} c . \tag{A.15}$$

Simplifying gives

$$\ln\left(\frac{r_1 + s}{r_1} \right) = \frac{s}{r_1} c . \tag{A.16}$$

Hence

$$c = \frac{r_1}{s} \ln\left(\frac{r_1 + s}{r_1} \right). \tag{A.17}$$

Appendix B - Uncertainty on the measurements

The purpose of this appendix is to evaluate the uncertainty on the measurements performed in this project. First, the precision of the equipments is given and the uncertainty on the *I-V* measurements is estimated. Then the details of the mesa structure resistance uncertainty calculations are given.

1- Uncertainty on the equipment

Table 13: Uncertainties on the measurements.

Keithley 2601 sourcemeter		Range	Error
	Voltage	1.00000V	±0.02% + 400 μV
	Current	10.0000 mA	±0.03% + 6 μA
		100.000 mA	±0.03% + 30 μA
Lamp power supply			±0.5 W
Oscilloscope			
	Voltage		±80 mV
	time		$\pm 150\times10^{-6}$ μs
Microscope			±0.0040 μm/pixel

- Uncertainty in current measurements

The error on the currents measured by the Keithley 2601 sourcemeter gives a negligible error, i.e. 10^{-7}A for the 10 mA range. The error comes from the repeatability of the measurements. It is estimated by measuring multiple scans on a sample in the same conditions and comparing them together. Typically, for the 10 mA range the averaged difference is 1×10^{-4} A. Therefore the error on the current is taken to be $\pm1\times10^{-4}$ A.

2- Uncertainty on the mesa structure resistance calculations

In this section, the uncertainty on the resistance of the mesa structure of a TJ calculated using the Corbino method is determined. The uncertainty on the current evaluated previously is used and the uncertainty on the dimensions of the devices is estimated. Once these values are determined, they are used to calculate the error on the total mesa structure resistance.

- Uncertainty on the dimensions:

The dimensions are measured using the microscope and the associated error is

$$\Delta M = 0.004\ \mu\text{m/pixel}. \tag{B.1}$$

Converting into pixel/cm gives

$$\frac{1}{\Delta M}\times 10^4 = \frac{1}{0.0040}\times 10^4 = 2.5\times 10^6\ \text{pixel/cm}. \tag{B.2}$$

The 4.50 times magnification is used to take the pictures, corresponding to a resolution of 1019.1 pixel/cm. Therefore, for a spacing of 70 μm, the error is

$$\frac{(0.007\ \text{cm})(1019.139487\ \text{pixel/cm})}{(2.5\times 10^6\ \text{pixel/cm})} = 3\times 10^{-2}\ \mu\text{m} \tag{B.3}$$

This value is negligible compared to the error due to the fabrication. For a spacing labelled 70 μm, the actual measured dimension can vary between 69 μm and 71 μm. Therefore, the error on the dimensions is estimated to 1 μm. This error can now be carried on for all the calculations.

- Uncertainty on the correction factor:

$$c = \frac{r_1}{s}\ln\left(\frac{r_1+s}{r_1}\right) \tag{B.4}$$

$$\Delta c = \frac{r_1}{s}\ln\left(\frac{r_1+s}{r_1}\right)\left(\sqrt{\left(\frac{\Delta\left(\frac{r_1}{s}\right)}{\frac{r_1}{s}}\right)^2+\left(\frac{\Delta\left(\ln\left(\frac{r_1+s}{r_1}\right)\right)}{\ln\left(\frac{r_1+s}{r_1}\right)}\right)^2}\right) \tag{B.5}$$

$$\Delta\left(\frac{r_1}{s}\right)=\left(\frac{r_1}{s}\right)\sqrt{\left(\frac{\Delta r_1}{r_1}\right)^2+\left(\frac{\Delta s}{s}\right)^2} \tag{B.6}$$

$$\Delta\ln\left(\left(\frac{r_1+s}{r_1}\right)\right)=\frac{r_1+s}{r_1}\Delta\left(\frac{r_1+s}{r_1}\right) \tag{B.7}$$

$$\Delta\left(\frac{r_1+s}{r_1}\right)=\frac{r_1+s}{r_1}\sqrt{\left(\frac{\sqrt{(\Delta r_1)^2+(\Delta s)^2}}{r_1+s}\right)^2+\left(\frac{\Delta r_1}{r_1}\right)^2} \tag{B.8}$$

$$\Delta\ln\left(\left(\frac{r_1+s}{r_1}\right)\right)=\left(\frac{r_1+s}{r_1}\right)^2\sqrt{\left(\frac{\sqrt{(\Delta r_1)^2+(\Delta s)^2}}{r_1+s}\right)^2+\left(\frac{\Delta r_1}{r_1}\right)^2} \tag{B.9}$$

$$\Delta c = \frac{r_1}{s}\ln\left(\frac{r_1+s}{r_1}\right)\sqrt{\left(\frac{\left(\left(\frac{r_1}{s}\right)\sqrt{\left(\frac{\Delta r_1}{r_1}\right)^2+\left(\frac{\Delta s}{s}\right)^2}\right)}{\left(\frac{r_1}{s}\right)}\right)^2+\left(\frac{\left(\left(\frac{r_1+s}{r_1}\right)^2\sqrt{\left(\frac{\sqrt{(\Delta r_1)^2+(\Delta s)^2}}{r_1+s}\right)^2+\left(\frac{\Delta r_1}{r_1}\right)^2}\right)}{\ln\left(\frac{r_1+s}{r_1}\right)}\right)^2} \tag{B.10}$$

Therefore the error on the corrected values of the resistance is:

$$\Delta\left(\frac{R_T}{c}\right)=\frac{R_T}{c}\sqrt{\left(\frac{\Delta R_T}{R_T}\right)^2+\left(\frac{\Delta c}{c}\right)^2} \tag{B.11}$$

This error is calculated for the *n*-type Corbinos and the *p*-type Corbinos. The corrected values of the resistance are plotted as a function of the spacing and the errors on the graphs can be approximated giving, for the *n*-Corbinos

$$slope=(2.9\pm0.3)\Omega \text{ and } y-\text{intercept}=(1800\pm60)\ \Omega/\text{cm} \tag{B.12}$$

and for the *p*-Corbinos

$$slope=(1.8\pm0.3)\ \Omega \text{ and } y-\text{intercept}=(560\pm70)\ \Omega/\text{cm}. \tag{B.13}$$

These errors can now be applied to the resistance calculations.

- Uncertainty on the sheet resistances and the contact resistances

The equation of the graph of the total resistance as a function of the spacing is given by Eq. (2.3.21). Thus, the error on the sheet resistance is

$$\Delta R_S=R_S\sqrt{\left(\frac{\Delta slope}{slope}\right)^2+\left(\frac{\Delta W_C}{W_C}\right)^2} \tag{B.14}$$

where

$$\Delta W_C=2\pi r_1\sqrt{\left(\frac{\Delta 2\pi}{2\pi}\right)^2+\left(\frac{\Delta r_1}{r_1}\right)^2} \tag{B.15}$$

Simplifying Eq. (B.15) gives

$$\Delta W_C = 2\pi r_1 \sqrt{\left(\frac{0}{2\pi}\right)^2 + \left(\frac{\Delta r_1}{r_1}\right)^2} \quad \text{and} \quad \Delta W_C = 2\pi \Delta r_1. \tag{B.16}$$

Hence,

$$\Delta W_C = 2\pi(0.0001) = 6\times10^{-4}\ \text{cm} \tag{B.17}$$

The error on the resistivity can be calculated using

$$\Delta\rho = \rho\sqrt{\left(\frac{\Delta R_S}{R_S}\right)^2 + \left(\frac{\Delta thickness}{thickness}\right)^2}\,. \tag{B.18}$$

The error on the contact resistance is

$$\Delta R_C = R_C \sqrt{\left(\frac{\Delta(y(0))}{y(0)}\right)^2} \tag{B.19}$$

The calculations are done for the *p*-type Corbino and the *n*-type Corbino, giving

$$\Delta R_{PS} = R_{PS}\sqrt{\left(\frac{70}{560}\right)^2 + \left(\frac{6\times10^{-4}}{0.0220}\right)^2} = 1\,\Omega/\square \tag{B.20}$$

$$\Delta R_{NS} = R_{NS}\sqrt{\left(\frac{60}{1800}\right)^2 + \left(\frac{6\times10^{-4}}{0.0220}\right)^2} = 2\,\Omega/\square \tag{B.21}$$

$$\Delta\rho_P = \rho_P\sqrt{\left(\frac{1}{11}\right)^2} = 5\times10^{-5}\,\Omega\cdot\text{cm} \tag{B.22}$$

$$\Delta\rho_N = \rho_N\sqrt{\left(\frac{2}{40}\right)^2} = 1\times10^{-4}\,\Omega\cdot\text{cm} \tag{B.23}$$

$$\Delta R_{PC} = R_{PC}\sqrt{\left(\frac{0.3}{1.8}\right)^2} = 0.2\,\Omega \tag{B.24}$$

$$\Delta R_{NC} = R_{NC}\sqrt{\left(\frac{0.3}{2.9}\right)^2} = 0.1\,\Omega \tag{B.25}$$

The contact resistances in $\Omega\cdot cm^2$ can be calculated, giving

$$\Delta R'_{PC} = 5\times10^{-6}\ \Omega\cdot cm^2 \tag{B.26}$$

and

$$\Delta R'_{NC} = 5\times10^{-6}\ \Omega\cdot cm^2 . \tag{B.27}$$

- Calculations for a TJ of dimension 70 × 70 μm

Calculating for a TJ of dimension 70 × 70 μm, gives

$$\Delta R_P = R_P\sqrt{\left(\frac{\Delta\rho_p}{\rho_p}\right)^2 + \left(\frac{\Delta thickness}{thickness}\right)^2 + \left(\frac{\Delta MesaArea}{MesaArea}\right)^2}, \tag{B.28}$$

where

$$\Delta MesaArea = MesaArea\sqrt{\left(\frac{\Delta MesaWidth}{MesaWidth}\right)^2 + \left(\frac{\Delta MesaLength}{MesaLength}\right)^2} \tag{B.29}$$

$$\Delta MesaArea = (0.007\times0.007)\sqrt{\left(\frac{0.0001}{0.007}\right)^2 + \left(\frac{0.0001}{0.007}\right)^2} \tag{B.30}$$

$$\Delta MesaArea = 1\times10^{-6}\ cm^2$$

Thus the error on the resistance of the *p*-layer is

$$\Delta R_P = R_P\sqrt{\left(\frac{5\times10^{-5}}{40\times10^{-4}}\right)^2 + \left(\frac{1\times10^{-6}}{4.9\times10^{-5}}\right)^2} = 4\times10^{-5}\ \Omega \tag{B.31}$$

and the error on the resistance of the *n*-layer is

$$\Delta R_N = R_N \sqrt{\left(\frac{\Delta R_{NS}}{R_{NS}}\right)^2 + \left(\frac{\Delta gap}{gap}\right)^2 + \left(\frac{\sqrt{(2\Delta MesaLength)^2 + (2\Delta MesaWidth)^2}}{2MesaLength + 2MesaWidth}\right)^2} \quad \text{(B.32)}$$

$$\Delta R_N = R_N \sqrt{\left(\frac{2}{40}\right)^2 + \left(\frac{0.0001}{1\times10^{-3}}\right)^2 + \left(\frac{\sqrt{(2\times0.0001)^2 + (2\times0.0001)^2}}{2\times0.007 + 2\times0.007}\right)^2} = 0.2\,\Omega \quad \text{(B.33)}$$

The error on the contact resistance becomes

$$\Delta R_{PC} = R_{PC} \sqrt{\left(\frac{\Delta R'_{PC}}{R'_{PC}}\right)^2 + \left(\frac{\Delta MesaArea}{MesaArea}\right)^2} = 0.1\,\Omega \quad \text{(B.34)}$$

$$\Delta R_{NC} = R_{NC} \sqrt{\left(\frac{\Delta R'_{NC}}{R'_{NC}}\right)^2 + \left(\frac{\Delta BottomContactArea}{BottomContact}\right)^2} = 0.05\,\Omega \quad \text{(B.35)}$$

where

$$\Delta BottomContactArea = \sqrt{(\Delta TotalArea)^2 - (\Delta E)^2}$$

$$\text{where } \Delta E = (MesaLength + 2MesaGap)(MesaWidth + 2MesaGap) \quad \text{(B.36)}$$

$$\sqrt{\left(\frac{\sqrt{(\Delta MesaLength)^2 + (2\Delta MesaGap)^2}}{MesaLength + 2MesaGap}\right)^2 + \left(\frac{\sqrt{(\Delta MesaWidth)^2 + (2\Delta MesaGap)^2}}{(MesaWidth + 2MesaGap)}\right)^2}$$

$$\Delta BottomContactArea = 7\times10^{-5}\ \text{cm}^2. \quad \text{(B.37)}$$

Thus the error on the total mesa resistance of a TJ of dimension 70 × 70 μm is

$$\Delta R_T = \Delta R_P + \Delta R_N + \Delta R_{NC} + \Delta R_{PC} \tag{B.38}$$

$$\Delta R_T = 4\times10^{-5} + 0.2 + 0.04 + 0.1 = 0.3\,\Omega. \tag{B.39}$$

Multiplying by the area gives

$$\Delta R'_T = (0.3)(4.9\times10^{-5}) = 0.2\times10^{-4}\ \Omega\cdot\mathrm{cm}^2. \tag{B.40}$$

References

[1] A. E. Becquerel, "Mémoire sur les effets électriques produits sous l'influence des rayons solaires," *Comptes Rendus,* vol. 9, pp. 561-567, 1839.

[2] J. Nelson, *The Physics of Solar Cells,* World Scientific Pub Co Inc, 2003.

[3] S. Sun, Z. Fan, Y. Wang and J. Haliburton, "Organic solar cell optimizations," *J. Mater. Sci.,* vol. 40, pp. 1429-1443, 2005.

[4] J. Perlin, *From Space to Earth: The Story of Solar Electricity,* aatec Publications, 1999.

[5] D. M. Chapin, C. S. Fuller and G. L. Pearson, "A New silicon p-n junction photocell for converting solar radiation into electrical power," *J. Appl. Phys.,* vol. 25, pp. 676, 1954.

[6] C. W. Tang and S. A. VanSlyke, "Organic electroluminescent diodes," *Appl. Phys. Lett.,* vol. 51, pp. 913, 1987.

[7] G. A. Chamberlain, "Organic solar cells: a review," *Solar Cells,* vol. 8, pp. 47-83, 1983.

[8] H. Hoppea and N. S. Sariciftci, "Organic solar cells: An overview," *J. Mater. Res.,* vol. 19, pp. 1925, 2004.

[9] S. S. Sun and N. S. Sariciftci, *Organic Photovoltaics: Mechanism, Materials, and Devices.* CRC, 2005.

[10] K. L. Chopra, P. D. Paulson and V. Dutta, "Thin-film solar cells: an overview," *Prog. Photovoltaics Res. Appl.,* vol. 12, pp. 69-92, 2004.

[11] S. Kurtz, "Opportunities and challenges for development of a mature concentrating photovoltaic power industry," NREL 2009.

[12] L. Esaki, "New Phenomenon in Narrow Germanium p-n Junctions," *Phys. Rev.,* vol. 109, pp. 603-604, 1958.

[13] A. K. Jonscher, "The physics of the tunnel diode," *Br. J. Appl. Phys.,* vol. 12, pp. 654-659, 1961.

[14] R. L. Anderson, "Experiments on Ge-GaAs heterojunctions," *Solid-State Electron.,* vol. 5, pp. 341-344, 1962.

[15] T. W. Hickmott, P. M. Solomon, F. F. Fang, F. Stern, R. Fischer and H. Morkoc, "Sequential Single-Phonon Emission in GaAs-Al_ {x} Ga_ {1-x} As Tunnel Junctions," *Phys. Rev. Lett.,* vol. 52, pp. 2053-2056, 1984.

[16] W. Guter and A. W. Bett, "I-V characterization of tunnel diodes and multijunction solar cells," *IEEE Trans. Electron. Dev.*, vol. 53, pp. 2216-2222, 2006.

[17] M. Hermle, S. P. Philipps, G. Letay and A. W. Bett, "Numerical simulation of tunnel diodes and multi-junction solar cells," *Prog. Photovolt: Res. Appl.*, vol. 16, pp. 409–418, 2008.

[18] K. Jandieri, S. D. Baranovskii, W. Stolz, F. Gebhard, W. Guter, M. Hermle and A. W. Bett, "Fluctuations of the peak current in tunnel diodes," *J. Phys. D*, vol. 42, pp. 155101, 2009.

[19] J. F. Wheeldon, C. E. Valdivia, A. Walker, G. Kolhatkar, T. J. Hall, K. Hinzer, D. Masson, B. Riel, S. Fafard, A. Jaouad, A. Turala, R. Ares and V. Aimez, "GaAs, AlGaAs and InGaP tunnel junctions for multi-junction solar cells under concentration: Resistance study," *International Conference on Concentrating Photovoltaic Systems (CPV-6)*, Freiburg, Germany, 2010.

[20] W. Guter, J. Schöne, S. P. Philipps, M. Steiner, G. Siefer, A. Wekkeli, E. Welser, E. Oliva, A. W. Bett and F. Dimroth, "Current-matched triple-junction solar cell reaching 41.1% conversion efficiency under concentrated sunlight," *Appl. Phys. Lett.*, vol. 94, pp. 223504-223507, 2009.

[21] E. Kapon and A. Sirbu, "Long-wavelength VCSELs: Power-efficient answer," *Nat. Photonics*, vol. 3, pp. 27-29, 2009.

[22] S. Adachi, *Physical Properties of III-V Semiconductor Compounds: InP, InAs, GaAs, GaP, InGaAs, and InGaAsP*, Wiley-Interscience, 1992.

[23] J. G. Korvink and A. Greiner, *Semiconductors for Micro-and Nanotechnology: An Introduction for Engineers*, Wiley-VCH, 2002.

[24] S. R. Wenham, M. Green, M. Watt and R. Corkish, *Applied Photovoltaics*, Earthscan/James & James, 2007.

[25] C. Kittel, *Introduction to Solid State Physics*, Wiley, 2005.

[26] S. M. Sze, *Physics of Semiconductor Devices*, 3rd edition, Wiley-Interscience, 1981.

[27] W. A. Harrison, *Solid State Theory*, Dover Publications, 1980.

[28] Y. Varshni, "Temperature dependence of the energy gap in semiconductors," *Physica*, vol. 34, pp. 149-154, 1967.

[29] Y. Suematsu, A. R. Adams, D. F. Rogers, J. A. Adams, J. A. S. Adams, J. A. S. Adams, W. M. Lowder, A. Adams and A. Adams, *Handbook of Semiconductor Lasers and Photonic Integrated Circuits*, Chapman and Hall, London, 1952.

[30] A. Luque and S. Hegedus, *Handbook of photovoltaic science and engineering*, John Wiley & Sons Inc, pp. 396-397, 2003.

[31] R. A. Smith, Ed., *Semiconductors*, Cambridge University Press, 1978.

[32] N. W. Ashcroft and N. D. Mermin, *Solid State Physics,* Saunders College, Philadelphia, 1976.

[33] S. Banerjee and B. G. Streetman, *Solid State Electronic Devices,* Prentice Hall, 2000.

[34] ASTM Standard E490-00a, "Standard solar constant and zero air mass solar spectral irradiance tables," 2006.

[35] M. J. Chuang, H. F. Huang, C. H. Wen and A. K. Chu, "On the structure and surface chemical composition of indium–tin oxide films prepared by long-throw magnetron sputtering," *Thin Solid Films,* vol. 518, pp. 2290, 2008.

[36] R. R. King, J. H. Ermer, D. D. Krut, J. E. Granata, M. S. Gillanders, B. T. Cavicchi and N. H. Karam, "Advances in high-efficiency III-V multijunction solar cells," *Space Power Workshop*, pp. 2-5, 2001.

[37] R. R. King, D. C. Law, K. M. Edmondson, C. M. Fetzer, G. S. Kinsey, H. Yoon, R. A. Sherif and N. H. Karam, "40% efficient metamorphic GaInP/ GaInAs/ Ge multijunction solar cells," *Appl. Phys. Lett.,* vol. 90, pp. 183516, 2007.

[38] ASTM Standard G173-03, "Standard tables for reference solar spectral irradiances: Direct normal and hemispherical on 37° tilted surface," 2003.

[39] V. K. Narasimhan, C. E. Valdivia, N. Yastrebova, J. Fafard, V. Tatsiankou, F. Lejean, T. J. Hall and K. Hinzer, "Performance analysis of III–V triple-junction concentrator solar cells under varying temperature and intensity," *IEEE Lasers and Electro-Optics Society (LEOS) 21st Annual Meeting*, pp. 91-92, 2008.

[40] G. Kolhatkar, J. F. Wheeldon, C. E. Valdivia, A. Walker, S. Fafard, A. Turala, A. Jaouad, R. Ares, V. Aimez and K. Hinzer, "Time-dependent analysis of AlGaAs/AlGaAs tunnel junctions for high efficiency multi-junction solar cells," *Photonics North 2010, Proc. SPIE*, Niagara Falls, Canada, 2010.

[41] J. F. Wheeldon, C. E. Valdivia, A. Walker, G. Kolhatkar, D. Masson, B. Riel, S. Fafard, A. Jaouad, A. Turala, R. Ares, V. Aimez, T. J. Hall and K. Hinzer, "Performance comparison of AlGaAs, GaAs and InGaP tunnel junctions for concentrated multi-junction solar cells," *Prog. Photovoltaics Res. Appl.,* March 2010.

[42] D. J. Griffiths and E. G. Harris, *Introduction to quantum mechanics*, 2nd edition, Pearson Prentice Hall, pp. 315-339, 1995.

[43] A. Förster, "Resonant tunneling diodes: the effect of structural properties on their performance," *Adv. in Solid State Phys.,* vol. 33, pp. 37-62, 1993.

[44] Synopsys Inc., "Sentaurus device guide," Tech. Rep. Release A-2008.09, Switzerland 2009.

[45] J. F. Wheeldon, C. E. Valdivia, A. Walker, G. Kolhatkar, T. J. Hall, K. Hinzer, D. Masson, B. Riel, S. Fafard, A. Jaouad, A. Turala, R. Ares and V. Aimez, "AlGaAs tunnel junction for high efficiency multi-junction solar cells: Simulation and measurements of temperature-

dependent operation," *34th IEEE Photovoltaic Specialist Conference 2009,* Philadelphia, PA, USA, pp. 135, 2009.

[46] P. Van Zant, *Microchip Fabrication: A Practical Guide to Semiconductor Processing*, McGraw-Hill New York, 2000.

[47] S. M. Sze, *Physics of Semiconductor Devices*, 1st edition, Wiley-Interscience, 1969.

[48] L. Esaki and Y. Miyahara, "A new device using the tunneling process in narrow pn junctions," *Solid-State Electron.,* vol. 1, pp. 13-14, 1960.

[49] W. Shockley, "Research and investigation of inverse epitaxial UHF power transistors," *Air Force Avionics Lab,* 1964.

[50] G. K. Reeves and H. B. Harrison, "Obtaining the specific contact resistance from transmission line model measurements," *IEEE Electron Device Lett.,* vol. 3, pp. 111-113, 1982.

[51] J. F. Bresse and S. Blayac, "Epitaxial layer sheet resistance outside and under ohmic contacts measurements using electrostatic force microscopy," *Solid-State Electron.,* vol. 45, pp. 1071-1076, 2001.

[52] Y. G. Chen, M. Ogura, S. Yamasaki and H. Okushi, "Investigation of specific contact resistance of ohmic contacts to B-doped homoepitaxial diamond using transmission line model," *Diamond Relat. Mater.,* vol. 13, pp. 2121-2124, 2004.

[53] G. S. Marlow and M. B. Das, "The effects of contact size and non-zero metal resistance on the determination of specific contact resistance," *Solid-State Electron.,* vol. 25, pp. 91-94, 1982.

[54] M. Ahmad and B. M. Arora, "Investigation of AuGeNi contacts using rectangular and circular transmission line model," *Solid-State Electron.,* vol. 35, pp. 1441-1445, 1992.

[55] J. H. Klootwijk and C. E. Timmering, "Merits and limitations of circular TLM structures for contact resistance determination for novel III-V HBTs," *Proc. IEEE 2004 Int. Conference on Microlelectronic Test Structures*, pp. 247-252, 2004.

[56] L. F. Lester, J. M. Brown, J. C. Ramer, L. Zhang, S. D. Hersee and J. C. Zolper, "Nonalloyed Ti/Al Ohmic contacts to n-type GaN using high-temperature premetallization anneal," *Appl. Phys. Lett.,* vol. 69, pp. 2737, 1996.

[57] D. K. Schroder and D. L. Meier, "Solar cell contact resistance—a review," *IEEE Trans. Electron Dev.,* vol. 31, pp. 637-647, 1984.

[58] A. Walker, J. F. Wheeldon, C. E. Valdivia, G. Kolhatkar and K. Hinzer, "Simulation, modeling and comparison of III-V tunnel junction designs for high efficiency metamorphic multi-junction solar cells," *Photonics North 2010, Proc. SPIE*, Niagara Falls, Canada, 2010.

[59] Keithley Instruments Inc. "Keithley Series 2600A System SourceMeter Instruments Reference Manual," section 2, 2010.

[60] P. Wurfel and U. Wurfel, *Physics of Solar Cells,* Wiley-VCH, 2005.

[61] J. F. Young, B. M. Wood, H. C. Liu, M. Buchanan, D. Landheer, A. J. SpringThorpe and P. Mandeville, "Effect of circuit oscillations on the dc current-voltage characteristics of double barrier resonant tunneling structures," *Appl. Phys. Lett.,* vol. 52, pp. 1398-1400, 1988.

[62] K. Jensen and F. Buot, "Numerical simulation of intrinsic bistability and high-frequency current oscillations in resonant tunneling structures," *Phys. Rev. Lett.,* vol. 66, pp. 1078-1081, 1991.

[63] R. H. Enns and G. McGuire, *Nonlinear Physics with Maple for Scientists and Engineers,* Birkhauser, 2000.

[64] S. H. Strogatz, *Nonlinear Dynamics and Chaos: With Applications to Physics, Biology, Chemistry, and Engineering*, chap.7, Westview Press, 2000.

[65] F. A. Buot and K. L. Jensen, "Intrinsic high-frequency oscillations and equivalent circuit model in the negative differential resistance region of resonant tunneling devices," *COMPEL,* vol. 10, pp. 241-253, 1991.

[66] John C. Butcher, *Numerical methods for ordinary differential equations*, 2nd edition, John Wiley and Sons, 2003.

[67] D. Jung, C. A. Parker, J. Ramdani and S. M. Bedair, "AlGaAs/GaInP heterojunction tunnel diode for cascade solar cell application," *J. Appl. Phys.,* vol. 74, pp. 2090-2093, 1993.

[68] T. Margalith, O. Buchinsky, D. A. Cohen, A. C. Abare, M. Hansen, S. P. DenBaars and L. A. Coldren, "Indium tin oxide contacts to gallium nitride optoelectronic devices," *Appl. Phys. Lett.,* vol. 74, pp. 3930, 1999.

[69] T. Karasawa and Y. Miyata, "Electrical and optical properties of indium tin oxide thin films deposited on unheated substrates by dc reactive sputtering," *Thin Solid Films,* vol. 223, pp. 135-139, 1993.

[70] L. Meng, A. Macarico and R. Martins, "Study of annealed indium tin oxide films prepared by rf reactive magnetron sputtering," *Vacuum,* vol. 46, pp. 673-680, 1995.

[71] W. F. Wu, B. S. Chiou and S. T. Hsieh, "Effect of sputtering power on the structural and optical properties of RF magnetron sputtered ITO films," *Semicond. Sci. and Technol.,* vol. 9, pp. 1242, 1994.

[72] H. Kobayashi, T. Ishida, K. Nakamura, Y. Nakato and H. Tsubomura, "Properties of indium tin oxide films prepared by the electron beam evaporation method in relation to characteristics of indium tin oxide/silicon oxide/silicon junction solar cells," *J. Appl. Phys.,* vol. 72, pp. 5288, 1992.

[73] H. Kim, C. M. Gilmore, A. Pique, J. S. Horwitz, H. Mattoussi, H. Murata, Z. H. Kafafi and D. B. Chrisey, "Electrical, optical, and structural properties of indium–tin–oxide thin films for organic light-emitting devices," *J. Appl. Phys.,* vol. 86, pp. 6451, 1999.

[74] M. J. Alam and D. C. Cameron, "Characterization of transparent conductive ITO thin films deposited on titanium dioxide film by a sol-gel process," *Surf. and Coat. Technol.*, vol. 142, pp. 776-780, 2001.

[75] H. Kobayashi, T. Ishida, Y. Nakato and H. Tsubomura, "Mechanism of carrier transport in highly efficient solar cells having indium tin oxide/Si junctions," *J. Appl. Phys.*, vol. 69, pp. 1736, 1991.

[76] S. E. Shaheen, C. J. Brabec, N. S. Sariciftci, F. Padinger, T. Fromherz and J. C. Hummelen, "2.5% efficient organic plastic solar cells," *Appl. Phys. Lett.*, vol. 78, pp. 841, 2001.

[77] C. E. Valdivia, E. Desfonds, D. Masson, S. Fafard, A. Carlson, J. Cook, T. J. Hall and K. Hinzer, "Optimization of antireflection coating design for multi-junction solar cells and concentrator systems," *Proceedings of SPIE, the International Society for Optical Engineering*, pp. 709911-709915, 2008.

[78] Newport Resource, "1600W Oriel solar simulators," pp. 200, 2008/2009.

[79] D. K. Schroder, *Semiconductor Material and Device Characterization,* Wiley-Interscience, 2006.